

**THE DEVELOPMENT OF NOISE REDUCTION MODEL
FOR COMPUTED RADIOGRAPHY SYSTEM**

Boonserm Nerysungnoen



**A Thesis Submitted in Partial Fulfillment of the Requirements for the
Degree of Doctor of Information Science in Information Technology**

Suranaree University of Technology

Academic Year 2015

การพัฒนาแบบจำลองการลดสัญญาณรบกวนสำหรับ
ระบบการสร้างภาพรังสีด้วยคอมพิวเตอร์



นายบุญเสริม เนยสูงเนิน

วิทยานิพนธ์นี้เป็นส่วนหนึ่งของการศึกษาตามหลักสูตรปริญญาวิทยาศาสตรมหาบัณฑิต
สาขาวิชาเทคโนโลยีสารสนเทศ
มหาวิทยาลัยเทคโนโลยีสุรนารี
ปีการศึกษา 2558

THE DEVELOPMENT OF NOISE REDUCTION MODEL FOR COMPUTED RADIOGRAPHY SYSTEM

Suranaree University of Technology has approved this thesis submitted in partial fulfillment of the requirements for the Degree of Doctor of Information Science in Information Technology.

Thesis Examining Committee

Polnigong, T. W.
(Assoc. Prof. Dr. Weerapong Polnigongit)

Chairperson

J. Tanthanuch
(Asst. Prof. Dr. Jessada Tanthanuch)

Member (Thesis Advisor)

[Signature]
(Asst. Prof. Dr. Banjong Kheonkaew)

Member

S. Niwatt
(Asst. Prof. Dr. Suphakit Niwattanukul)

Member

[Signature]
(Asst. Prof. Dr. Thara Angskun)

Member

[Signature]
(Prof. Dr. Sukit Limpijumnong)

Vice Rector for Academic Affairs
and Innovation

[Signature]
(Dr. Peerasak Siriyothin)

Dean of Institute of Social Technology

บุญเสริม เนยสูงเนิน : การพัฒนาแบบจำลองการลดสัญญาณรบกวนสำหรับระบบการ
สร้างภาพรังสีด้วยคอมพิวเตอร์ (THE DEVELOPMENT OF NOISE REDUCTION
MODEL FOR COMPUTED RADIOGRAPHY SYSTEM) อ า จ า ร ย ์ ที่ ป ร ี ก ษ า :
ผู้ช่วยศาสตราจารย์ ดร. เจษฎา คันทนุช, 188 หน้า.

ภาพเอกซเรย์มีข้อดีในการช่วยวินิจฉัยหรือตรวจเช็คผู้ป่วย ภาพเอกซเรย์ใช้ฟิล์มแบบดั้งเดิม
ถูกแทนที่ด้วยภาพดิจิทัล เช่น ภาพเอกซเรย์ซีอาร์ ซึ่งมีข้อดีหลายอย่าง ยกตัวอย่าง เช่น ภาพที่
สามารถดูได้ ขยาย วัด และเปรียบเทียบบนจอภาพโดยรังสีแพทย์ ภาพเอกซเรย์ที่เป็นภาพดิจิทัล
สามารถเก็บได้ในระยะยาว และมีความเสี่ยงของการสูญหายน้อยกว่าภาพในระบบฟิล์ม การสร้าง
ภาพรังสีแบบดิจิทัลมีช่วงพลวัตที่กว้าง และสามารถดำเนินการกับภาพซ้ำแล้วซ้ำอีก โดยไม่กระทบ
กับคุณภาพ อย่างไรก็ตาม สัญญาณรบกวนเป็นปัจจัยสำคัญที่ลดคุณภาพของภาพเอกซเรย์ บางครั้ง
อาจจะทำให้เกิดการวินิจฉัยผิดพลาดได้ ดังนั้นงานวิจัยนี้มีวัตถุประสงค์ เพื่อพัฒนาขั้นตอนวิธี
สำหรับระบุนิคมสัญญาณรบกวนในระบบเอกซเรย์ซีอาร์ ประยุกต์ขั้นตอนวิธีสำหรับลดสัญญาณ
รบกวนในภาพเอกซเรย์ซีอาร์ และสร้างโปรแกรมต้นแบบเพื่อลดสัญญาณรบกวน

การวิจัยนี้ดำเนินการควบคุมคุณภาพระบบซีอาร์ พัฒนาขั้นตอนวิธีสำหรับจำแนกสัญญาณ
รบกวน และประยุกต์ขั้นตอนวิธีสำหรับลดสัญญาณรบกวน การตรวจคุณภาพของระบบซีอาร์
ปฏิบัติตามแนวทางมาตรฐานของ ไอ พี อี เอ็ม การจำแนกสัญญาณรบกวนในภาพเอกซเรย์ซีอาร์ ทำ
การสร้างโมเดลโดยใช้ขั้นตอนวิธีเพอร์เซ็ปตรอนหลายชั้น สำหรับการระบุนิคมสัญญาณรบกวน
และขั้นตอนวิธีสำหรับลดสัญญาณรบกวนใช้ตัวกรองแบบคลุมเครือสำหรับลดสัญญาณรบกวน

การควบคุมคุณภาพของระบบซีอาร์เป็นที่ยอมรับได้ตามมาตรฐาน ไอ พี อี เอ็ม การจำแนก
สัญญาณรบกวนในระบบซีอาร์สามารถจำแนกได้ว่า คือ สัญญาณรบกวนแบบปัวซอง และเกาส์เซียน
ซึ่งมีค่าเฉลี่ยของค่าคั่นคั่น เท่ากับ 93.31% ค่าเฉลี่ยของค่าความเที่ยง เท่ากับ 93.79% และค่าเฉลี่ย
ของค่าเอฟเมเชอร์ เท่ากับ 93.34% สำหรับการจำแนก ซอฟต์แวร์ต้นแบบสามารถลดสัญญาณ
รบกวนได้มากกว่าซอฟต์แวร์ของบริษัท ผลการประเมินภาพที่ถูกลดสัญญาณรบกวน ค่าความคลาด
เคลื่อนกำลังสองเฉลี่ย เท่ากับ 0.2822 ค่าพิคซิกแนลทูนอยส์เรโซ เท่ากับ 53.6247 และค่า
สหสัมพันธ์ เท่ากับ 0.9972

BOONSERM NERYSUNGNOEN : THE DEVELOPMENT OF NOISE
REDUCTION MODEL FOR COMPUTED RADIOGRAPHY SYSTEM.
THESIS ADVISOR : ASST. PROF. JESSADA TANTHANUCH, Ph.D.,
188 PP.

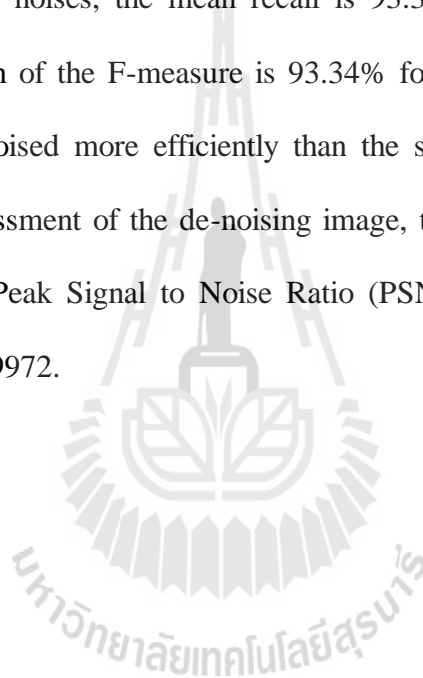
COMPUTED RADIOGRAPHY/CLASSIFICATION/NOISE REDUCTION

There are many advantages to having X-ray images, diagnoses or check-ups for patients. Conventional X-ray images are replaced by digital X-rays, such as computed radiography (CR) images. The advantages of having digital X-rays are, for example, that the images can be viewed, extended, measured and compared on a monitor by the radiologist. Since the images are produced digitally, they can be stored long term and there is less risk of their being lost and they require less storage space than conventional X-ray films. Digital radiography has a wide dynamic range and can be processed repeatedly without compromising on quality. However, image noise is a key factor that reduces the quality of X-ray images. It sometimes causes a deficiency in images which can lead to misdiagnoses. Hence, this research aims to develop an algorithm for the specification of the type of noise in the CR system, and to apply the appropriate algorithm for reducing noise in CR images and to create a prototype software for de-noising.

This research includes commissioning and routine quality control of CR systems, develops algorithms for the classification of the noise in the CR system, and applies an algorithm for de-noising. The commissioning and routine quality control of the CR system is performed following the guidelines of the Institute of Physics and

Engineering in Medicine (IPEM). The classification of the noise in the CR the system is conducted by creating a model using multilayer perceptron (MLP) algorithms for specifying noise types. The algorithm for de-noising applies fuzzy filters for de-noising.

The quality control of the CR system is acceptable according to the guidelines of the IPEM. The classification of the noise in the CR image can be specified as Poisson and Gaussian noises, the mean recall is 93.31%, the mean of precision is 93.79%, and the mean of the F-measure is 93.34% for classification. This prototype software can be de-noised more efficiently than the software found on the market. According to the assessment of the de-noising image, the Mean Square Error (MSE) value is 0.2822, the Peak Signal to Noise Ratio (PSNR) value is 53.6247 and the correlation value is 0.9972.



School of Information Technology

Academic Year 2015

Student's Signature Boonserm N.

Advisor's Signature S.Tanthanuch

ACKNOWLEDGEMENTS

There are many people to whom I would like to express my sincere gratitude for their assistance, advice and encouragement which I have received in completing this dissertation.

First, my deepest respect and sincere gratitude belong to my research advisor, Asst. Prof. Dr. Jessada Tanthanuch. I am very grateful for his supervision, useful comments, kind assistance, continuous encouragement, and understanding given to me. Without him, I would not have been able to complete my dissertation.

I would like to express my very great appreciation to Assoc. Prof. Dr. Weerapong Polnigongit, the chairman of my dissertation committee, for his suggestion and assistance. My grateful thanks are also extended to the committees for my dissertation, who are Asst. Prof. Dr. Banjong Kheonkaew for his insightful comments, Asst. Prof. Dr. Suphakit Niwattanakul for his intelligent comments, Asst. Prof. Dr. Thara Angskun and Asst. Prof. Dr. Jitimon Angskun for giving me opportunity and inspiration in all aspects of this endeavor.

My grateful thanks go to Institute of Social Technology, School of Information Technology, Suranaree University of Technology for offering me a scholarship in order to study a doctor degree and to all of my lecturers at the School of Information Technology for their kindness in teaching me throughout my study.

I would like to extend my gratitude to Institute of Science, School of Mathematics, Suranaree University of Technology for studying and researching.

I would like to express my thanks to all of my research at Maharat Nakhon Ratchasima Hospital. I would also like to express my gratitude to the Department of Radiology, Faculty of Medicine, Khon Kaen University for facilitating to experimental devices.

Finally, I wish to convey thanks to my beloved parents, my family, sister and brother for their endless love and care, encouragement and moral support.

Boonserm Nerysungnoen

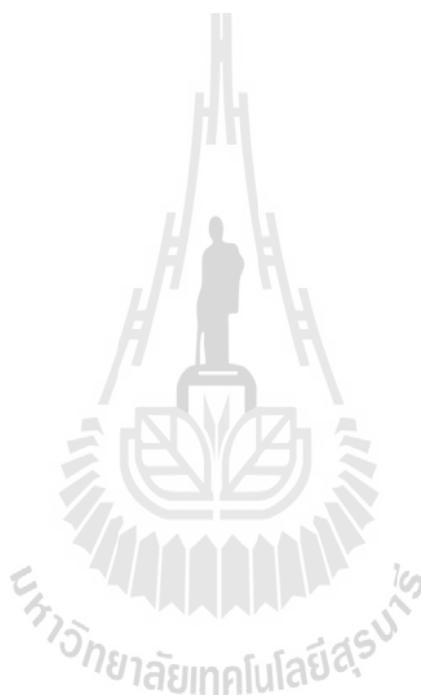


TABLE OF CONTENTS

	Page
ABSTRACT (THAI)	I
ABSTRACT (ENGLISH)	II
ACKNOWLEDGEMENTS	IV
TABLE OF CONTENTS	VI
LIST OF TABLES	XI
LIST OF FIGURES	XIII
CHAPTER	
1 INTRODUCTION	1
1.1 Introduction.....	1
1.2 Research Objectives.....	3
1.3 Research Hypothesis.....	3
1.4 Scope of the Study.....	4
1.5 Expected Results.....	4
1.6 Definitions of Terms.....	4
2 REVIEW OF THE LITERATURE	6
2.1 X-ray Production	7
2.1.1 The X-ray Tube.....	7
2.1.2 Bremsstrahlung X-ray Generation.....	9

TABLE OF CONTENTS (Continued)

	Page
2.1.3 Characteristic X-ray Generation	12
2.1.4 Interaction of X-ray with Matter.....	14
2.1.5 Attenuation and Subject Contrast.....	18
2.2 Mechanism of Processing in CR.....	21
2.3 Commissioning and Routine Quality Control of CR.....	32
2.3.1 Image Processing.....	33
2.3.2 Signal Transfer Property.....	34
2.3.3 Detector Dose Indicator.....	36
2.3.4 Beam Quality.....	39
2.3.5 Commissioning and Quality Control.....	40
2.4 Mathematical Model of Noise.....	42
2.5 Machine Learning for Classification.....	52
2.6 Artificial Neural Network.....	54
2.7 Fuzzy Logic.....	61
2.8 Algorithm of Noise Reduction.....	67
2.8.1 Linear Filters.....	67
2.8.2 Non-linear Filter	68
2.9 Computer Programming.....	68
2.9.1 ImageJ.....	68
2.9.2 MATLAB.....	70

TABLE OF CONTENTS (Continued)

	Page
2.9.3 Weka.....	71
2.10 Related Work.....	73
3 RESEARCH PROCEDURE.....	84
3.1 Research Methodology.....	84
3.1.1 Commissioning and Routine Quality Control of CR.....	84
3.1.2 Classification the Noise in the Computed Radiography System.....	97
3.1.3 The Algorithm for De-noising.....	105
3.1.4 Hypothesis Testing.....	117
3.2 Research Instruments.....	117
3.3 Data Collection.....	118
3.4 Data Analysis.....	118
3.4.1 Analyzing Evaluating the Performance of Classification.....	119
3.4.2 Analyzing Peak Signal to Noise Ratio and MSE.....	120
3.4.3 Analyzing Correlation.....	121
4 THE RESULTS OF THE STUDY AND DISCUSSIONS.....	122
4.1 Commissioning and Routine Quality Control of CR.....	122
4.1.1 Result of Dosimetry.....	122
4.1.2 Result of Calibration of CR Unit DDI.....	123
4.1.3 Result of STP and DDI with Standard Factors.....	125
4.1.4 Result of DDI Repeatability.....	129

TABLE OF CONTENTS (Continued)

	Page
4.1.5 Result of Matching of CR Imaging Plates.....	130
4.1.6 Result of Differences between CR readers.....	131
4.1.7 Result of Dark Noise.....	132
4.1.8 Result of Measured Uniformity.....	133
4.1.9 Result of Erasure Cycle Efficiency.....	134
4.1.10 Result of Variation of Noise with Detector Air Kerma.....	135
4.1.11 Result of Signal to Noise Ratio.....	137
4.1.12 Results of Limiting High Contrast Spatial Resolution.....	138
4.1.13 Result of Laser Beam Function.....	141
4.2 Classification the Noise in Computed Radiography System.....	142
4.2.1 Result of Formation the Original Image.....	143
4.2.2 Results of Production the Known-Noise.....	143
4.2.3 Results of Adding the Known-Noise in Original Image.....	147
4.2.4 Result of Feature Extraction.....	151
4.2.5 Result of Feature Selection.....	151
4.2.6 Result of Modeling.....	152
4.2.7 Results of Model Usage.....	160
4.3 The Algorithm for De-noising.....	166
4.3.1 Results of Reduced Poisson Noise.....	166
4.3.2 Results of Reduced Gaussian Noise.....	167

TABLE OF CONTENTS (Continued)

	Page
4.3.3 Results of the Prototype Program.....	167
4.4 Hypothesis Testing	170
4.4.1 Result of De-noised CR image Using Prototype Program.....	170
4.4.2 Result of De-noised CR image Using Vendor’s Software.....	172
5 CONCLUSIONS AND RESEARCH RECOMMENDATIONS.....	173
5.1 Summary of the Research Findings.....	173
5.1.1 Summary of Commissioning and Routine Quality Control of CR.....	174
5.1.2 Summary of Classification the Noise in CR System.....	176
5.1.3 Summary of Algorithm for De-noising.....	176
5.2 The Limitation of the Study.....	177
5.3 The Application of the Study.....	178
5.4 Recommendations for Further Study.....	179
REFERENCES.....	180
CURRICULUM VITAE.....	188

LIST OF TABLES

Table		Page
2.1	Manufacturers' conditions for checking DDI calibration.....	38
2.2	Comparison of standard beam spectra for testing.....	40
2.3	Commissioning tests for CR.....	41
2.4	Summary of related work comparison associated with the development of noise reduction model for computed radiography system.....	81
3.1	The confusion matrix for evaluating the categorical output.....	103
3.2	The details of instances used for modeling.....	109
3.3	Confusion matrix.....	119
4.1	The air kerma of standard beam.....	123
4.2	Calibration of CR unit DDI.....	124
4.3	STP and DDI with standard factors.....	125
4.4	DDI repeatability.....	129
4.5	Matching of CR Imaging Plates.....	130
4.6	Differences between CR readers.....	131
4.7	Dark noise.....	132
4.8	Measured uniformity.....	133
4.9	Variation of noise with detector air kerma.....	135

LIST OF TABLES (Continued)

Table	Page
4.10 Values of mean pixel value, SD and SNR for the evaluating signal to noise ratio.....	138
4.11 Limiting high contrast spatial resolution.....	139
4.12 The values of feature extraction.....	151
4.13 The values of assessment the subsets for feature selection.....	152
4.14 Classifier model.....	154
4.15 Cross-validated confusion matrix for classifier.....	159
4.16 Detailed accuracy by class.....	160
4.17 Specifying the noise in CR images.....	165
4.18 Comparison of MSE, PSNR and Correlation for Poisson noise de-noised by filters.....	166
4.19 Comparison of MSE, PSNR and Correlation for Gaussian noise de-noised by filters.....	166
4.20 Cross-validated confusion matrix for classifier.....	168

LIST OF FIGURES

Figure		Page
2.1	X-ray machine circuit.....	7
2.2	X-ray tubes.....	8
2.3	The bremsstrahlung interaction.....	10
2.4	The bremsstrahlung X-ray spectrum.....	11
2.5	The characteristic interaction in the x-ray tube.....	12
2.6	The characteristic X-ray spectrum.....	13
2.7	The coherent scattering.....	14
2.8	The photoelectric effect.....	15
2.9	The Compton effect.....	16
2.10	The pair production.....	17
2.11	The attenuation of an X-ray beam by a homogeneous object.....	18
2.12	The attenuation of an X-ray beam by a soft tissues.....	19
2.13	The relative predominance of photoelectric and Compton interactions in various tissues at increasing levels of kVp.....	21
2.14	Computed Radiography cycle.....	22
2.15	Substance element medium of three different type Imaging Plates.....	23
2.16	Imaging Plate and construction.....	24
2.17	CR reader.....	25

LIST OF FIGURES (Continued)

Figure	Page
2.18 Laser construction.....	26
2.19 CR reader laser optics.....	27
2.20 The laser scans Imaging Plate.....	28
2.21 Laser optics.....	29
2.22 Erasing the Imaging Plate.....	32
2.23 The PDF of Rayleigh noise.....	47
2.24 The PDF of gamma noise.....	48
2.25 The PDF of exponential noise.....	49
2.26 PDF of uniform noise.....	50
2.27 PDF of salt and pepper noise.....	51
2.28 Generic neural network architecture.....	55
2.29 Schematic representation of a biological (pyramidal cell) and artificial neuron.....	58
2.30 Activation functions, (a) linear, (b), threshold, and (c), sigmoid function....	59
2.31 Membership function.....	63
2.32 Input and output membership functions.....	65
3.1 The X-ray equipment.....	85
3.2 The dosimeter.....	85
3.3 The copper sheet.....	85

LIST OF FIGURES (Continued)

Figure		Page
3.4	The CR reader.....	86
3.5	The cassettes and Imaging Plates.....	87
3.6	The CR readers.....	91
3.7	The Hüttner test object.....	96
3.8	The steel ruler (a) and (b) ROI for plot profile	97
3.9	The TOR CDR phantom.....	98
3.10	The ImageJ software.....	98
3.11	The procedure for creating the original image.....	99
3.12	The procedure for retouching the image.....	99
3.13	The known-noise added.....	100
3.14	Diagram showing extraction of features	100
3.15	The algorithm for feature selection.....	101
3.16	Procedure for the selection of the best subset.....	102
3.17	Modeling of MLP.....	102
3.18	Model using for classification.....	104
3.19	Calculation of each node.....	104
3.20	Diagram of the prototype program.....	106
3.21	Fuzzy inference system used for creating the original image.....	106
3.22	Membership functions of input variable “SD”.....	108

LIST OF FIGURES (Continued)

Figure		Page
3.23	Membership functions of output variable “Matrix size”.....	108
3.24	Fuzzy inference system for creating fuzzy filter of Poisson noise.....	110
3.25	Membership functions of input variable “SD”.....	111
3.26	Membership functions of input variable “MSE”.....	112
3.27	Membership functions of output variable “Matrix size”.....	112
3.28	Fuzzy inference system for creating fuzzy filter of Gaussian noise.....	113
3.29	Membership functions of input variable “SD”.....	114
3.30	Membership functions of input variable “MSE”.....	115
3.31	Membership functions of output variable “Matrix size”.....	116
4.1	Graph of STP function of 14” x 17”.....	126
4.2	Graph of STP function of 10” x 12”.....	127
4.3	Graph of STP function of 8” x 10”.....	128
4.4	The first image, (a) and (b), the second image.....	134
4.5	Variation of noise with detector air kerma.....	135
4.6	Plot of laser beam function for test jitter.....	142
4.7	The CR image, (a) and (b), the original image.....	142
4.8	Image of added Gaussian noise to image, (a) and (b), its histogram.....	143
4.9	Image of added Rayleigh noise to image, (a) and (b), its histogram.....	144
4.10	Image of added gamma noise to image, (a) and (b), its histogram.....	144

LIST OF FIGURES (Continued)

Figure	Page
4.11	Image of added exponential noise to image, (a) and (b), its histogram... 145
4.12	Image of added uniform noise to image, (a) and (b), its histogram..... 145
4.13	Image of added impulse noise to image, (a) and (b), its histogram..... 146
4.14	Image of added Poisson noise to image, (a) and (b), its histogram..... 146
4.15	Images of added Gaussian noise to original image..... 147
4.16	Images of added Rayleigh noise to original image..... 147
4.17	Images of added gamma noise to original image..... 148
4.18	Images of added exponential noise to original image..... 148
4.19	Images of added uniform noise to original image..... 149
4.20	Images of added impulse noise to original image..... 149
4.21	Images of added Poisson noise to original image..... 150
4.22	Model for classified noise..... 153
4.23	Rule viewer of creating original image..... 167
4.24	Rule viewer for classification..... 168
4.25	Rule viewer of filtering Poisson noise..... 169
4.26	Rule viewer of filtering Gaussian noise..... 170
4.27	Rule viewer for calculating matrix size..... 171
4.28	Rule viewer for de-noising..... 172

CHAPTER 1

INTRODUCTION

1.1 Introduction

X-rays were used for detecting internal defects inside structures soon after being discovered by the German scientist Wilhelm Conrad Röntgen in 1895. In the form of very energetic radiation, it can penetrate opaque and even metallic objects. Radiography can detect variations in different types of materials or thickness via the variations in intensity of the transmitted radiation. Heavy or thick materials can greatly attenuate X-ray beams. The transmitted beam, which carries the object pattern, is received by a detector. At the beginning, in the early 1900s, glass radiography plates were used to detect X-ray images. Later, a flexible silver film was invented. Now, with the advent of the digital age, the film is being replaced more and more by digital detectors such as storage phosphor plates used in computed radiography (CR) and photoconductor plates used in digital radiography (DR).

When compared with traditional film radiography, digital technology, both CR and DR are much more dose efficient and have a larger dynamic range. A direct digital output allows image processing, long distance sharing, a lossless image copy, elimination of chemical development and physical storage. Though digital systems are more expensive than film systems, as films are not reusable, the long term costs become smaller. CR is based on the use of Photostimulated Phosphor (PSP) in the Imaging Plate (IP).

Digital radiography systems have replaced films over a broad range of investigations. The basic definition of digital imaging is any imaging acquisition process that produces an electronic image which can be viewed and manipulated on a computer. Most modern medical imaging modalities produce digital images that can be distributed through a computer network to a host of locations.

CR or cassette-based digital radiography is the digital acquisition modality that uses storage phosphor plates to produce projection images (Carter and Veale, 2010). There are many advantages of having digital X-rays, for example, the images can be viewed, extended, measured and compared on a monitor by the radiologist. Since the images are produced digitally, they can be stored long term and have less risk of being lost and they require less storage space than conventional X-ray films. Digital radiography has a wide dynamic range and can be processed repeatedly without compromising on quality (Bushberg, Seibert, Leidholdt, and Boone, 2002). However, image noise is a key factor that reduces the quality of X-ray images. It sometimes causes a deficiency in images which can lead to misdiagnoses.

This research focuses on noise arising in the image processing of CR systems. Analysis of the process provides a mathematical model of the CR image overlaid with noise which helps in the selection of a suitable method to de-noise and recover the anatomical details of the medical CR image.

The CR system is similar to the conventional X-ray system, which uses a film base for X-ray examinations. The receiver plate of a CR system uses an Imaging Plate that is like an X-ray film when the IP is exposed by X-ray beams, it is read by a CR reader. It is analogous to film processing in the conventional X-ray system. Finally, the digital X-ray image is processed and sent to a radiologist or physician. The

production process of the CR image requires several steps that are the cause of the noise, therefore this research will be of interest for research of the CR system.

The CR system is still being used in hospitals in Thailand which is expected to continue in the future, because this system is also important and cheaper than the DR system.

Hence, this research aims to apply the appropriate algorithm for reducing noise in the CR system. Prototype software will be designed to implement the algorithm. This study should help patients to obtain accurate diagnoses and treatment in the future.

1.2 Research Objectives

1.2.1 To develop an algorithm for the specification of the type of noise in the CR system.

1.2.2 To apply the appropriate algorithm for reducing noise in CR images.

1.2.3 To create a prototype software for de-noising in CR images.

1.3 Research Hypothesis

1.3.1 The recall for the classification of types of noise in the CR system is greater than or equal to 80%.

1.3.2 The prototype software can de-noise greater than the software currently available on the market.

1.4 Scope of the Study

1.4.1 The trial studies and research are located in the Department of Radiology, Maharat Nakhon Ratchasima Hospital, School of Information Technology, and the School of Mathematics, Suranaree University of Technology.

1.4.2 Duration of the study is from June 2015 to June 2016.

1.4.3 The contents of the study include quality evaluation of the CR system, specifications of the noise in the CR system, and the appropriate algorithm for noise reduction in CR images and prototype software for de-noising in CR images.

1.5 Expected Results

1.5.1 To produce the type of noise found in the CR system.

1.5.2 To produce the appropriate algorithm for noise reduction in CR images.

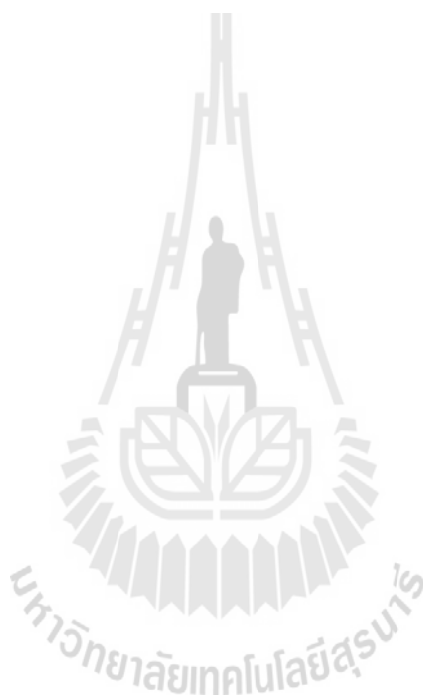
1.5.3 To produce prototype software which can enhance CR images.

1.6 Definitions of Terms

Computed Radiography (CR) is digital radiography that records radiographic images on photostimulable phosphor plates instead of film/ screen image receptors. The acquired image data are converted to electronic signals and digitized so they can be stored and manipulated by a computer and displayed on a high-resolution monitor or recorded on film by using a laser printer.

Noise is random variations of brightness or color information in images, and is usually an aspect of electronic noise, which produces random electronic variations in the signals of the electromagnetic spectrum that do not carry any useful information from the source.

Peak Signal to Noise Ratio (PSNR) is an expression for the ratio between the maximum possible value (power) of a signal and the power of distorting noise that affects the quality of its representation. Because many signals have a very wide dynamic range, (the ratio between the largest and smallest possible values of a changeable quantity) the PSNR is usually expressed in terms of the logarithmic decibel scale.



CHAPTER 2

REVIEW OF THE LITERATURE

The literature review is presented in this chapter comprising the related concept, theories, background knowledge, and related work. Firstly, the X-ray production is described. The second part of this chapter explains mechanism of processing in CR. The quality evaluation for CR is clarified in the third section. The fourth section introduces mathematical model of noise. The fifth part expounds the concept of machine learning followed by introduction of neural network and fuzzy logic. The algorithms of noise reduction are elucidated in the seventh section. The last part explicates computer programming. The topics in this chapter are as follows.

- 2.1 X-ray production
- 2.2 Mechanism of processing in CR
- 2.3 Quality evaluation for CR
- 2.4 Mathematical model of noise
- 2.5 Machine learning
- 2.6 Neural network
- 2.7 Fuzzy logic
- 2.8 Algorithm of noise reduction
- 2.9 Computer programming

2.1 X-ray Production

2.1.1 The X-ray Tube

An X-ray machine circuit is a simplified schematic of a complete X-ray machine. The main circuit is composed of three general sections, the control console, the high voltage section, and the X-ray tube.

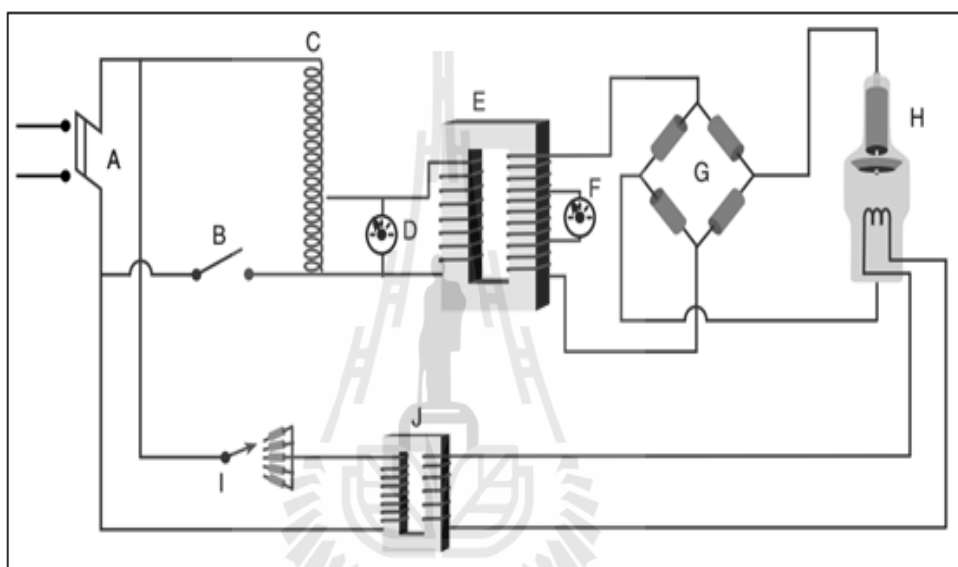
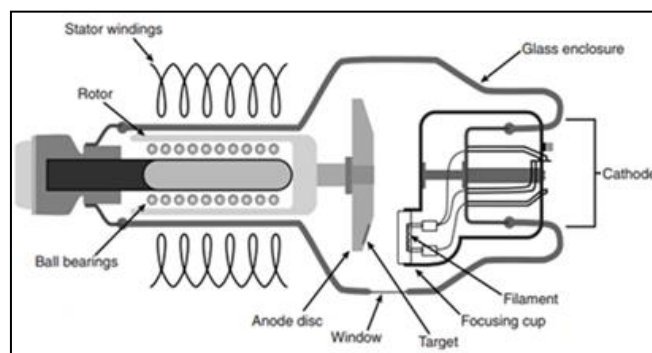


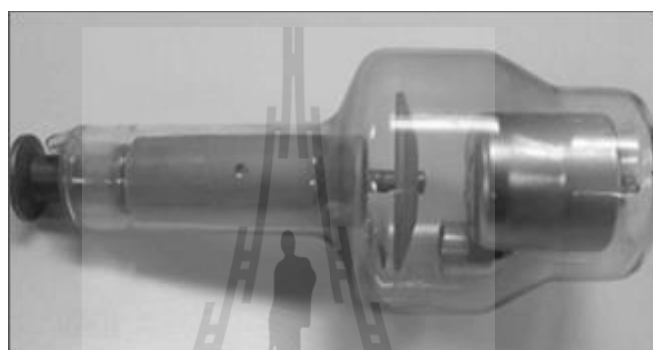
Figure 2.1 X-ray machine circuit (Quinn and Carroll, 2011)

Figure 2.1 as shown simplified schematic of a complete X-ray machine circuit, *A* is incoming lines and power switch, *B* is exposure switch and timer, *C* is autotransformer for kVp selection, *D* is pre-reading kVp meter, *E* is step-up transformer for high voltage, *F* is mA meter, *G* is rectification bridge, *H* is X-ray tube, *I* is bank of resistors for mA selection, and *J* is step-down transformer.

Figures 2.2 (a) and 2.2 (b) show a diagram and a photograph of a complete X-ray tube. The diagram shows the way in which the focusing cup and filaments are aligned to the anode in the tube.



(a)



(b)

Figure 2.2 X-ray tubes (Quinn and Carroll, 2011)

The source of free electrons is a filament wire heated sufficiently to produce thermionic emission. A minimum filament temperature of about 3700°F (2000°C) is required. The actual temperature of the filament and the rate of thermionic emission are predetermined by the mA station selected. When the rotor button is depressed, a current sufficient to generate this temperature flows through the filament. With added energy, electrons jump from their atoms and right off the wire, forming an electron cloud or space charge around the filament. The space charge constitutes electrons that are free to move across the X-ray tube to the anode. Some of the electrons fall back into the filament, but are replaced by other electrons jumping out such that a constant number of electrons hover within the cloud. This state of

equilibrium is called the space charge effect. The number of electrons is predetermined by setting the mA station. All of this process occurs through the filament circuit. In order to suddenly accelerate the electrons of the space charge in a direction toward the anode, an extremely high-voltage electromotive force is applied to the same filament. The electron cloud feels the force of the negative voltage behind it, and is repelled away from the filament. At the same time, the anode of the X-ray tube has acquired a positive charge from the same high-voltage circuit, and also pulls the electron cloud toward it. This potential difference in the tens of thousands of volts is so strong that the electrons can accelerate to more than one-half of the speed of light in just one inch of travel before reaching the anode disc. The anode disc, made of metals with very high atomic numbers, provides the means of precipitously decelerating these projectile electrons as they smash into it. By the law of conservation of energy, the energy lost by the sudden slowing down of the electrons cannot disappear but must be converted into another form. It is emitted from the anode in the form of electromagnetic radiation waves, including infrared, visible light, ultraviolet waves and X-rays. Unfortunately, the entire process is not very efficient. Only 1 percent of the radiation emitted is in the form of useful diagnostic X-rays. The other 99 percent is emitted from the X-ray tube and its housing in the form of wasted heat (Quinn and Carroll, 2011; Bushberg, Seibert, Leidholdt and Boone, 2002).

2.1.2 Bremsstrahlung X-ray Generation

If the electron passes near the atomic nucleus, the positive attraction of the nucleus will cause it to brake or slow down. This deceleration in the speed of the electron represents a loss of kinetic energy, and that energy which is lost is emitted as an X-ray photon. X-rays produced by this interaction are called bremsstrahlung or

braking radiation in German, and they account for the vast majority of the overall X-ray beam (Quinn and Carroll, 2011; Bushberg et al., 2002).

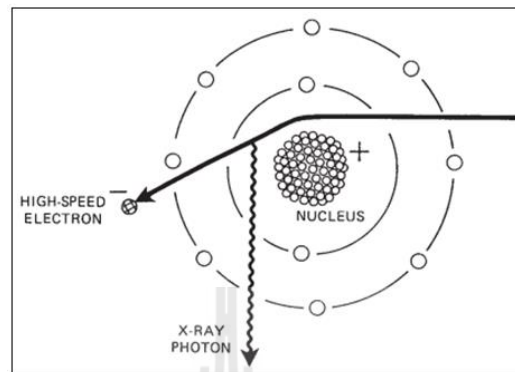


Figure 2.3 The bremsstrahlung interaction (Quinn and Carroll, 2011)

High speed electrons may pass by the nucleus at various distances from it. The closer an electron approaches to the nucleus, the greater will be the deceleration of the electron, due to the stronger pulling force of the nucleus. As shown in Figure 2.3, the attractive force of the nucleus also causes the electron to bend in its path of travel toward the nucleus. The greater the deceleration of the electron, the more it deviates from its original direction, and the more kinetic energy is lost. Thus, the closer the electron passes by the nucleus, the higher will be the energy of the emitted X-ray. Bremsstrahlung, occurring at various distances from the nucleus, produces a wide range of X-ray energies and is thus responsible for the heterogeneous or poly energetic nature of the X-ray beam. Heterogeneity contributes to the differential absorption X-rays within the patient's body by different tissues. It is just this differential absorption which provides subject contrast to the remnant X-ray beam and makes the radiographic image possible (Quinn and Carroll, 2011; Bushberg et al., 2002).

The X-ray beam must first pass through a number of materials which effectively act as filters. These include the anode itself, from which each X-ray must escape without being absorbed by another tungsten or rhenium atom. They include the glass window of the X-ray tube and the oil surrounding it, a beryllium window filter, an added aluminum filter normally placed between the X-ray tube and the collimator box, the mirror in the collimator, and other parts of the collimator. All of these filters absorb the X-rays with the lowest energies, so that the remaining bremsstrahlung portion of the emitted X-ray beam is graphed like Figure 2.4 (Quinn and Carroll, 2011; Bushberg et al., 2002).

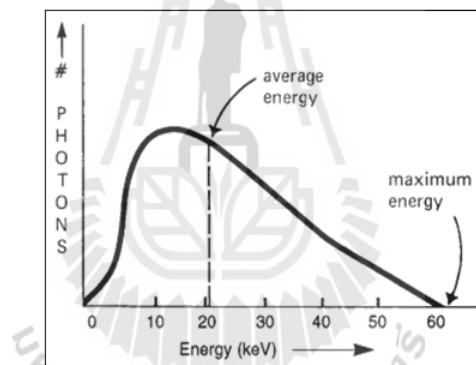


Figure 2.4 The bremsstrahlung X-ray spectrum (Quinn and Carroll, 2011)

Figure 2.4, fewer X-rays are produced at low energies due to filtration, and fewer X-rays are produced at high energies because of the statistical distribution of bremsstrahlung X-rays production. This leaves a bell shaped curve which is somewhat lopsided toward the left, so that the average kV within the beam is roughly one third of the set peak kilovoltage (kVp). The total number of X-rays producing is represented by the total area under the curve. This area covers the wide range of energies needed to produce subject contrast within the X-ray beam as it passes

through the patient's body tissues, rendering a full range of information for the image (Quinn and Carroll, 2011; Bushberg et al., 2002).

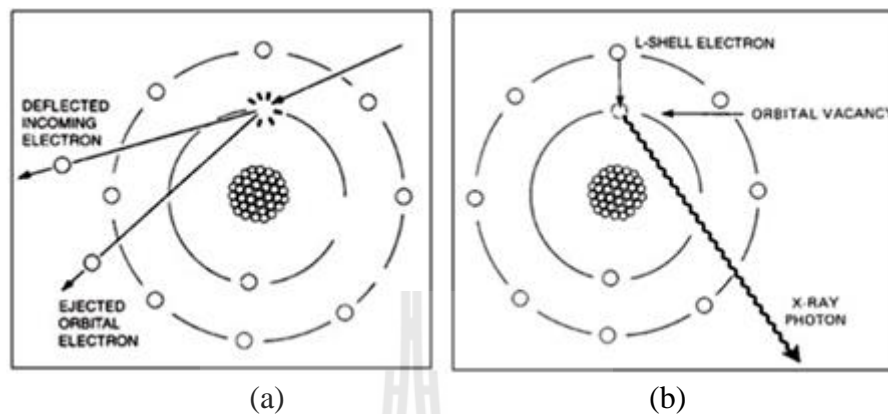


Figure 2.5 The characteristic interaction in the x-ray tube (Quinn and Carroll, 2011)

2.1.3 Characteristic X-ray Generation

Characteristic X-rays depend entirely on the difference in energy levels between different orbital shells in the atom. The atoms in the X-ray tube anode, the second possibility for the projectile electron is that it might interact with one of the atoms' orbital electrons. When it passes near an orbital electron, its repulsive negative charge can eject the orbital electron out of its orbit, leaving a vacancy in that electron shell of the atom (Fig. 2.5 (a)). The atom, left with a positive charge, will eventually pull in another electron to return to a neutral state. In the meantime, the vacancy created in this specific shell will be filled by any electron available from higher orbits. As the atom attempts to return to its ground state, the state with the least energy, electrons from outer orbits will fall down into vacancies that are closer to the nucleus. When an electron falls from an outer orbit down into an inner orbit, there is a loss of potential energy. By the law of conservation of energy, this potential energy cannot merely disappear, but must be converted into some other form of energy. It is emitted

as a characteristic X-ray (Fig. 2.5 (b)). Characteristic radiation makes up only a small portion of the overall X-ray beam, but since it can possess high energies that penetrate through the patient to the detectors, these X-rays are still important in producing a radiographic image (Quinn and Carroll, 2011; Bushberg et al., 2002).

Figure 2.5, in step (a), a projectile electron collides with and dislodges an orbital electron from the atom, in step (b), the atom pulls down an electron from a higher shell to fill the vacancy left. As this electron drops into a lower orbit, it loses potential energy which is emitted as an X-ray.

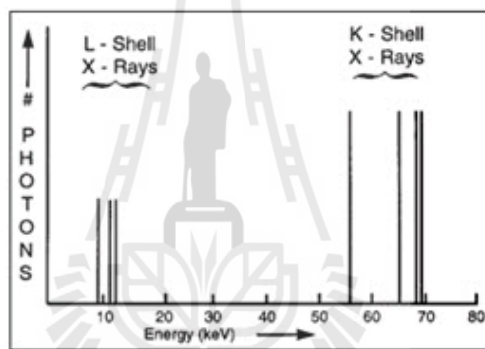


Figure 2.6 The characteristic X-ray spectrum (Quinn and Carroll, 2011)

Figure 2.6 plots the spectrum of characteristic X-rays production in tungsten. Inherent filtration will remove virtually all of the 2 kV and 3 kV X-rays, so these do not show up on the graph. Filtration also removes most of the 9 and 12 kV X-rays, so the graph plots them but showing a reduced number. Those characteristic X-rays having 57, 66, 68, and 69 kV largely escape the X-ray tube and are considered part of the useful X-ray beam. At each of these energies, a fairly high quantity of characteristic X-rays is produced, so they show up on the graph as tall spikes (Quinn and Carroll, 2011; Bushberg et al., 2002).

2.1.4 Interaction of X-ray with Matter

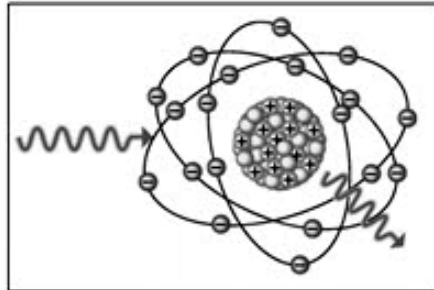


Figure 2.7 The coherent scattering (Sherer, Visconti, Ritenour, and Haynes, 2014)

1) Coherent Scattering

Coherent scattering (Fig. 2.7), the incoming low energy X-ray photon interacts with an atom and transfers its energy by causing some or all of the electrons of the atom to vibrate momentarily. The electrons then radiate energy in the form of electromagnetic waves. These waves nondestructively combine with one another to form a scattered wave, which represents the scattered photon. Its wavelength and energy, or penetrating power, are the same as those of the incident photon. Generally, the emitted photon may change in direction less than 20 degrees with respect to the direction of the original photon (Quinn and Carroll, 2011; Bushberg et al., 2002; Sherer et al., 2014).

2) Photoelectric Absorption

Photoelectric absorption, on encountering an inner-shell electron in the K or L shells, the incoming X-ray photon surrenders all its energy to the electron and the photon ceases to exist. The atom responds by ejecting the electron, called a photoelectron, from its inner shell, thus creating a vacancy in that shell. To fill the opening, an electron from an outer shell drops down to the vacated inner shell by

releasing energy in the form of a characteristic photon. Then, to fill the new vacancy in the outer shell, another electron from the shell next farthest out drops down and another characteristic photon is emitted, and so on until the atom regains electrical equilibrium. There is also some probability that instead of a characteristic photon, an Auger electron will be ejected (Quinn and Carroll, 2011; Bushberg et al., 2002; Sherer et al., 2014).

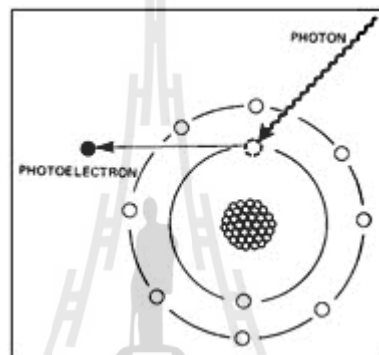


Figure 2.8 The photoelectric effect (Quinn and Carroll, 2011)

Figure 2.8, photoelectric absorption is the most important mode in the interaction between X-ray and the atoms of the patient's body in the energy range used in diagnostic radiology because this interaction is responsible for both the patient's dose and contrast in the image. During the process of photoelectric absorption, the kinetic energy of the incident photon is completely absorbed as it interacts with and ejects an inner shell electron of biologic tissue from its orbit. The newly ejected photoelectron possesses kinetic energy and can ionize other atoms it encounters until its energy is spent. After losing an electron, the original ionized atom is unstable and attempts to re-stabilize. This occurs as an electron from a higher shell drops down and fills the vacancy in the inner shell by releasing energy as a

characteristic photon. This cascading effect of electrons dropping down to fill existing shell vacancies continue until the original atom regains its stability (Quinn and Carroll, 2011; Bushberg et al., 2002; Sherer et al., 2014).

3) Compton Scattering

In the Compton process, an incoming X-ray photon interacts with a loosely bound outer electron of an atom of the irradiated object. On encountering the electron, the incoming X-ray photon surrenders a portion of its kinetic energy to dislodge the electron from its outer shell orbit, thereby ionizing the biologic atom. The freed electron, called a Compton scattered electron, or secondary, or recoil electron, possesses excess kinetic energy and is capable of ionizing other atoms. It loses its kinetic energy by a series of collisions with nearby atoms and finally recombines with an atom that needs another electron. This usually occurs within a few micrometers of the site of the original Compton interaction (Quinn and Carroll, 2011; Bushberg et al., 2002; Sherer et al., 2014).

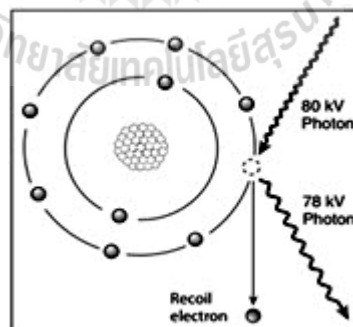


Figure 2.9 The Compton effect (Quinn and Carroll, 2011)

Figure 2.9 is Compton scattering, on encountering a loosely bound outer shell electron, the incoming X-ray photon surrenders a portion of its kinetic

energy to dislodge the electron from its orbit. The energy degraded X-ray photon then continues on its way but in a new direction. The high speed electron ejected from its orbit is called a Compton scattered electron, or secondary or recoil electron.

4) Pair Production

Pair production does not occur unless the energy of the incident X-ray photon is at least 1.022 Mega electron Volts (MeV). The incoming photon strongly interacts with the nucleus of the atom of the irradiated object and disappears. In the process, the energy of the photon is transformed into two new particles, a negatron (electron) and a positron. The negatron eventually recombines with any atom that needs another electron. The positron interacts destructively with a nearby electron. During the interaction, the positron and the electron annihilate each other, with their rest masses converted into energy, which appears in the form of two 0.511 MeV photons, each moving in the opposite direction as shown in Figure 2.10 (Bushberg et al., 2002; Sherer et al., 2014).

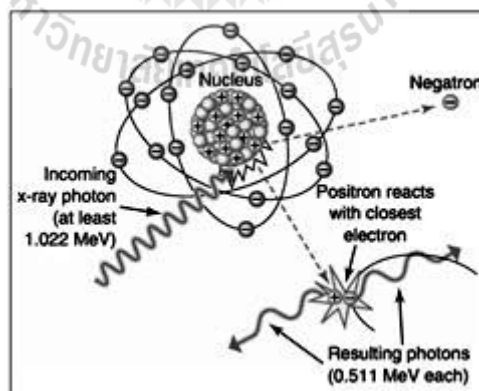


Figure 2.10 The pair production (Sherer et al., 2014)

5) Photodisintegration

Photodisintegration is an interaction that occurs at more than 10 MeV in high energy radiation therapy treatment machines. As with pair production, this energy range is also far higher than useful diagnostic energies. An incoming high energy photon collides with the nucleus of the atom of the irradiated object and absorbs all the photon's energy. This energy excess in the nucleus creates an instability that is usually alleviated by the emission of a neutron (Sherer et al., 2014).

2.1.5 Attenuation and Subject Contrast

Attenuation is the partial absorption of the X-ray beam, the reduction in intensity that occurs as the X-ray beam traverses a body part. General attenuation of the X-ray beam includes all three of the interactions explained in the previous section, since both the absorption and the scattering of X-rays can prevent them from reaching the image receptor (Quinn and Carroll, 2011; Bushberg et al., 2002).

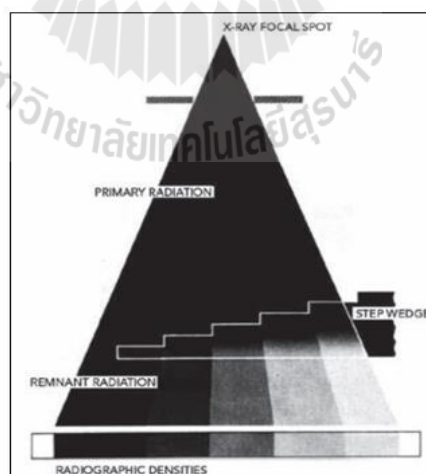


Figure 2.11 The attenuation of an X-ray beam by a homogeneous object
(Quinn and Carroll, 2011)

Figure 2.11 demonstrates the attenuation of an X-ray beam by a homogeneous object, a step wedge made of pure aluminum. Since the material is of uniform consistency throughout, differences in the remnant radiation beam are entirely due to the changing thickness of the steps in the block of aluminum. Primary radiation, striking the first and thinnest step is only slightly attenuated, and the receptor plate behind it receives high radiation exposure. As each step gets thicker, more attenuation occurs and less radiation exposure reaches the receptor plate (Quinn and Carroll, 2011; Bushberg et al., 2002).

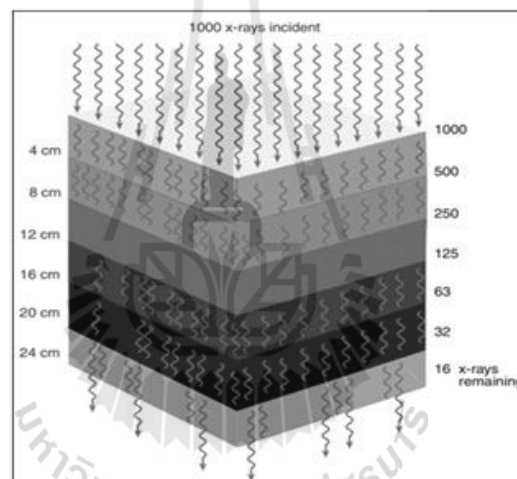


Figure 2.12 The attenuation of an X-ray beam by soft tissues (Quinn and Carroll, 2011)

Figure 2.12, the progressive, exponential attenuation of an X-ray beam as it passes through soft tissues of the body. Each 4 to 5 cm of tissue thickness reduces the X-ray intensity to about one half. The compensating rule for radiographic technique is to double technique for every 4 cm increase in body part thickness. Figure 2.12 shows this progressive attenuation of the X-ray beam as it passes through

a fairly homogeneous body tissue, such as muscle tissue, which possesses close to the same molecular atomic number and physical density as liquid water. The attenuation is about 50 percent for every 4 to 5 centimeters of soft tissue thickness. At 4 cm depth, only 500 of the original 1000 X-rays incident upon the body surface remain. At 8 cm, half of these, 250, remain, and so on until, after passing through the full thickness of a 24 centimeter abdomen, only 16 X-rays remain of the original 1000. This is 1.6 percent penetration through the body, which is close to the actual situation (Quinn and Carroll, 2011).

Subject contrast is produced by the differential absorption between various tissues of the body. The physical differences between these tissues are already present before the X-ray beam strikes them. Simply put a tissue such as bone stands out from the background of soft tissues because the bone attenuates more X-rays than soft tissue does. This general attenuation of X-rays can be due to either absorption of the X-rays by the tissue or to scattering of the X-rays by the tissue either way, the X-ray photon is prevented from reaching the image receptor. All interactions within the patient, whether photoelectric, Compton, or coherent scattering, represent some degree of absorption of the overall X-ray beam. All interactions attenuate the beam (Quinn and Carroll, 2011).

Changes in the energy levels of the X-ray beam, controlled primarily by the selected kVp, alter the penetration characteristics of the X-rays. Penetration is the opposite of attenuation. As kVp is increased and more penetration is achieved, the subject contrast between different tissues is lessened, but more different type soft tissues can also be demonstrated between the extremes of black and white within the image. This is referred to as lengthened gray scale. As subject contrast is decreased,

gray scale is increased. These effects are due to the penetration of the beam versus the overall attenuation factor, and will hold true regardless of the particular prevalence of the photoelectric effect or the Compton scattering. However, there are implications for the relative prevalence of these two interactions as study subject contrast (Quinn and Carroll, 2011).

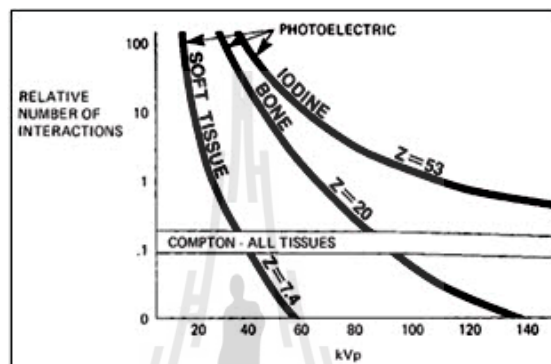


Figure 2.13 The relative predominance of photoelectric and Compton interactions in various tissues at increasing levels of kVp (Quinn and Carroll, 2011)

Figure 2.13 shows the relative predominance of photoelectric and Compton interactions in various tissues at increasing levels of kVp. While Compton interactions occur at about the same rate for all tissues, photoelectric interactions occur in much greater numbers in substances with higher atomic numbers such as bone and iodine. However, they still drop quickly as kVp increases (Quinn and Carroll, 2011).

2.2 Mechanism of Processing in CR

The CR uses same exposure routine as traditional film radiography: by absorption of X-ray, a latent image is generated in PSP Imaging Plate (IP). The latent

image is stable in hours under room temperature. The Imaging Plate, like film, can be handled with a light tight cassette. In order to enhance the X-ray absorption efficiency at high energies, metallic screens are usually used together with IP within a cassette. After exposure, the IP is introduced into an optical scanner by users. With the scanning of the finely focused laser light (raster scanning), the latent image stored in IP is released by means of PSL. The emitted signal is guided into photomultiplier by an optical fiber, and then converted into a digital image. An intense light is used in the last step to erase the unreleased information, and then the Imaging Plate can be reused. An Imaging Plate can be reused thousands of times.

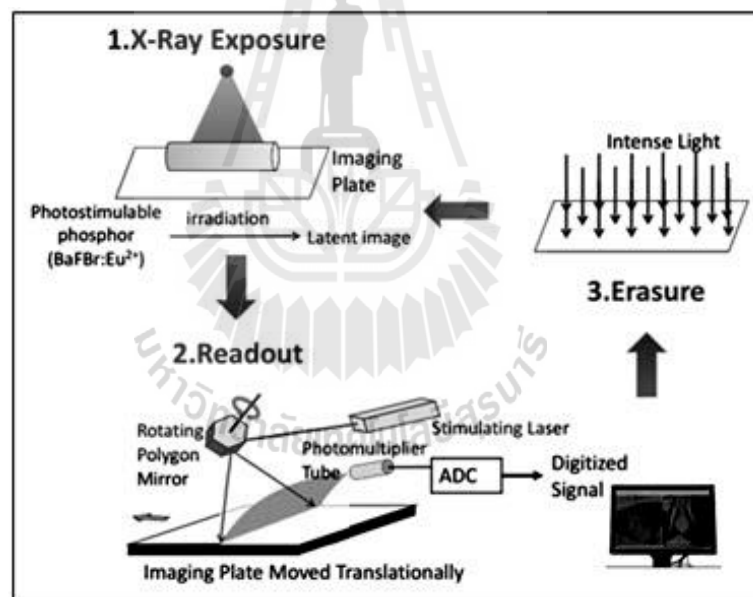


Figure 2.14 Computed Radiography cycle

Figure 2.14 is computed radiography procedure, during exposure, an Imaging Plate is used to receive the transmitted X-ray image creating a latent image (which is stable in hours under room temperature); as a second step, the Imaging Plate is introduced into an laser scanner, and the latent image is released and digitized

resulting in a final digital image which can be viewed through monitors; intense light is used in the last step to erase the residual image in Imaging Plate (Leblans, Vandenbroucke and Willems, 2011).

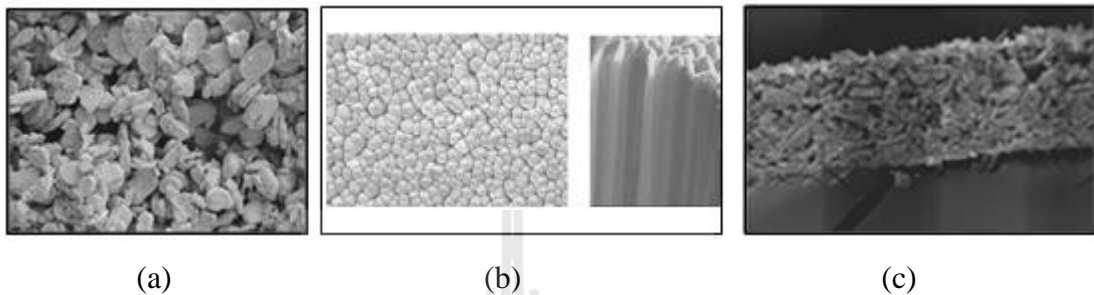


Figure 2.15 Substance element medium of three different type Imaging Plates
(Leblans et al., 2011)

Imaging Plate is the recording medium of the latent image, and the CR image depends massively on IP's property. Today's existing Imaging Plates can be categorized into three families: powder (or granular) plate, needle structured plate and glass ceramic plate (Figure 2.15 (a), (b), and (c), respectively). Powder plates are the most common commercial Imaging Plate, in which the phosphor (e.g. BaFBr: Eu²⁺) grains (of about 5 μm diameter) are held in a polymer binder. In needle plates, there is no use of binder, the phosphor crystals (e.g. CsBr: Eu²⁺) are grown into needles (about 5 to 10 μm diameter and 400 to 500 μm length (Leblans et al., 2011) which act as light guides. Hence strong light scattering can be avoided leading to better image quality than a powder plate of the same thickness. The glass ceramic type IP is not yet commercialized nowadays, in which nano or micro crystallites (e.g. BaCl: Ce³⁺) are doped into a glassy material. Due to the transparency of the glass ceramic material, the light scattering can be greatly reduced resulting in good spatial resolution.

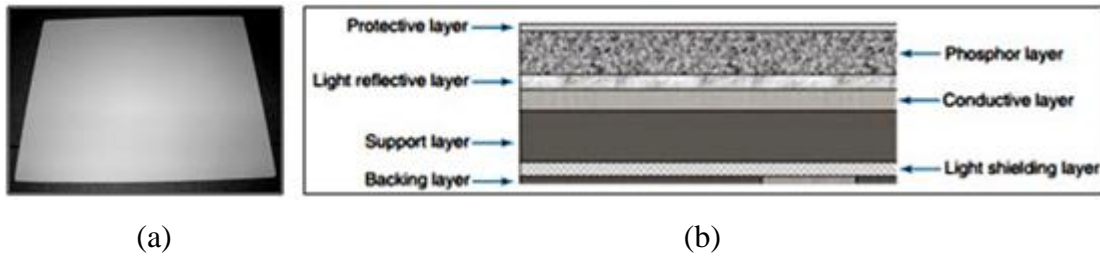


Figure 2.16 Imaging Plate and construction (Carter and Veale, 2010)

The CR cassette looks like the conventional radiography cassette. It consists of a durable, lightweight plastic material. The cassette is backed by a thin sheet of aluminum that absorbs X-rays. Instead of intensifying screens inside, there is antistatic material that protects against static electricity buildup, dust collection, and mechanical damage to the plate. In CR, the radiographic image is recorded on a thin sheet of plastic known as the Imaging Plate (Carter and Veale, 2010).

The Imaging Plate consists of several layers as shown in Figure 2.16 (Carter and Veale, 2010).

(1) A protective layer is a very thin, tough, clear plastic that protects the phosphor layer.

(2) A phosphor active layer is a layer of photostimulable phosphor that traps electrons during exposure. It is usually made of phosphors from the barium fluorohalide family (e.g., barium fluorohalide, chlorohalide, or bromohalide crystals). This layer may also contain a dye that differentially absorbs the stimulating light to prevent as much spread as possible and functions much the same as dye added to conventional radiographic screens.

(3) A reflective layer is a layer that sends light in a forward direction when released in the cassette reader. This layer may be black to reduce the spread of stimulating light and the escape of emitted light. Some detail is lost in this process.

(4) A conductive layer is a layer of material that absorbs and reduces static electricity.

(5) A color layer that newer plates may contain a color layer, located between the active layer and the support that absorbs the stimulating light but reflects emitted light.

(6) A support layer is a semi rigid material that gives the imaging sheet some strength.

(7) A backing layer is a soft polymer that protects the back of the cassette.



Figure 2.17 CR reader

The patient is X-rayed exactly the same way as in conventional radiography. The patient is then exposed using the proper combination of kVp, mAs, and distance. The difference lies in how the exposure is recorded. In CR, the remnant beam interacts with electrons in the barium fluorohalide crystals contained within the

Imaging Plate. This interaction stimulates, or gives energy to, electrons in the crystals, allowing them to enter the conductive layer, where they are trapped in an area of the crystal known as the color or phosphor center. This trapped signal will remain for hours, even days, although deterioration begins almost immediately. In fact, the trapped signal is never completely lost. That is, a certain amount of an exposure remains trapped so that the Imaging Plate can never be completely erased. However, the residual trapped electrons are so few in number that they do not interfere with subsequent exposures. With CR systems, no chemical processor or darkroom is necessary. Instead, following exposure, the cassette is fed into a CR reader (Figure 2.17) that removes the Imaging Plate and scans it with a laser to release the stored electrons. A laser, or light amplification of stimulated emission of radiation, is a device that creates and amplifies a narrow, intense beam of coherent light (Figure 2.18).

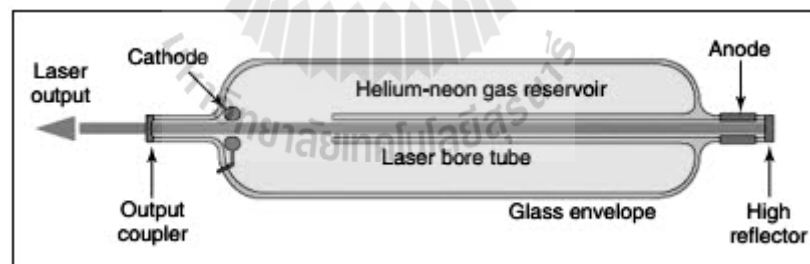


Figure 2.18 Laser construction (Carter and Veale, 2010)

The atoms or molecules of a crystal such as ruby or garnet or of a gas, liquid, or other substance are excited so that more of them are at high energy levels rather than low energy levels. Surfaces at both ends of the laser container reflect energy back and forth as atoms bombard each other, stimulating the lower energy atoms to

emit secondary photons in the same frequency as the bombarding atoms. When the energy builds sufficiently, the atoms discharge simultaneously as a burst of coherent light. It is coherent because all of the photons are traveling in the same direction at the same frequency. The laser requires a constant power source to prevent output fluctuations. The laser beam passes through beam shaping optics to an optical mirror that directs the laser beam to the surface of the Imaging Plate as shown in Figure 2.19 (Carter and Veale, 2010).

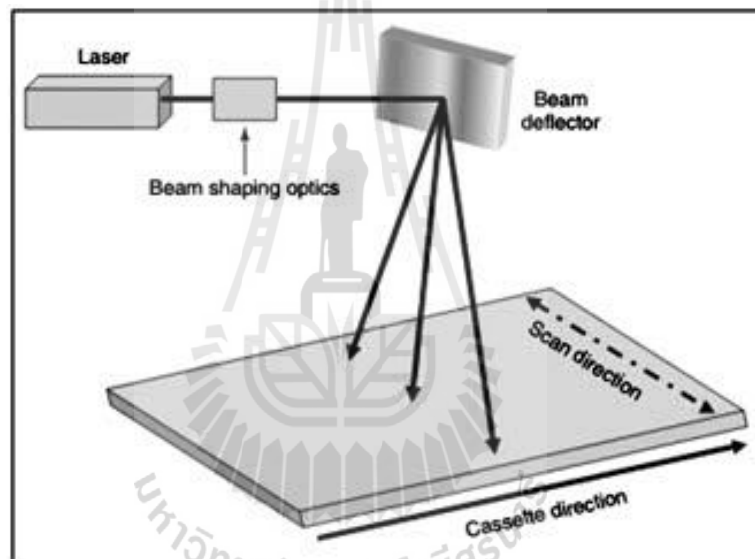


Figure 2.19 CR reader laser optics (Carter and Veale, 2010)

When the cassette is put into the reader, the Imaging Plate is extracted and scanned with a helium laser beam or, in more recent systems, solid state laser diodes. This beam, about 100 μm wide with a wavelength of 633 nm (or 670 to 690 nm for solid state), scans the plate with red light in a raster pattern and gives energy to the trapped electrons.

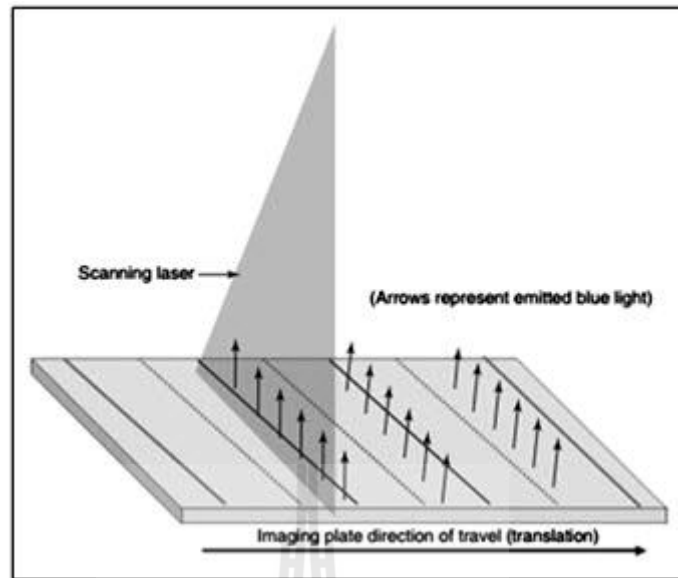


Figure 2.20 The laser scans Imaging Plate (Carter and Veale, 2010)

The red laser light is emitted at approximately 2 eV, which is necessary to energize the trapped electrons. This extra energy allows the trapped electrons (Figure 2.20) to escape the active layer where they emit visible blue light at the energy of 3 eV as they relax into lower energy levels. As the Imaging Plate moves through the reader, the laser scans across the Imaging Plate multiple times. The plate movement through the scanner is known as translation because it moves in a parallel manner at a certain rate through the reader. This scan process produces lines of light intensity information that are detected by a photomultiplier that amplifies the light and sends it to a digitizer. The translation speed of the plate must be coordinated with the scan direction of the laser, or the spacing of the scan lines will be affected. The action of moving the laser beam across the Imaging Plate is much like holding a flashlight at the same height and moving it back and forth across a wall. The more angled the

beam is, the more elliptical the shape of the beam. The same thing happens with the reader laser beam as it scans (Carter and Veale, 2010).

This means that if this change in the beam shape were ignored, the output of the screen would differ from the middle to the edges, resulting in differing spatial resolution and inconsistent output signals, depending on the position and angle of the laser beam. To correct this, the beam is shaped by special optics that keeps the beam size, shape, and speed largely independent of the beam position. A beam deflector moves the laser beam rapidly back and forth across the Imaging Plate to stimulate the phosphors. Mirrors are used to ensure that the beam is positioned consistently. Because the type of phosphor material in the the Imaging Plate has an effect on the amount of energy required, the laser and the Imaging Plate should be designed to work together. The light collection optics direct the released phosphor energy to an optical filter and then to the photo detector (Figure 2.21). Although there will be variances among manufacturers, the typical throughput is 50 cassettes/hr. Some manufacturers claim up more than one (Carter and Veale, 2010).

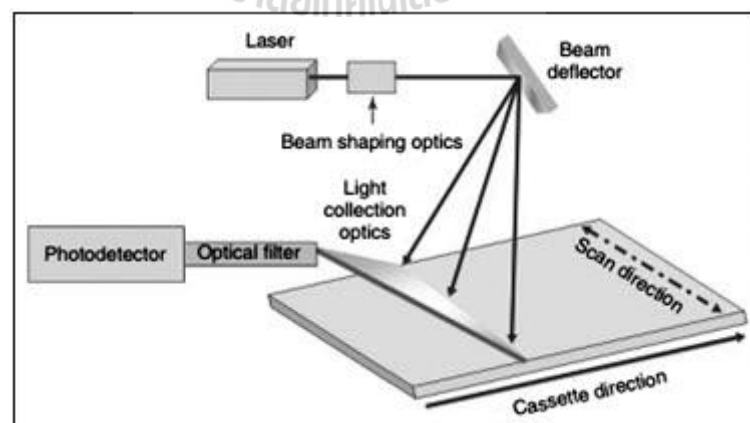


Figure 2.21 Laser optics (Carter and Veale, 2010)

The digitizing a signal, such as the light signal from the photomultiplier, that is talking about assigning a numerical value to each light photon. As humans, that once experience the world analogically that see the world as infinitely smooth gradients of shape and colors. Analog refers to a device or system that represents changing values as continuously variable physical quantities. A typical analog device is a watch that hands move continuously around the face and are capable of indicating every possible time of day. In contrast, a digital clock is capable of representing only a finite number of times (e.g., every tenth of a second). In the process of digitizing the light signal, each phosphor storage center is scanned, and the released electrons enter a digitizer that divides the analog image into squares (matrix) and assigns each square in the matrix a number based on the brightness of the square. Each square is called a pixel or picture element. The typical number of pixels in a matrix ranges from about 512×512 to 1024×1024 for CT but can be as large as 2500×2500 for radiography. The more pixels there are, the greater the image resolution. The image is digitized both by position (spatial location) and by intensity (gray level). Each pixel contains bits of information, and the number of bits per pixel that define the shade of each pixel is known as bit depth. If a pixel has a bit depth of 8, then the number of gray tones that pixel can produce is 2 to the power of the bit depth, or 2^8 , or 256 shades of gray. Therefore how many photons are detected will determine where it will be located in the matrix in conjunction with the amount of gray level or bit depth. Some CR systems have bit depths of 10 or 12, resulting in more shades of gray. Each pixel can have a gray level between 0 (2^0-1) and 4095 ($2^{12}-1$). The gray level will be a factor in determining the quality of the image. The amount of detail present in any image is known as its spatial resolution. Just as the crystal size and thickness of the

phosphor layer determine resolution in film/screen radiography, phosphor layer thickness and pixel size determine resolution in CR. The thinner the phosphor layer, the higher the resolution. In film/screen radiography, resolution at its best is limited to 10 lp/mm. In CR, resolution is approximately 2.55 to 5 lp/mm, resulting in less detail. However, because the dynamic range, or the number of recorded densities, is much higher, the difference in resolution is more difficult to discern. In conventional radiography, speed is determined by the size and layers of crystals in the film and screen. In CR, speed is not exactly the same because there is no intensifying screen or film. The phosphors emit light according to the width and intensity of the laser beam as it scans the plate, resulting in a relative speed that is roughly equivalent to a 200 speed film/screen system. CR system speeds are a reflection of the amount of photostimulable luminescence (PSL) given off by the Imaging Plate while being scanned by the laser. For example, Fuji Medical Systems (Tokyo, Japan) reports that a 1 mR exposure at 80 kVp and a source to image distance of 72 inches will result in a luminescence value of 200, hence the speed number (Carter and Veale, 2010).

The process of reading the image returns most but not all of the electrons to a lower energy state, effectively removing the image from the plate. However, Imaging Plates are extremely sensitive to scatter radiation and should be erased to prevent a buildup of background signal. The plates should be run at least once a week under an erase cycle to remove background radiation and scatter. CR readers have an erasure mode that allows the surface of the Imaging Plate to be scanned without recoding the generated signal. Systems automatically erase the plate by flooding it with light to remove any electrons still trapped after the initial plate reading (Figure 2.22). Cassettes should be erased before using if the last time of erasure is unknown. Once

the Imaging Plate has been read, the signal is sent to the computer where it is preprocessed. The data then go to a monitor where the technologist can review the image, manipulate it if necessary (post-processing), and send it to the quality control (QC) station and ultimately to the PACS (Carter and Veale, 2010).

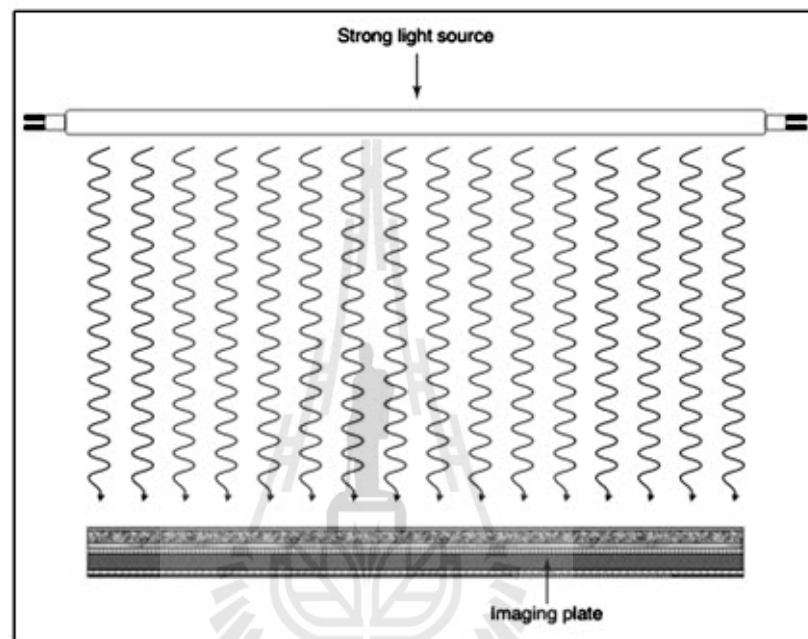


Figure 2.22 Erasing the Imaging Plate (Carter and Veale, 2010)

2.3 Commissioning and Routine Quality Control of CR

The performance tests for CR systems are used for general radiography. These include checks on the sensitivity of the system and image quality.

As the Imaging Plate has a wide dynamic range, changes to the sensitivity of the system or exposure levels may not be obvious to users. Thus, routine quality control (QC) of the system is particularly important.

Clinical image processing may adversely affect test images, for example, by introducing artifacts. For QC, it will generally be appropriate to use minimal image

processing, with a direct relationship between the exposure and mean pixel value. This relationship, known as the signal transfer property (STP), may not be linear.

Consistency checks are made easier by reducing the numbers of variables. If possible, always use the same X-ray tube and generator; choose an X-ray unit that is known to perform well. Check that its tube potential calibration is accurate and that its output is consistent over the range of exposures that are likely to be used (IPEM, 2005). Use consistent image processing and be aware that readers that are nominally the same may have different response. Assess image quality on the media uses clinically and archive and/or print reference images from commissioning.

2.3.1 Image Processing

The raw image is produced by digital imaging systems that are generally not of diagnostic quality due to the wide dynamic range of the detector and presence of non-uniformities in it. Pre-processing is undertaken on the raw image to compensate for detector artifacts.

1) Image Collection for CR Systems

Whilst there will be some degree of structural noise in CR system, it is not possible to apply a generic gain correction to the whole image. This is a result of difficulties in registering each image with a correction map. However, some manufacturers do apply a correction in the scan direction to account for variations in the light collection efficiency along this axis. However, in dark images where there is no signal, the correction matrix is applied to a uniform dark signal and creates bands in the image parallel to the scan direction corresponding to the sensitivities of the photomultiplier tubes.

2) Clinical Image Processing

The aforementioned pre-processing is used to correct for detector characteristics. Further processing is applied to make the image ready for presentation and suitable for clinical use. This may include collimation recognition, spatial frequency and grey scale processing. Ideally, the viewer should not need to undertake any further post-processing of the image.

3) Image Processing for Quality Control

Image processing can affect the results of QC. Where possible, no or minimal post-processing should be applied. In any case, the images should be processed in the consistent and reproducible manner. Clinical image processing may adversely affect test images, for example, by introducing artifacts (Honey and Mackenzie, 2009). Usually, only pre-processing corrections should be applied. Spatial frequency processing should be avoided as this is aimed at specific examinations and can adversely affect test images. Quantitative image quality tests require the imaging systems to be linear.

2.3.2 Signal Transfer Property

1) Linearizing the Image Data

The first step in any form of objective image quality analysis is measurement of the STP, which relates output parameter (usually a pixel value which is unitless) to the air kerma at the detector input plane. A system must have a linear or at least linearisable response to produce valid results for quantitative analysis measurements whether it is for simple measurements such as uniformity or for the more complex measurement of modulation transfer function (MTF). An image can be linearized by applying the inverse of the STP function. For systems with a linear (with

or without an offset), logarithmic, or power response (typically square root), the STP values and their respective inverses would be:

$$PV_{lin} = a + bK \Rightarrow K = \left(\frac{PV - a}{b} \right) \quad (2.1)$$

$$PV_{log} = a \ln(K) + b \Rightarrow K = \exp\left(\frac{PV - b}{a} \right) \quad (2.2)$$

$$PV_{power} = aK^b + c \Rightarrow K = \left(\frac{PV - c}{a} \right)^{\frac{1}{b}} \quad (2.3)$$

where a , b and c are constants, PV is pixel value and K is detector air kerma (μGy).

2) Measuring STP

The pixel value reading is taken from the pre-processed images. These image types are available on many digital imaging systems and are often given a distinct name such as 'RAW', 'For Processing' or 'Flat Field' images by the system.

There should be sufficient images obtained to cover the range of doses relevant to the tests being performed and to produce an accurate assessment of the STP. For a system known to have a straight line STP, then five images will generally be sufficient to specify the STP. For non-linear systems, the International Electrotechnical Commission (IEC) recommends that the ratio between adjacent dose steps should be a maximum of 1.26 (IEC, 2005). With careful measurement, the coefficient of correlation (R^2) of the STP should be greater than 0.99, though, for QC, a lower tolerance of greater than 0.98 should be satisfactory. Values of R^2 below 0.98 will increase the uncertainty of measurements involving linearizing the image data.

In cases where image processing is applied to the images, some of the quantitative tests may not produce meaningful results. Usually, on request, the supplier will set up an option with suitable image processing. There are several software packages available to measure mean pixel value, however, caution must be taken as even for the same image, some of them will give significantly different results.

2.3.3 Detector Dose Indicator

1) Defining Detector Dose Indicator

There are some fundamental differences between digital detectors and film/screen systems. One of the main advantages of digital imaging is the separation of the acquisition and display of the image. The majority of digital detectors have a wide dynamic range and so a wide range of exposures can therefore be displayed optimally. However, this can potentially obscure changes in the imaging system's sensitivity or give rise to situations where patient exposure is not optimal.

The Medicines and Healthcare products Regulatory Agency (MHRA) recommends that all digital systems for radiography in the UK have an indication of the absorbed dose at the detector (MHRA, 2006). Manufacturers have different names and definitions for such indices. In this report, such indices will be referred to as detector dose indicators (DDI). The DDI generally does not have a linear relationship with detector dose. The IEC has produced a standard for DDI (IEC, 2008), though this is not widely implemented at this time.

DDI can be considered as the digital equivalent of optical density for film/ screen systems. Previously with film imaging, changes in the film density could indicate problems with the film processing, automatic exposure control (AEC) or X-

ray system. Problems with the imaging system may be detected using the DDI. It is also a useful concept for undertaking QC, to test for changes in sensitivity to the imaging system and for testing the AEC.

Each manufacturer has their own approach to specifying clinically acceptable DDIs. These values can be used by radiographers to check acquired images. However, the DDI only indicates whether the Imaging Plate has received an appropriate exposure for that type of radiograph; it does not by itself show that the correct exposure parameters are set for a particular examination. It can also be affected by radiographic technique and image post-processing. There may be a range of acceptable DDI values for different examinations. DDI should be used in conjunction with another parameter such as dose-area product (DAP) for monitoring patient dose.

2) Routine Quality Control of DDI

DDI is dependent on beam quality (Tucker and Rezendes, 1997) and different manufacturers specify different beam conditions for DDI calibration, as shown in Table 2.1. At acceptance, the DDI calibration should be checked using the manufacturer's protocol. However, given the number of different definitions, it may be advisable to use a single, consistent method for routine QC on all types of digital systems. It may also be difficult to achieve the manufacturer's specified set-up, for example, if a low level of filtration and/ or a very long focus detector distance (FDD) is needed (to achieve a sufficiently low detector air kerma).

For consistency and simplicity, the standard set-up should reflect that used for image quality measurements. For CR, the time delay between exposure and readout could be reduced to 1 min as opposed to 2 to 15 min used in DDI calibration.

Table 2.1 Manufacturers' conditions for checking DDI calibration

	Agfa	Fuji	Kodak	Konica
Energy spectrum	75 kVp/ 1.5 mm Cu filtration	80 kVp/ no filtration	80 kVp/ 0.5 mm Cu + 1 mm Al filtration	80 kVp/ no filtration
Processing	2.5 min delay/ S = 200/ Exam type 'System Diagnostic'/ Processing 'Flat Field'/ Linear sensitometry	10 min delay/ Readout mode 'Semi- Auto'/ L = 1	5 min delay/ 'Pattern' mode	2 min delay/ 'Test 1'/ G = 2/F off
Linearized DDI value DAK _{DDI} (μGy)	DAK _{DDI} $= \left(\frac{SAL}{402} \right)^2$	DAK _{DDI} $= \left(\frac{1740}{S} \right)$	DAK _{DDI} = 10 ⁿ where $n = \frac{EI - C}{1000}$ C = 1060 for GP; C = 760 for HR	DAK _{DDI} $= \left(\frac{1740}{S} \right)$

Consistency between physics tests and more frequent user tests may make comparison of results easier and is recommended in IPEM 91 (IPEM, 2005). Ideally, the response of the detector should be tested at clinical beam energies. This is difficult to achieve in practice as tissue equivalent materials are bulky. Instead, metal filters attached to the tube exit port can provide suitable attenuation. This removes (to a large extent) the effect of variations in the filtration of X-ray tubes and provides

reasonably scatter-free conditions. This additional filtration is generally copper or aluminum.

3) Linearising DDI

The DDI is used to measure changes in the imaging system sensitivity and for testing the AEC. However, the DDIs are normally not linear and need to be linearized before they can be used quantitatively. Alternatively, tolerances can be set in terms of changes in the DDI.

A relationship between DDI compared to any suitable dose measurement, e.g. detector air kerma, entrance dose or dose-area product, must be measured. The IPEM recommended using DDI against DAK as the DDI calibration method. The linearized DDI value (DAK_{DDI}) can be found using the inverse of the measured relationship between DAK and DDI, in a similar manner to STP. The DDI is related not only to DAK but is dependent on the beam quality (Tucker and Rezentes, 1997), therefore at beam qualities different from the DDI calibration, DAK will be different from DAK_{DDI} .

2.3.4 Beam Quality

The STP and DDI will show some energy dependence. Ideally, the STP equation should be measured at the same beam quality as the image quality test.

Most departments already possess copper filters for testing image intensifiers. The spectrum recommended by IPEM 91 (IPEM, 2005) is 70 kVp with 1 mm copper on the tube exit port. The King's Centre for the Assessment of Radiological Equipment (KCARE, 2005) protocol for CR testing also uses these standard beam conditions. Table 2.2 compares this beam energy to RQA5. The American Association of Physicists in Medicine (AAPM) recommended 0.5 mm

copper plus 1 mm aluminum, with the copper positioned closest to the exit port of the X-ray tube (AAPM, 2006). Any kVp filter combination can be used if it is felt to be more relevant to the clinical use of the system, provided it is used consistently.

Table 2.2 Comparison of standard beam spectra for testing

Spectrum	Filter	kVp	1 st HVL (mm Al)
IPEM 91	1 mm Cu	70	~7.7
AAPM	0.5 mm Cu/ 1 mm Al	75	~7.1
RQA5	21 mm Al	Nominally 70	7.1

2.3.5 Commissioning and Quality Control

The QC measurements should be undertaken as detailed in the following sub-sections using standard conditions. The following conditions should be used unless specified otherwise:

- Position the Imaging Plate a long way from the X-ray tube, ideally > 150 cm
- Minimize backscatter as much as possible; use a sheet of lead rubber or spacers behind the Imaging Plate (AAPM, 2006)
- Use a QC cassette
- Set a field size that will just cover the largest cassette size
- Attach any additional filtration at the tube housing exit
- Standardize beam conditions should be used, e.g. 70 kVp, 1 mm Cu and detector air kerma of 10 μ Gy.

Table 2.3 Commissioning tests for CR

Test parameter	Acceptable level
DDI calibration	20%
Signal transfer properties	Simple relationship
DDI repeatability	CV of $DAK_{DDI} < 10\%$
Matching of CR Imaging Plate	DAK_{DDI} varies by $< 20\%$ between Imaging Plate
Differences between CR readers	DAK_{DDI} varies by $< 20\%$ between CR readers
Dark noise	Agfa: SAL < 100 Fuji: Pixel value < 280 Kodak: EI < 80 (GP plates) EI < 380 (HR plates) Konica: Pixel value > 3975
Measured uniformity	STP corrected ROI values within mean $\pm 10\%$
Erasure cycle efficiency	No visible ghost image
Threshold contrast detail detectability	Compare with data from other systems tested or published data
Variation of noise with detector air kerma	Compare with data from other systems tested
Signal-to-noise ratio	Compare with data from other systems tested
Limiting high contrast spatial resolution	$\geq 0.70/2\Delta p$ for scan and sub-scan measurements
Laser beam function	Edge continuous across whole image; uniform 'stair' characteristics across whole image

Table 2.3 list the some test parameters recommended to commission CR systems and documents a level of acceptability for each.

2.4 Mathematical Model of Noise

Rudin, Osher, and Fatemi (1992) presented a mathematical de-noising model which is called the ROF model used the additive noise model and was based on calculus of variation. The ROF model is considered u as the solution to a problem of calculus of variation which minimized the functional

$$F(u) = \iint_{\Omega} \left(\sqrt{u_x^2 + u_y^2} \right) dA + \lambda \iint_{\Omega} (u - \tilde{u})^2 dA, \quad (2.4)$$

where $\Omega \in R^2$ is the domain of the image functions and λ is a chosen parameter. By calculus of variations, the solution of this problem is obtained when the Euler-Lagrange differential equation is satisfied, i.e.

$$\frac{\partial}{\partial x} \left(\frac{u_x}{\sqrt{u_x^2 + u_y^2}} \right) + \frac{\partial}{\partial y} \left(\frac{u_y}{\sqrt{u_x^2 + u_y^2}} \right) + \lambda(u - \tilde{u})^2 = 0, \quad (2.5)$$

where $\frac{\partial u}{\partial N} = 0$ on $\partial\Omega$ and N is the normal vector to the boundary $\partial\Omega$.

Le, Chatrand and Asaki (2007) adapted the ROF model to reduce Poisson noise in the image by minimizing the functional

$$G(u) = \beta \iint_{\Omega} \left(\sqrt{u_x^2 + u_y^2} \right) dA + \iint_{\Omega} (u - \tilde{u} \ln u) dA. \quad (2.6)$$

The Euler-Lagrange differential equation for solving this problem is

$$\frac{\partial}{\partial x} \left(\frac{u_x}{\sqrt{u_x^2 + u_y^2}} \right) + \frac{\partial}{\partial y} \left(\frac{u_y}{\sqrt{u_x^2 + u_y^2}} \right) + \frac{1}{\beta u} (u - \tilde{u})^2 = 0, \quad (2.7)$$

where $\frac{\partial u}{\partial N} = 0$ on $\partial\Omega$ and N is the normal vector to the boundary $\partial\Omega$.

Gravel, Beaudoin, and De Guise, (2004) developed a method to study the statistical properties of the noise found in various medical images. The method is specifically designed for types of noise with uncorrelated fluctuations. Such signal fluctuations generally originated in the physical processes of imaging rather than in the tissue textures. Various types of noise (e.g., photon, electronics, and quantization) often contributed to degrade medical images; the overall noise is generally assumed to be additive with a zero-mean, constant-variance Gaussian distribution. However, statistical analysis suggested that the noise variance could be better modeled by a nonlinear function of the image intensity depending on external parameters related to the image acquisition protocol. They presented a method to extract the relationship between an imaged intensity and the noise variance and to evaluate the corresponding parameters. The method is applied successfully to magnetic resonance images with different acquisition sequences and to several types of X-ray images.

Altas, Louis, and Belward, (1995) presented a variational approach to the problem of finding suitable radiometric image transformations that optimized desirable characteristics of the output image histogram. This variational approach can be interpreted as the minimization of the cumulative spacing between histogram bars in the least squares sense subject to some weight function. Most of the common histogram transformation procedures used in remote sensing applications can be

deduced from this general variational approach with an appropriate choice of the weight function.

Zhang, Cao, Zhang, and Wang, (2014) proposed an adaptive total variation (TV) model by introducing the steerable filter into the TV-based diffusion process for image filtering. The local energy measured by the steerable filter can effectively characterize the object edges and ramp regions and guide the TV-based diffusion process so that the new model behaves like the TV model at edges and leads to linear diffusion in flat and ramp regions. This way, the proposed model can provide a better image processing tool which enables noise removal, edge-preserving, and staircase suppression.

Sun, Chen, and Qiao, (2014) studied a general non-local de-noising model using multi kernel induced measures. Noises are inevitably introduced in digital image acquisition processes, and thus image de-noising was still a hot research problem. Different from local methods operating on local regions of images, the non local methods utilized non local information (even the whole image) to accomplish image de-noising. Due to their superior performance, the non local methods have recently drawn more and more attention in the image de-noising community. However, these methods generally did not work well in handling complicated noises with different levels and types. Inspired by the fact in machine learning field that multi kernel methods were more robust and effective in tackling complex problems than single-kernel ones, the authors established a general non local de-noising model based on multi kernel induced measures (GNLMKIM for short), which provided them a platform to analyze some existing and design new filters. With the help of GNLMKIM, the authors reinterpreted two well known non local filters in the united

view and extend them to their novel multi kernel counterparts. The comprehensive experiments indicated that these novel filters achieved encouraging de-noising results in both visual effect and PSNR index.

Gaussian noise is statistical noise having a probability density function (PDF) equal to that of the normal distribution, which is also known as the Gaussian distribution. In other words, the values that the noise can take on are Gaussian distributed. The probability density function *PDF* of a Gaussian random variable z is given by:

$$p(z) = \frac{1}{\sigma\sqrt{2\pi}} e^{-\frac{(z-\mu)^2}{2\sigma^2}} \quad (2.8)$$

where z represents gray level, μ is the mean value and σ is its standard deviation.

A special case is white Gaussian noise, in which the values at any pair of times are identically distributed and statistically independent. In communication channel testing and modeling, Gaussian noise is used as additive white noise to generate additive white Gaussian noise. In telecommunications and computer networking, communication channels can be affected by wideband Gaussian noise coming from many natural sources, such as the thermal vibrations of atoms in conductors. Principal sources of Gaussian noise in digital images arise during acquisition e.g., sensor noise caused by poor illumination, high temperature, transmission e.g., electronic circuit noise (Gonzalez and Woods, 2002).

In probability theory and statistics, the Poisson distribution, named after French mathematician Siméon Denis Poisson, was a discrete probability distribution that expressed the probability of a given number of events occurring in a fixed interval of time and/or space if these events occur with a known average rate and

independently of the time since the last event. The Poisson distribution can also be used for the number of events in other specified intervals such as distance, area or volume (Haight, 1967).

Individual photon detections can be treated as independent events that follow a random temporal distribution. As a result, photon counting is a classic Poisson process, and the number of photons N measured by a given sensor element over a time interval t is described by the discrete probability distribution

$$P(z) = \frac{e^{-\lambda t} (\lambda t)^z}{z!} \quad (2.9)$$

where λ is the expected number of photons per unit time interval, which is proportional to the incident scene irradiance. This is a standard Poisson distribution with a rate parameter λt that corresponds to the expected incident photon count. The uncertainty described by this distribution is known as photon noise (Bushberg, et al, 2002).

Poisson noise prevailed in situations where an image is created by the accumulation of photons over a detector. Typical examples are found in standard X-ray films, CCD cameras, and infrared photometers (Gravel, Beaudoin, and De Guise, 2004).

Linear Intensity Scaling: the following analysis assumes a pixel intensity corresponding to the number of monochromatic photons captured in a given amount of time. Real X-ray beams are not monochromatic and have energy spectra showing strong characteristic emission lines superimposed over a Bremsstrahlung radiation background (Bushberg, et al, 2002). The energy deposited at a pixel location (the image intensity) did not correspond exactly to the number of captured monochromatic

photons since the X-rays follow a compound Poisson noise process. Whereas the number of X-rays followed a Poisson noise distribution, the X-ray energy converted counts follow a compound Poisson noise distribution due to the wide spectrum of the energy. For a Poisson process of mean X (where X represents the number of captured photons), the expectation value for the variance is

$$\sigma_x^2 = X \quad (2.10)$$

because a recorded image is usually linearly rescaled to accommodate a given range in grey scales, the relation between the intensity X reaching the detector and the recorded intensity I is

$$I = \gamma X + \delta \quad (2.11)$$

where γ and δ are constants. The corresponding variance σ_I^2 varies linearly with the intensity I (Gravel et al, 2004).

$$\sigma_I^2 = \gamma I - \delta \gamma \quad (2.12)$$

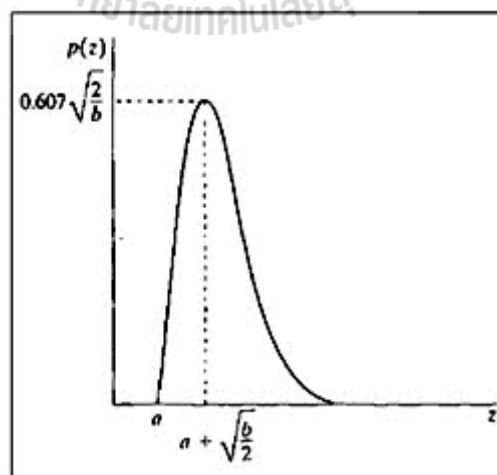


Figure 2.23 The PDF of Rayleigh noise (Gonzalez and Woods, 2002)

Rayleigh noise, the PDF is given by

$$P(z) = \begin{cases} \frac{2}{b}(z-a)e^{-(z-a)^2/b} & \text{for, } z \geq a \\ 0 & \text{for, } z < a. \end{cases} \quad (2.13)$$

The mean and variance of this density are given by

$$\mu = a + \sqrt{\pi b/4} \quad (2.14)$$

and

$$\sigma^2 = \frac{b(4-\pi)}{4}. \quad (2.15)$$

Figure 2.23 is shown a plot of the Rayleigh density. Note the displacement from the origin and the fact that the basic shape of this density is skewed to the right. The Rayleigh density can be quite useful for approximating skewed histograms.

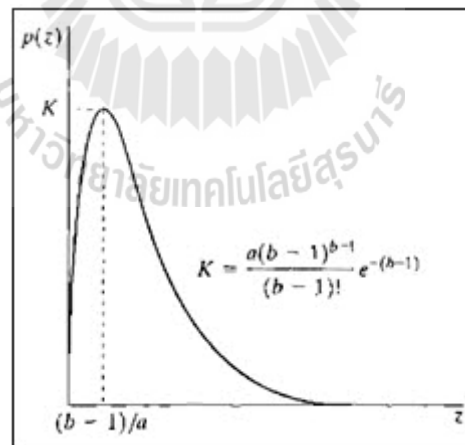


Figure 2.24 The PDF of gamma noise (Gonzalez and Woods, 2002)

Gamma or Erlang noise, The PDF of gamma noise is given

$$p(z) = \begin{cases} \frac{a^b z^{b-1}}{(b-1)!} e^{-az} & \text{for, } z \geq 0 \\ 0 & \text{for, } z < 0 \end{cases} \quad (2.16)$$

where the parameters are such that $a > 0, b$ is a positive integer, and "!" indicates factorial. The mean and variance of this density are given by

$$\mu = \frac{b}{a} \quad (2.17)$$

and

$$\sigma^2 = \frac{b}{a^2}. \quad (2.18)$$

Figure 2.24 is shown a plot of this density. Although this equation often is referred to as the gamma density, strictly speaking this is correct only when the denominator is the gamma function, $\Gamma(b)$. When the denominator is as shown, the density is more appropriately called the Erlang density.

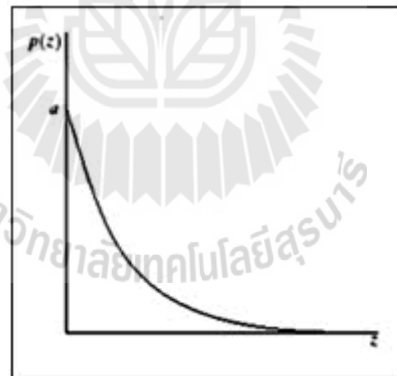


Figure 2.25 The PDF of exponential noise (Gonzalez and Woods, 2002)

Exponential noise, the PDF is given by

$$p(z) = \begin{cases} ae^{-az} & \text{for } z \geq 0 \\ 0 & \text{for } z < 0 \end{cases} \quad (2.19)$$

where $a > 0$. The mean and variance of this density function are

$$\mu = \frac{1}{a} \quad (2.20)$$

and

$$\sigma^2 = \frac{1}{a^2}. \quad (2.21)$$

The PDF of exponential noise is shown in Figure 2.25.

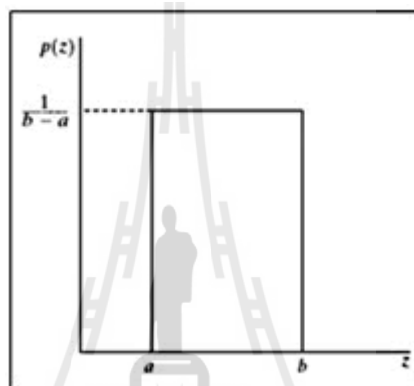


Figure 2.26 PDF of uniform noise (Gonzalez and Woods, 2002)

Figure 2.26 is shown a plot of the uniform density. Uniform noise, the PDF is given by

$$p(z) = \begin{cases} \frac{1}{b-a} & \text{if } a \leq z \leq b \\ 0 & \text{otherwise} \end{cases}. \quad (2.22)$$

The mean of this density function is given by

$$\mu = \frac{a+b}{2} \quad (2.23)$$

and its variance by

$$\sigma^2 = \frac{(b-a)^2}{12} \quad (2.24)$$

Impulse valued noise or salt and pepper noise is also called data drop noise because statistically its drop the original data values. This noise is also referred as salt and pepper noise. However, the image is not fully corrupted by salt and pepper noise instead of some pixel values are changed in the image. Although in noisy image, there is a possibilities of some neighbors did not change (Boyat and Joshi, 2015).

$$p(g) = \begin{cases} Pa & \text{for } g = a \\ Pb & \text{for } g = b \\ 0 & \text{otherwise} \end{cases} \quad (2.25)$$

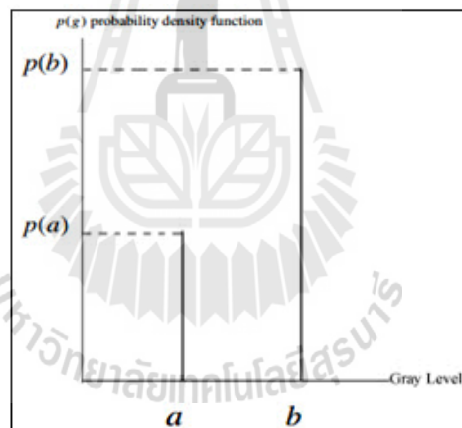


Figure 2.27 PDF of salt and pepper noise (Boyat and Joshi, 2015)

Figure 2.27 is shown the PDF of salt and pepper noise, if mean is zero and variance is 0.05. The two spike is met two, one is for bright region where gray level is less that called region a and another one is dark region where gray level is large that called region b , the PDF values are minimum and maximum in region a and region b , respectively (Koli and Balaji, 2013). Salt and pepper noise generally corrupted the

digital image by malfunctioning of pixel elements in camera sensors, faulty memory space in storage, errors in digitization process and many more.

2.5 Machine Learning for Classification

Classification techniques can be grouped into two main types: supervised and unsupervised. Supervised classification relies on having example pattern or feature vectors which have already been assigned to a defined class. Using a sample of such feature vectors as our training data, a classification system was designed with the intention and hope that new examples of feature vectors which were not used in the design would subsequently be classified accurately. In supervised classification then, the aim is to use training examples to design a classifier which generalizes well to new examples. By contrast, unsupervised classification did not rely on possession of existing examples from a known pattern class (Solomon and Breckon, 2011).

A decision tree is defined as a connected, acyclic, undirected graph, with a root node, zero or more internal nodes (all nodes except the root and the leaves), and one or more leaf nodes (terminal nodes with no children), which would be termed as an ordered tree if the children of each node are ordered (normally from left to right). A tree is termed as univariate, if it splits the node using a single attribute or a multivariate, if it uses several attributes. A binary tree is an ordered tree such that each child of a node is distinguished either as a left child or a right child and no node has more than one left child or more than one right child. For a binary decision tree, the root node and all internal nodes have two child nodes. All non-terminal nodes contain splits (Cormen, Leiserson, Rivest, and Stein, 2009).

The basic algorithm for decision tree is a greedy algorithm that constructs decision tree in a top-down recursive divide and conquer manner. Assuming that a training set consisting of feature vectors and their corresponding class labels are available, the decision tree is then constructed by partitioning the feature space in such a way as to recursively generate the tree. This procedure involves: create a root node; for each known feature value of the sample, partition the samples grow a branch node from the root node. And determining which nodes are terminal nodes (it is leaf node), assign class labels to terminal nodes. Obviously, the most important step is partition the samples to grow the branch node. One of the popular algorithms for design the decision tree is C4.5 (Quinlan, 1993). The information gain is used as the criterion for splitting the nodes. The feature attribute of the sample with the high information gain is chosen as the test attribute for the current node. This feature attribute minimizes the Information needed to classify the samples in the resulting partitions and reflects the least randomness in these partitions. It guarantees that a simple tree is found.

An Artificial Neural Network (ANN) is an information processing paradigm that is inspired by the way biological nervous systems, such as the brain, process information. The key element of this paradigm is the novel structure of the information processing system. It is composed of a large number of highly interconnected processing elements (neurons) working in unison to solve specific problems. ANNs, like people, learn by example. An ANN is configured for a specific application, such as pattern recognition or data classification, through a learning process. Learning in biological systems involves adjustments to the synaptic connections that exist between the neurons.

Wang, Fan, Bhatt, and Davatzikos, (2010) presented a general methodology for high-dimensional pattern regression on medical images via machine learning techniques. Compared with pattern classification studies, pattern regression considers the problem of estimating continuous rather than categorical variables, and can be more challenging. It is also clinically important, since it can be used to estimate disease stage and predict clinical progression from images. In this work, adaptive regional feature extraction approach is used along with other common feature extraction methods, and feature selection technique is adopted to produce a small number of discriminative features for optimal regression performance. Then the Relevance Vector Machine (RVM) is used to build regression models based on selected features. To get stable regression models from limited training samples, a bagging framework is adopted to build ensemble basis regressors derived from multiple bootstrap training samples, and thus to alleviate the effects of outliers as well as facilitate the optimal model parameter selection. Finally, this regression scheme is tested on simulated data and real data via cross-validation. Experimental results demonstrate that this regression scheme achieves higher estimation accuracy and better generalizing ability than Support Vector Regression (SVR).

2.6 Artificial Neural Network

Artificial neural networks (Floreano and Mattiussi, 2008) are computational models implemented in software or custom-made hardware devices that attempt to capture the behavioral and adaptive features of biological nervous systems. An artificial neural network is composed of several interconnected units, or neurons (Figure 2.28). Some of these units receive information directly from the environment

(input units), some have a direct effect on the environment (output units), and others communicate only with units within the network (internal or hidden units).

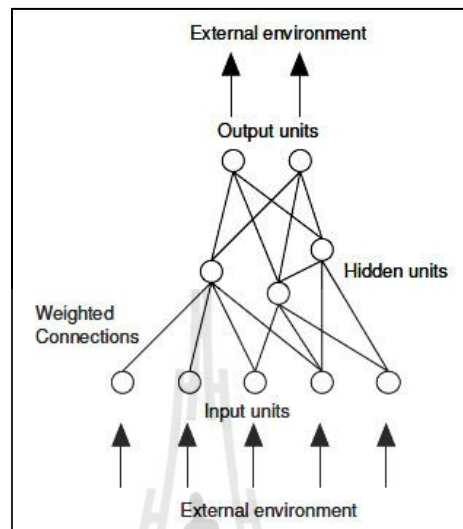


Figure 2.28 Generic neural network architecture (Floreato and Mattiussi, 2008)

Each unit implements a simple operation that consists in becoming active if the total incoming signal is larger than its threshold. An active unit emits a signal that reaches all units to which it is connected. The connection, or synaptic point, operates like a filter that multiplies the signal by a signed weight, also known as synaptic strength.

Whereas biological neurons are either inhibitory or excitatory and have the same effect on all neurons which they send signals to, artificial neurons can emit both negative and positive signals and thus the same neuron can establish both negative and positive synaptic connections with other neurons. There are two reasons for this difference. The first is that artificial neurons are mathematical objects that are not constrained by the physiological properties of biological neurons in order to achieve

the same functionality. The second is that an artificial neuron often models the average response of a population of biological neurons, which may include both excitatory and inhibitory neurons.

The response of an artificial neural network to an input from the environment depends on its architecture and pattern of connection strengths. The knowledge of the network is distributed across its connections. The behavior of the network is given by the pattern of activations of the neurons, which in some models can self-sustain and change over time even in the absence of input from the environment.

Neural networks learn by modification of synaptic strengths when presented with stimulation from the environment. Usually, learning requires several repeated presentations of the set of input patterns. There are several types of learning rules, each displaying specific functionalities and applicable to specific architectures. Typically, all synaptic connections within the artificial neural network change according to the same learning rule.

In addition to the ability of learning by exposition to examples (learning by demonstration), neural networks are often appreciated in engineering applications also for the following features.

(1) Robustness, neural networks are robust to various types of signal degradation, such as input noise or malfunctioning of connection and unit operation in hardware implementations. As the noise level increases, neural networks display graceful degradation by increasing the error rate more or less uniformly across the entire input domain or by making errors for specific input patterns while maintaining a correct response for all other patterns. Furthermore, neural networks can be incrementally trained to compensate for signal noise or damage to their components.

(2) Flexibility, neural networks are not domain specific, that is to say that a neural model can be applied to several types of problems (however, that does not mean that any type of neural network can be applied to any type of problem). Neural networks can be used to tackle problems for which there is not an analytical solution, but this presents the risk of giving up the effort of understanding the problem to find the comfort of a neural solution that does not increase our knowledge.

(3) Generalization, neural networks trained on a limited number of examples can provide the correct response to input patterns that share some similarity with training patterns, but were never seen before. This ability comes from the fact that neural networks store a larger number of input-output associations than the number of available synaptic strengths by extracting invariant features of the patterns. The ability of the network to generalize the response to a new pattern depends on the extent to which the new pattern can be described by the learned invariant features. The extraction of invariant features is also a common property of biological neural systems that allow them to operate consistently in continuously changing environments. From an engineering perspective, the ability to generalize to novel input patterns is very useful for those applications where it is impossible to obtain an exhaustive list of all situations that the system may be exposed to.

(4) Content-based retrieval, neural networks retrieve memories by matching contents and can do so even when the input patterns are incomplete or corrupted by noise. In some neural models, such as those derived from adaptive resonance theory (Grossberg, 1987), retrieval resembles the way in which humans operate: more familiar patterns are recognized faster than items that are different or seen less frequently. Instead, in conventional computer systems, data are retrieved using the

address of the electronic memory cells. If that number is corrupted or lost, the entire memory is lost.

Neural model, an artificial neuron is characterized by a set of connection strengths, a threshold, and an activation function (Figure 2.29). If we ignore transmission delays, the effect of a set of input signals \vec{x} on the postsynaptic neuron is equal to the product $\vec{w} \cdot \vec{x}$, where \vec{w} are the synaptic weights and can take any real value (both negative and positive). The net input, or activation a_i , of a neuron i is the sum of all weighted inputs from pre-synaptic neurons j :

$$a_i = \sum_{j=1}^N w_{ij} x_j. \quad (2.26)$$

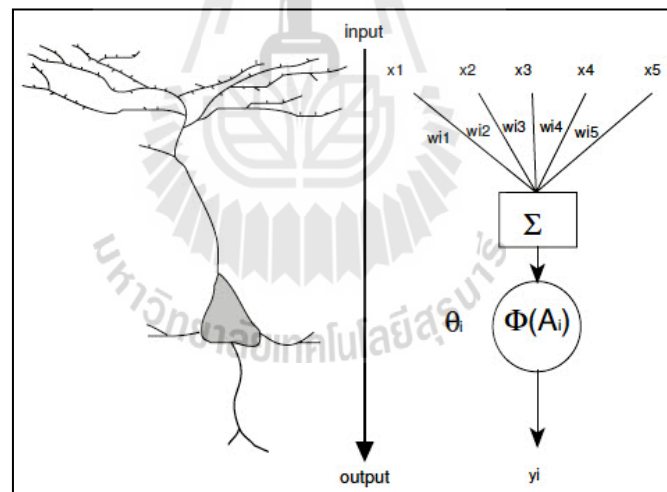


Figure 2.29 Schematic representation of a biological (pyramidal cell) and artificial neuron (Floreano and Mattiussi, 2008)

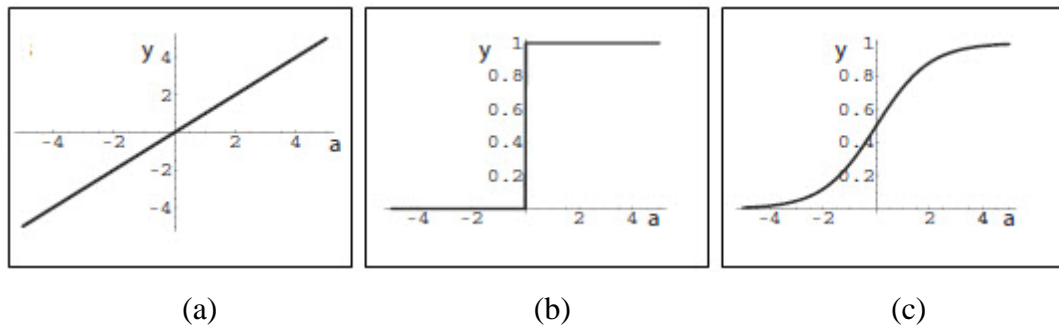


Figure 2.30 Activation functions, (a) linear, (b), threshold, and (c), sigmoid function

(Floreano and Mattiussi, 2008)

The output signal y_i is a function of the net input and of the neuron threshold \mathcal{G}_i , which is usually subtracted from the sum of weighted inputs:

$$y_i = \Phi(a_i) = \Phi\left(\sum_{j=1}^N w_{ij}x_j - \mathcal{G}_i\right). \quad (2.27)$$

The activation function $\Phi(\cdot)$ describes the response profile of the neuron and can take several different forms, (Figure 2.30) (a) linear, (b) step (threshold), and (c) sigmoid function. In the original formulation by McCulloch and Pitts (1943) neurons have a binary output (0 or 1) and the threshold is used as a hard delimiter to tell whether a neuron emits a signal.

$$\Phi(a_i) = \begin{cases} 1: \sum_{j=1}^N w_{ij}x_j > \mathcal{G}_i \\ 0: \text{otherwise} \end{cases} \quad (2.28)$$

A variation of this function is the bipolar activation where

$$\Phi(a_i) = \begin{cases} 1: \sum_{j=1}^N w_{ij}x_j > \mathcal{G}_i \\ -1: \text{otherwise} \end{cases} \quad (2.29)$$

Here the neuron can be in only one of two states and transmit only one bit of information. More information can be transmitted if the neuron could be in several states, as is the case for continuous activation functions. The output of a continuous activation function is a real number. In biological terms, this number could be interpreted either as the firing rate of the neuron over a short time window or as the sum of all excitatory and inhibitory outputs of a population of neurons at a given instant. The simplest continuous function is the linear model

$$\Phi(a_i) = k a_i \quad (2.30)$$

where k is a constant. In undesirable situations where the output of the neuron could grow indefinitely for example, if it has a positive feedback connection, this activation function can be constrained to operate within a given interval, such as $[0, 1]$ or $[-1, 1]$.

There are also several continuous and nonlinear activation functions that are used in complex neural architectures. One of the most common nonlinear functions is the sigmoid, or logistic, function

$$\Phi(a_i) = \frac{1}{1 + e^{-k a_i}} \quad (2.31)$$

where k is a scaling factor that determines the inclination of the slope as shown in Figure 2.30 (c) (for $k \rightarrow 0$ the function approximates a linear function; for $k \rightarrow \infty$ the function approximates a step function). The sigmoid function tends asymptotically to 0 and 1. A similar function is $\tanh(kA)$, which tends asymptotically to -1 and 1.

2.7 Fuzzy Logic

Fuzzy logic idea is similar to the human being's feeling and inference process. Unlike classical control strategy, which is a point to point control, fuzzy logic control is a range to point or range to range control. The output of a fuzzy controller is derived from fuzzifications of both inputs and outputs using the associated membership functions. A crisp input will be converted to the different members of the associated membership functions based on its value. From this point of view, the output of a fuzzy logic controller is based on its memberships of the different membership functions, which can be considered as a range of inputs.

The idea of fuzzy logic was invented by Professor L. A. Zadeh of the University of California at Berkeley in 1965 (Zadeh, 1965). This invention was not well recognized until Dr. E. H. Mamdani, who is a professor at London University, applied the fuzzy logic in a practical application to control an automatic steam engine in 1974 (Mamdani, 1999), which is almost ten years after the fuzzy theory was invented. Then, in 1976, Blue Circle Cement and SIRA in Denmark developed an industrial application to control cement kilns (Holmblad and Ostergaard, 1982). That system began to operation in 1982. More and more fuzzy implementations have been reported since the 1980s, including those applications in industrial manufacturing, automatic control, automobile production, banks, hospitals, libraries and academic education. Fuzzy logic techniques have been widely applied in all aspects in today's society.

To implement fuzzy logic technique to a real application requires the following three steps:

(1) Fuzzification, convert classical data or crisp data into fuzzy data or Membership Functions (MFs).

(2) Fuzzy Inference Process, combine membership functions with the control rules to derive the fuzzy output.

(3) Defuzzification, use different methods to calculate each associated output and put them into a table: the lookup table. Pick up the output from the lookup table based on the current input during an application.

Fuzzy set is only an extension of the concept of a classical or crisp set. The fuzzy set is actually a fundamentally broader set compared with the classical or crisp set. The classical set only considers a limited number of degrees of membership such as '0' or '1', or a range of data with limited degrees of membership. For instance, if a temperature is defined as a crisp high, its range must be between 27° C and higher and it has nothing to do with 21° C or even 16° C. But the fuzzy set will take care of a much broader range for this high temperature. In other words, the fuzzy set will consider a much larger temperature range such as from -18° C to higher degrees as a high temperature. The exact degree to which the -18° C can contribute to that high temperature depends on the membership function. This means that the fuzzy set uses a universe of discourse as its base and it considers an infinite number of degrees of membership in a set. In this way, the classical or crisp set can be considered as a subset of the fuzzy set.

Linguistic variable is some fuzzy set joining values sharing some common property, usually familiar to human beings. For example, if we consider outdoor temperatures, then warm could be a linguistic variable. A set of linguistic variables is used to represent the original domain set in terms of the variables. In the case of

outdoor temperatures, this set could be (cold, cool, just right, warm, hot): cold = {0, 0, 8}, cool = {0, 12, 20}, just right = {16, 20, 24}, warm = {20, 28, 36}, and hot = {32, 36, 40}.

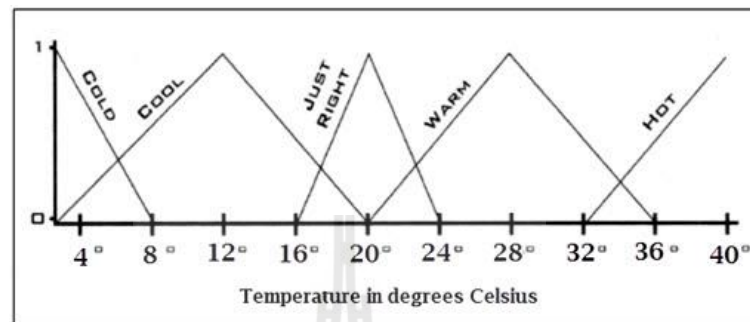


Figure 2.31 Membership function

Figure 2.31, fuzzification and membership functions: the fuzzy set is a powerful tool and allows us to represent objects or members in a vague or ambiguous way. The fuzzy set also provides a way that is similar to a human being's concepts and thought process. However, just the fuzzy set itself cannot lead to any useful and practical products until the fuzzy inference process is applied. To implement fuzzy inference to a real product or to solve an actual problem, as we discussed before, three consecutive steps are needed, which are fuzzification, fuzzy inference, and defuzzification.

Fuzzification is the first step to apply a fuzzy inference system. Most variables existing in the real world are crisp or classical variables. One needs to convert those crisp variables (both input and output) to fuzzy variables, and then apply fuzzy inference to process those data to obtain the desired output. Finally, in most cases,

those fuzzy outputs need to be converted back to crisp variables to complete the desired control objectives.

Generally, fuzzification involves two processes: derive the membership functions for input and output variables and represent them with linguistic variables. This process is equivalent to converting or mapping classical set to fuzzy set to varying degrees.

In practice, membership functions can have multiple different types, such as the triangular waveform, trapezoidal waveform, Gaussian waveform, bell-shaped waveform, sigmoid waveform and S-curve waveform. The exact type depends on the actual applications. For those systems that need significant dynamic variation in a short period of time, a triangular or trapezoidal waveform should be utilized. For those system that need very high control accuracy, a Gaussian or S-curve waveform should be selected.

The membership function of these temperatures is shown in Figure 2.32. To make thing simple, a triangular waveform is utilized for this type of membership function. A crisp cool temperature can be considered as a just right temperature to some degree in this fuzzy membership function representation. For instance, about 17° C will belong to cool and just right to about 0.4 degree. Some terminologies used for the membership function are also shown in Figure 2.32.

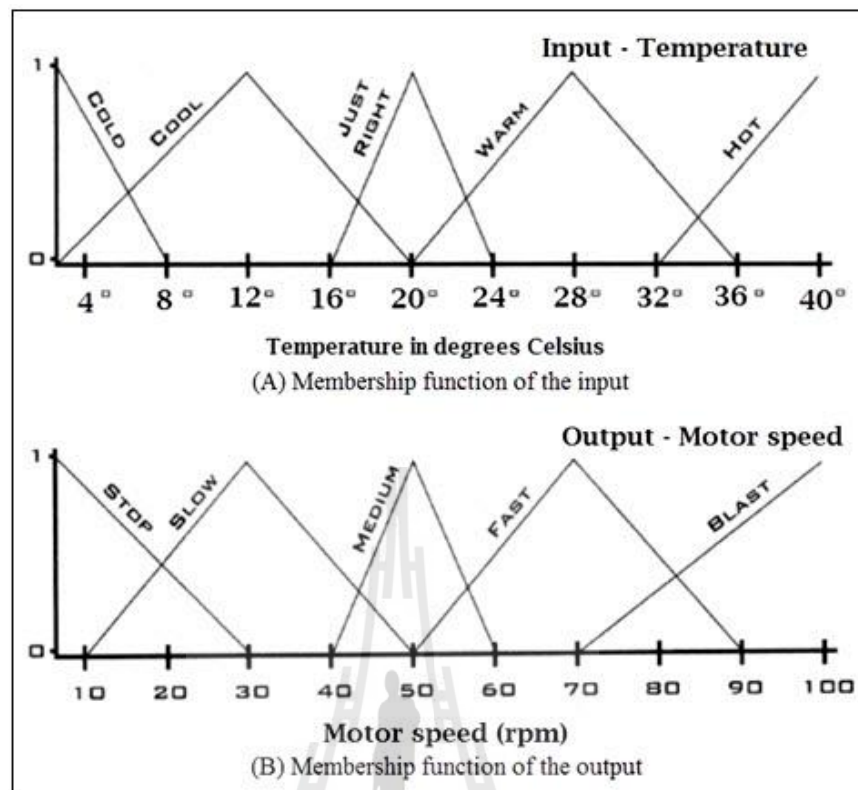


Figure 2.32 Input and output membership functions

Fuzzy control rule can be considered as the knowledge of an expert in any related field of application. The fuzzy rule is represented by a sequence of the form IF-THEN, leading to algorithms describing what action or output should be taken in terms of the currently observed information, which includes both input and feedback if a closed-loop control system is applied. The law to design or build a set of fuzzy rules is based on a human being's knowledge or experience, which is dependent on each different actual application.

A fuzzy IF-THEN rule associates a condition described using linguistic variables and fuzzy sets to an output or a conclusion. The IF part is mainly used to capture knowledge by using the elastic conditions, and the THEN part can be utilized

to give the conclusion or output in linguistic variable form. This IF-THEN rule is widely used by the fuzzy inference system to compute the degree to which the input data matches the condition of a rule.

Fuzzy mapping rules provide a functional mapping between the input and the output using linguistic variables. The foundation of a fuzzy mapping rule is a fuzzy graph, which describes the relationship between the fuzzy input and the fuzzy output. Sometimes, in real applications, it is very hard to derive a certain relationship between the input and the output, or the relationship between those inputs and outputs are very complicated even when that relationship is developed. Fuzzy mapping rules are a good solution for those situations. Fuzzy mapping rules work in a similar way to human intuition or insight, and each fuzzy mapping rule only approximates a limited number of elements of the function, so the entire function should be approximated by a set of fuzzy mapping rules. Still using our air conditioner system as an example, a fuzzy mapping rule can be derived as “*IF the temperature is cool, THEN the heater motor should be rotated fast*”.

For other input temperatures, different rules should be developed. For most actual applications, the input variables are commonly more than one dimension. For example, in our air conditioner system, the inputs include both current temperature and the change rate of the temperature. The fuzzy control rules should also be extended to allow multiple inputs to be considered to derive the output.

Defuzzification, the conclusion or control output derived from the combination of input, output membership functions and fuzzy rules is still a vague or fuzzy element, and this process is called fuzzy inference. To make that conclusion or fuzzy output available to real applications, a defuzzification process is needed. The

defuzzification process is meant to convert the fuzzy output back to the crisp or classical output to the control objective.

2.8 Algorithm of Noise Reduction

Spatial domain filtering, this is the traditional way to remove the noise from the digital images to employ the spatial filters. Spatial domain filtering is further classified into linear filters and non-linear filters.

2.8.1 Linear Filters

A mean or average filter is the optimal linear for Gaussian noise in the sense of mean square error. Linear filters tend to blur sharp edges, destroy lines and other fine details of image. It includes mean filter and Wiener filter.

Mean filter acts on an image by smoothing it. It reduces the intensity variations between the adjacent pixels. Mean filter is nothing just a simple sliding window spatial filter that replaces the centre value of the window with the average values of its all neighboring pixels values including itself. It is implemented with the convolution mask, which provides the results that is weighted sum of vales of a pixel and its neighbors. It is also called linear filter. The mask or kernel is square. Often 3×3 mask is used. If the coefficient of the mask sum is up to one, then the average brightness of the image is not changed. If the coefficient sum to zero, average brightness is lost, and it returns a dark image.

Weiner filter, Weiner filtering method requires the information about the spectra of noise and original signal and it works well only if the underlying signal is smooth. Weiner method implements the spatial smoothing and its model complexity control corresponds to the choosing the window size. $H(u, v)$ is the degradation

function and $H(u,v)^*$ is its conjugate complex. $G(u,v)$ is the degraded image. Functions $Sf(u,v)$ and $Sn(u,v)$ are power spectra of original image and the noise. Wiener filter assumes noise and power spectra of object a priori.

$$F(u,v) = [H(u,v) / H(u,v)^2 + [Sn(u,v) / Sf(u,v)]]G(u,v) \quad (2.32)$$

The Gaussian smoothing operator is a 2-D convolution operator that is used to blur images and remove detail and noise. In this sense it is similar to the mean filter, but it uses a different kernel that represents the shape of a Gaussian (bell-shaped) hump.

2.8.2 Non-linear Filters

With the non-linear filter, noise is removed without any attempts to explicitly identify it. Spatial filters employ a low pass filtering on the group of pixels with the assumption that noise occupies the higher region of frequency spectrum. Generally spatial filters remove the noise to reasonable extent but at the cost of blurring the images which in turn makes the edges in the picture invisible.

Median filter follows the moving window principle and uses 3×3 , 5×5 or 7×7 window. The median of window is calculated and the center pixel value of the window is replaced with that value.

2.9 Computer Programming

2.9.1 ImageJ

Prior to the release of ImageJ in 1997, a similar freeware image analysis program known as National Institutes of Health (Collins, 2007; Schneider, Rasband and Eliceiri, 2012) (NIH) image had been developed in Object Pascal for Macintosh

computers running pre-OS X operating systems. Further development of this code continues in the form of Image SXM, a variant tailored for physical research of scanning microscope images. A Windows version – ported by Scion Corporation (now defunct), so-called Scion Image for Windows – was also developed. Both versions are still available but – in contrast to NIH Image – closed-source.

ImageJ is a public domain, Java-based image processing program developed at the National Institutes of Health. ImageJ was designed with an open architecture that provides extensibility via Java plugins and recordable macros (Girish and Vijayalakshmi, 2004). Custom acquisition, analysis and processing plugins can be developed using ImageJ's built-in editor and a Java compiler. User-written plugins make it possible to solve many image processing and analysis problems, from three-dimensional live-cell imaging (Eliceiri and Rueden, 2005) to radiological image processing (Barboriak et al., 2005), multiple imaging system data comparisons (Rajwa et al., 2004) to automated hematology systems (Gering and Atkinson, 2004). ImageJ's plugin architecture and built-in development environment has made it a popular platform for teaching image processing.

ImageJ can be run as an online applet, a downloadable application, or on any computer with a Java 5 or later virtual machine. Downloadable distributions are available for Microsoft Windows, Mac OS, OS X, Linux, and the Sharp Zaurus PDA. The source code for ImageJ is freely available (Rueden and Eliceiri, 2007).

ImageJ can display, edit, analyze, process, save, and print 8-bit color and grayscale, 16-bit integer, and 32-bit floating point images. It can read many image file formats, including TIFF, PNG, GIF, JPEG, BMP, DICOM, and FITS, as well as raw formats. ImageJ supports image stacks, a series of images that share a single window,

and it is multithreaded, so time-consuming operations can be performed in parallel on multi-CPU hardware. ImageJ can calculate area and pixel value statistics of user-defined selections and intensity-thresholded objects. It can measure distances and angles. It can create density histograms and line profile plots. It supports standard image processing functions such as logical and arithmetical operations between images, contrast manipulation, convolution, Fourier analysis, sharpening, smoothing, edge detection, and median filtering. It does geometric transformations such as scaling, rotation, and flips. The program supports any number of images simultaneously, limited only by available memory.

2.9.2 MATLAB

Cleve Moler, the chairman of the computer science department at the University of New Mexico, started developing MATLAB (Matrix Laboratory) in the late 1970s (Moler, 2004). He designed it to give his students access to LINPACK and EISPACK without them having to learn Fortran. It soon spread to other universities and found a strong audience within the applied mathematics community. Jack Little, an engineer, was exposed to it during a visit Moler made to Stanford University in 1983. Recognizing its commercial potential, he joined with Moler and Steve Bangert. They rewrote MATLAB in C and founded MathWorks in 1984 to continue its development. These rewritten libraries were known as JACKPAC. In 2000, MATLAB was rewritten to use a newer set of libraries for matrix manipulation, LAPACK.

MATLAB was first adopted by researchers and practitioners in control engineering, Little's specialty, but quickly spread to many other domains. It is now

also used in education, in particular the teaching of linear algebra, numerical analysis, and is popular amongst scientists involved in image processing.

MATLAB is a multi-paradigm numerical computing environment and fourth-generation programming language. A proprietary programming language developed by MathWorks, MATLAB allows matrix manipulations, plotting of functions and data, implementation of algorithms, creation of user interfaces, and interfacing with programs written in other languages, including C, C++, Java, Fortran and Python.

Although MATLAB is intended primarily for numerical computing, an optional toolbox uses the MuPAD symbolic engine, allowing access to symbolic computing abilities. An additional package, Simulink, adds graphical multi-domain simulation and model-based design for dynamic and embedded systems. In 2004, MATLAB had around one million users across industry and academia. MATLAB users come from various backgrounds of engineering, science, and economics.

2.9.3 Weka

Waikato Environment for Knowledge Analysis (Weka) is a popular suite of machine learning software written in Java, developed at the University of Waikato, New Zealand. It is free software licensed under the GNU General Public License.

Weka is a workbench that contains a collection of visualization tools and algorithms for data analysis and predictive modeling, together with graphical user interfaces for easy access to these functions. The original non-Java version of Weka was a Tcl/Tk front-end to (mostly third-party) modeling algorithms implemented in other programming languages, plus data preprocessing utilities in C, and a Make file-based system for running machine learning experiments. This original version was

primarily designed as a tool for analyzing data from agricultural domains, but the more recent fully Java-based version (Weka 3), for which development started in 1997, is now used in many different application areas, in particular for educational purposes and research. Advantages of Weka include:

- (1) Free availability under the GNU General Public License.
- (2) Portability, since it is fully implemented in the Java programming language and thus runs on almost any modern computing platform.
- (3) A comprehensive collection of data preprocessing and modeling techniques.
- (4) Ease of use due to its graphical user interfaces.

Weka supports several standard data mining tasks, more specifically, data preprocessing, clustering, classification, regression, visualization, and feature selection. All of Weka's techniques are predicated on the assumption that the data is available as one flat file or relation, where each data point is described by a fixed number of attributes (normally, numeric or nominal attributes, but some other attribute types are also supported). Weka provides access to SQL databases using Java Database Connectivity and can process the result returned by a database query. It is not capable of multi-relational data mining, but there is separate software for converting a collection of linked database tables into a single table that is suitable for processing using Weka. Another important area that is currently not covered by the algorithms included in the Weka distribution is sequence modeling.

2.10 Related Work

Rampado, Isoardi and Ropolo (2006) studied quantitative assessment of computed radiography quality control parameters. Quality controls for testing the performance of Computed Radiography systems have been recommended by manufacturers and medical physicists' organizations. The purpose of this work was to develop a set of image processing tools for quantitative assessment of Computed Radiography quality control parameters. Automatic image analysis consisted in detecting phantom details, defining regions of interest and acquiring measurements. The tested performance characteristics included dark noise, uniformity, exposure calibration, linearity, low-contrast and spatial resolution, spatial accuracy, laser beam function and erasure thoroughness. CR devices from two major manufacturers, Kodak and Philips (Fuji) were evaluated. They investigated several approaches to quantify the detector response uniformity. They developed methods to characterize the spatial accuracy and resolution properties across the entire image area, based on the Fourier analysis of the image of a fine wire mesh. The implemented methods were sensitive to local blurring and allowed to detect a local distortion of 4% or greater in any part of an Imaging Plate. The obtained results showed that the developed image processing tools allow them to implement a quality control program for CR with short processing time and with absence of subjectivity in the evaluation of the parameters.

Samei et al. (2001) studied performance evaluation of computed radiography systems. Recommended methods to test the performance of computed radiography digital radiographic systems have been recently developed by the AAPM Task Group No. 10. Included are tests for dark noise, uniformity, exposure response, laser beam function, spatial resolution, low-contrast resolution, spatial accuracy, erasure

thoroughness, and throughput. The recommendations may be used for acceptance testing of new CR devices as well as routine performance evaluation checks of devices in clinical use. The purpose of this short communication is to provide a tabular summary of the tests recommended by the AAPM Task Group, delineate the technical aspects of the tests, suggest quantitative measures of the performance results, and recommend uniform quantitative criteria for the satisfactory performance of CR devices. The applicability of the acceptance criteria is verified by tests performed on CR systems in clinical use at five different institutions. This paper further clarifies the recommendations with respect to the beam filtration to be used for exposure calibration of the system, and the calibration of automatic exposure control systems.

Santhanam and Radhika (2005) studied probabilistic neural network a better solution for noise classification. Classification is one of the major research areas of neural networks. Classification problems play a major role in the field of business, science, industry and medicine. Neural networks have emerged as an important tool for classification. The recent research activities which use neural networks for classification have established that neural networks are a promising alternative to various conventional classification methods. The advantage of neural networks is that it makes use of self-adaptive methods to adjust to the data without any explicit specification. The use of a Probabilistic Neural Network (PNN) to classify the image noise, based on the statistical features is discussed. There are different types of image noise, include salt and pepper noise, Gaussian white noise, non-Gaussian white noise, speckle noise, quantization noise and shot noise. The characteristics of the noise are to be studied to analyze the type of the noise in an image. Noise identification is vital for

determining the de-noising procedure for an image, which leads to image enhancement for further processing. Noise classification in digital image processing is a must so as to identify the suitable filters for smoothing the image for further processing. The use of Probabilistic Neural Network to classify the noise present in an image after extracting the statistical features like skewness and kurtosis is explored in this article. When the noises are classified accurately, identification of the filter becomes an easy task. The use of PNN for classification of noise is explored in this article. Their databases have been used to test the performance of the network and the experiments have been carried out in MATLAB. The results show that PNN proves to be a better technique in classifying the noises than the MLP and BPN models. The future work will concentrate on identifying an appropriate filter for removal of each type of noise by using neural network which will further enhance the image for processing.

Tiwari, Singh and Shukla (2011) studied statistical moments based noise classification using feed forward back propagation neural network, a neural network classification based noise identification method is presented by isolating some representative noise samples, and extracting their statistical features for noise type identification. The isolation of representative noise samples is achieved using prevalent used image filters whereas noise identification is performed using statistical moments features based classification system. The steps of the algorithm, these are seven major steps: image acquisition, preprocessing of images, noise inclusion, filtering, noise pattern extraction, feature extraction and classification. In the initial steps they introduced noises namely uniform, Gaussian, impulse and speckle to the preprocessed images. Then they filtered the noisy images using two commonly used

filters, average filter and median filter. To get the noise patterns, filtered images have been subtracted from the noisy images in case of additive noises and divided in case of multiplicative noise. Once the noise patterns are acquired, the method demands the extraction of features. So, the statistical features as the moments up to fifth order have been calculated in the next step to prepare the training and testing database. Finally, the training and testing performed quite well with this feature database using feed forward back propagation neural network. Their results of the experiments using this method show better identification of noise than those suggested in the recent works. In general the purpose of detection and classification of the noise has been achieved by using feed forward back propagation neural network. A maximum accuracy of 98 percent was found for speckle noise followed by accuracy of 96 percent, 95 percent and 90 percent for those of uniform, Gaussian and impulse noises respectively. Their work shows that it can help in choosing the appropriate filter for image de-noising.

Masood, Hussain and Jaffar (2012) studied intelligent noise detection and filtering using neuro-fuzzy system, in their research, they have proposed a neuro-fuzzy based blind image restoration technique to remove impulse noise which improves an existing novel fuzzy filter (NFF) technique. The research introduces a new noise detection technique in the existing NFF technique so that edge and texture information can be preserved by not considering the non-noisy pixels for noise removal. Proposed method consists of noise detection, histogram estimation and noise filtering processes. Noise detection process, they have used feed forward neural network to detect salt & peppers noise in gray-scale images. Proposed method consists of two steps, neural network training and noise detection. Noise detection is performed using trained neural network. Neural network lies under supervised

learning paradigm. First of all they train a neural network using training data. Generation of training data is given below in detail. After training they get a trained net, which is capable of distinguishing noisy pixels from non-noisy pixels. They have applied their technique on a large dataset of images. They have used images having large fine details as well as images having lesser fine details. As the number of hidden layers increase, the time taken by neural network to train and to generate output also increases. Therefore, in the proposed technique minimum number of hidden layers and neurons, with which neural network gives best performance are used.

Charhar and Thakare (2015) studied performance comparison of various filters for removing Gaussian and Poisson noises, the area of digital image processing related to processing of digital images by using digital computer. De-noising of image is an essential part of image reconstruction process. Noise gets introduced during acquisition, transmission, reception and storage and retrieval processes. Noise may be classified as substitutive noise (impulsive noise like salt and pepper noise, impulsive noise etc), additive noise like Gaussian noise and multiplicative noise like speckle noise. The important property of image de-noising model is that it should completely remove noise with preserving edges. Basically the image quality is measured by the peak signal to noise ratio and root mean square error. However, in their research first image is taken and some noise is added to image to make it as noisy image and then noisy image is decomposed by filters. It becomes very important to de-noise the image before applying to different applications. The principle approach of image de-noising is filtering. Filters used to remove noise are averaging filters, median filters, and wiener filter. In their study, they have implemented the above mentioned filters in MATLAB to recover the image degraded by Gaussian noise and Poisson noise.

Wiener filter performs better in removing Gaussian noise as well as Poisson noise than other filters. Median filter also provide better results for Gaussian noise and Poisson noise. In this paper PSNR and RMSE has been used as comparison parameters. Results have been simulated on MATLAB 2013.

Lal, Chandra and Upadhyay (2009) studied noise removal algorithm for images corrupted by additive Gaussian noise, their research presents noise removal algorithm for gray scale images corrupted by additive Gaussian noise. A robust open close sequence filter based on mathematical morphology for high probability additive Gaussian noise removal is discussed. Mathematical morphology is nonlinear image processing methodology that is based on the application of lattice theory to spatial structures. After that, mathematical morphology has become popular in the image processing field, due to its rigorous mathematical description and its proven applicability in a number of imaging problems, including noise elimination, feature extraction, and image compression. Two fundamental mathematical morphological operations are dilation and erosion. In fact, many of the morphological algorithms are based on these two primitive operations. In gray scale images, they develop algorithms for boundary extraction via a morphological gradient operation, and for region partitioning based on texture content. Mathematical morphological operations are also useful in smoothing and sharpening, which often are useful as per or post processing steps. Simulation and experimental results demonstrate that the robust open close sequence filter outperforms a number of other existing algorithms and is particularly effective for highly corrupted images. Their research highlighted the noise removal algorithm for gray scale images corrupted by additive Gaussian noise. In their study the performance of robust open-close sequence filter have been

evaluated and compared with the performance of other nonlinear filters and wavelet transforms. The morphological residue detector powerfully determinates the additive Gaussian noise with a low percentage error. The simulation results indicate that the robust open close filter performs better than other nonlinear filtering techniques and wavelet transforms for noise removal from gray scale images. The simulation results also indicate that the robust open close filter also provides better PSNR as compared to other non linear techniques used.

Palakkal and Prabhu (2012) studied Poisson image de-noising using fast discrete curvelet transform and wave atom, In their research, they propose a strategy to combine fast discrete curvelet transform (FDCT) and wave atom (WA) with multi-scale variance stabilizing transform (MS-VST). Their objective is to develop algorithms for Poisson noise removal from images. Applying variance stabilizing transform (VST) on a Poisson noisy image results in a nearly Gaussian is distributed image. The noise removal can be subsequently done assuming Gaussian noise model. MS-VST has been recently proposed to improve the de-noising performance of Anscombe's VST at low intensity regions of the image to facilitate the use of multi-scale multi-directional transforms like the curvelet transform for Poisson image de-noising. Since the MS-VST has been implemented in the space domain, it is not clear how it can be extended to FDCT and WA, which are incidentally implemented in the frequency domain. They propose a simple strategy to achieve this without increasing the computational complexity. They also extend our approach to handle the recently developed mirror extended versions of FDCT and WA. They have carried out simulations to validate the performance of the proposed approach. Their results

Table 2.4 Summary of related work comparison associated with the development of noise reduction model for computed radiography system (Continued)

Topics	Related Work								
	1	2	3	4	5	6	7	8	*
Algorithm for de-noising									
Speckle noise									
Wiener filter						✓			✓
Median filter				✓		✓			✓
Average filter				✓		✓			✓
Gaussian filter									✓
Unsharp filter							✓		
Neural network									✓
Fuzzy logic									✓
PSNR						✓	✓		✓
MSE									✓
Correlation									✓
RMSE						✓			

Related Work: 1 = Rampado et al. (2006); 2 = Samei et al. (2001); 3 = Santhanam and Radhika (2005); 4 = Tiwari et al. (2011); 5 = Masood et al. (2012); 6 = Charhar and Thakare (2015); 7 = Lal et al. (2009); 8 = Palakkal and Prabhu (2012); * = This research

CHAPTER 3

RESEARCH PROCEDURE

This chapter presents research and design issues of the development of a noise reduction model for a computer radiography system. The following sections in this chapter consist of research methodology, research instruments, data collection and data analysis.

3.1 Research Methodology

An approach to the development of a noise reduction model for a computer radiography system is the commissioning and routine quality control of a Computed Radiography system, the classification of the noise in the Computed Radiography system, and the algorithm for de-noising. Details of the design are explained as follows:

3.1.1 Commissioning and Routine Quality Control of CR

1) Dosimetry

The purpose is to establish the exposure factors needed to give known detector air kerma (DAK) values in subsequent tests.

The materials consist of the X-ray equipment (Toshiba KXO-50R) as shown in Figure 3.1, the dosimeter (Unfors ThinX RAD; S/N: 30001075) as shown in Figure 3.2, and the 1 mm thick copper sheet as shown in Figure 3.3.



Figure 3.1 The X-ray equipment



Figure 3.2 The dosimeter



Figure 3.3 The copper sheet

The method is as follows:

- (1) The dose meter was positioned at 1.2 m from the focus and centrally within the x-ray beam.

(2) A 1 mm thick copper sheet filter was added to the X-ray tube housing exit.

(3) The air kermas at 1.8 m of 1 μGy , 5 μGy , 10 μGy , 15 μGy , 20 μGy and 40 μGy were converted to 1.2 m using the inverse square law.

(4) The kVp was set at 70 and the mAs was varied for the air kermas at 1.2 m measured to be equal to the calculated values.

2) Calibration of CR Unit DDI

The purpose is to assess the accuracy of the detector dose indicator for the particular Imaging Plate size.



Figure 3.4 The CR reader

The materials consist of the X-ray equipment as shown in Figure 3.1, the CR reader (FCR PROFECTION) as shown in Figure 3.4, and the cassettes and Imaging Plates (Fuji; 352.0 mm x 428.0 mm, 250.5 mm x 301.5 mm and 200.0 mm x 251.0 mm as shown in Figure 3.5 (a), (b), and (c), respectively.

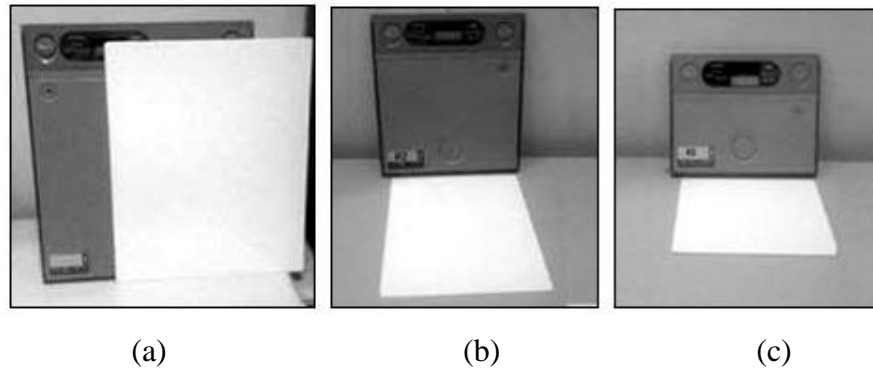


Figure 3.5 The cassettes and Imaging Plates

The method is as follows:

(1) The whole 352.0 mm x 428.0 mm Imaging Plate was exposed to a known DAK of $\sim 10 \mu\text{Gy}$ using the tube potential 80 kVp, SID (Source to Image-Detector Distance) was 180 cm and there was no filtration. The processing used a 10 minute delay, readout mode used semi-auto and $L = 1$.

(2) The detector dose indicator (DDI) was recorded and the linearised detector dose indicator value (DAK_{DDI}) was calculated using the equation, $\text{DAK}_{DDI} = (1740/S)$. This was compared to the delivered exposure.

(3) The detector dose indicator calibration test was repeated for other cassettes sizes, 250.5 mm x 301.5 mm and 200.0 mm x 251.0 mm.

3) Signal Transfer Property and DDI with Standard Factors

The purpose is to establish the relationship between the receptor dose and the pixel value.

The materials consist of the X-ray equipment as shown in Figure 3.1, the CR reader as shown in Figure 3.4, the Imaging Plates as shown in Figure 3.5(a), (b), and (c), respectively, and the copper plate as shown in Figure 3.3.

The method is as follows:

(1) The largest Imaging Plate was exposed to a known DAK of ~ 1 μGy using the standard beam condition of the Institute of Physics and Engineering in Medicine 91 (IPEM 91), 1 mm Cu filtration, SID = 180 cm, 70 kVp and 1st half value layer ~ 7.7 mm Al. The Imaging Plate was read by the CR reader using linearity, $S = 200$ and $L = 2$.

(2) This process was repeated for the air kerma values at 5 μGy , 10 μGy , 15 μGy , 20 μGy and 40 μGy .

(3) The mean pixel value from the center of the image was recorded using region of interest (ROI) analysis tools. The approximately 2 cm x 2 cm ROI was used and the actual size was recorded.

(4) The detector dose indicator calibration test was repeated for other cassettes sizes, 250.5 mm x 301.5 mm and 200.0 mm x 251.0 mm.

(5) The mean pixel value was plotted against the detector air kerma values and the equation was obtained for the trend-line graph.

(6) The regression coefficient (R^2) was obtained for the trend-line and checked to ensure that the trend-line was a good fit to the data.

4) DDI Repeatability

The purposes of this experiment are to check the short term consistency of the reader and to set a baseline for long term monitoring of system sensitivity.

The materials consist of the X-ray equipment as shown in Figure 3.1, the CR reader as shown in Figure 3.4, the largest Imaging Plate as shown in Figure 3.5 (a), and the copper sheet as shown in Figure 3.3.

The method is as follows:

(1) The Imaging Plate was exposed to known DAK using standard beam conditions of IPEM 91 then it was read by the CR reader using linearity, $S = 200$ and $L = 2$.

(2) The air kerma values were replicated at 5 μGy , 10 μGy , 15 μGy , 20 μGy and 40 μGy .

(3) The DDI was recorded and the linearised detector dose indicator value was calculated. This process was repeated three times and the coefficient of variation (CV) was calculated for the indicated exposures.

5) Matching of the CR Imaging Plates

The purpose of this experiment is to assess the variation in sensitivity between the Imaging Plates and to select a quality control cassette.

The materials consist of the X-ray equipment as shown in Figure 3.1, the CR reader as shown in Figure 3.4, the Imaging Plates as shown in Figure 3.5(a), (b), and (c), respectively, and the copper sheet as displayed in Figure 3.3.

The method is as follows:

(1) The 14" x 17" Imaging Plates in the batch were exposed to known DAK at 10 μGy using standard beam conditions and after that they were read by the CR reader using similar parameters of DDI repeatability.

(2) The process was repeated for 10" x 12" Imaging Plates in the batch and 8" x 10" Imaging Plates in the batch.

(3) The DDI was recorded and the linearised detector dose indicator values were calculated for each Imaging Plate.

(4) Each image was visually inspected for artifacts and the mean linearised DDI value was calculated for the Imaging Plates and any outliers were identified.

(5) An Imaging Plate with a DDI close to the Imaging Plates mean was identified for using in future quality control checks.

6) Differences between CR Readers

The purpose of this experiment is to assess variations in the sensitivity of the CR readers.

The materials consist of the X-ray equipment as shown in Figure 3.1, the CR reader (PROFECT) as shown in Figure 3.4, the CR reader (FCR XG5000) as shown in Figure 3.6 (a), the CR reader (FCR CAPSULA) as shown in Figure 3.6 (b), the largest Imaging Plate as shown in Figure 3.5 (a), and the copper sheet as shown in Figure 3.3.

The method is as follows:

(1) The Imaging Plate was exposed to known DAK using standard beam conditions, 1 mm Cu filtration, SID = 180 cm, 70 kVp and 1st half value layer ~7.7 mm Al. The Imaging Plate was read by the CR reader using linearity, S = 200 and L = 2.

(2) This was repeated for the air kerma values at 5 μ Gy, 10 μ Gy, 15 μ Gy, 20 μ Gy and 40 μ Gy.

(3) The results of the detector dose indicator were recorded and the DAK_{DDI} was calculated.

(4) Using the same Imaging Plate, this test was repeated for the other CR readers.

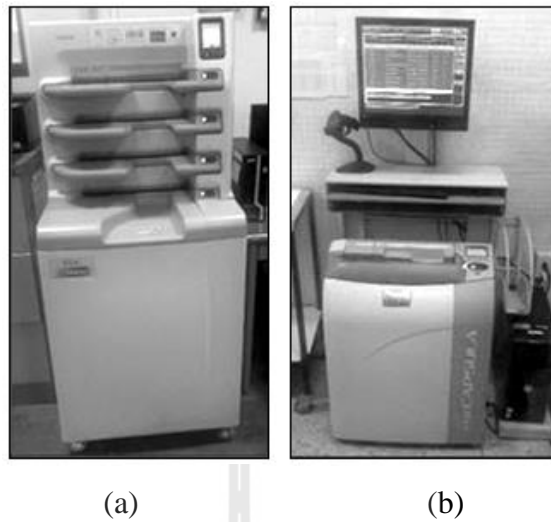


Figure 3.6 The CR readers

7) Dark Noise

The purpose of this experiment is to assess the signal level of dark noise and to test the laser power indirectly.

The materials consist of the CR reader (PROFECT) as shown in Figure 3.4 and the largest Imaging Plate as shown in Figure 3.5 (a).

The method is as follows:

- (1) An Imaging Plate was erased by the CR reader using the primary mode erasure.
- (2) The Imaging Plate was then immediately read without making an exposure using fixed mode, $S = 10000$ and $L = 1$.
- (3) The image was examined visually for uniformity using a narrow window width.
- (4) The detector dose indicator value was recorded if appropriate and the mean pixel value was recorded and its standard deviation using ROI analysis.

8) Measured Uniformity

The purpose of this experiment is to quantify the uniformity of the recorded signal from a uniformly exposed Imaging Plate.

The materials consist of the X-ray equipment as shown in Figure 3.1, the CR reader as shown in Figure 3.4, the largest Imaging Plate as shown in Figure 3.5 (a), and the copper sheet as shown in Figure 3.3.

The method is as follows:

- (1) The largest Imaging Plate was positioned at SID = 180 cm.
- (2) The Imaging Plate was exposed to a known dose of 5 μ Gy using 1 mm Cu filtration, 70 kVp and 1st half value layer \sim 7.7 mm Al.
- (3) The Imaging Plate was rotated through 180° about the vertical axis and re-exposed using the same parameters; this should largely cancel out non-uniformities due to the anode heel effect.
- (4) The Imaging Plate was read by the CR reader using linearity, S = 200 and L = 2.
- (5) The image was inspected visually for any artifacts or local non-uniformities.
- (6) Using ROI analysis tools, the mean pixel value was measured in five ROIs; one in the center of the image and one in the center of each quadrant of the image. Each ROI should include around 2 cm x 2 cm and should not include any artifacts or local non-uniformities.
- (7) The mean pixel values for each region of the image were estimated to DAK_{DDI} from the inverse signal transfer property equation.

(8) The mean for the ROIs and the maximum difference from the mean was calculated.

9) Erasure Cycle Efficiency

The purpose of this experiment is to test whether the residual signal (ghosting) remains on an Imaging Plate after readout and erasure.

The materials consist of the X-ray equipment as shown in Figure 3.1, the CR reader as shown in Figure 3.4, the largest Imaging Plate as shown in Figure 3.5 (a), and the copper sheet as shown in Figure 3.3.

The method is as follows:

(1) The attenuating material which is a 1 mm thick copper sheet was positioned in the center of an Imaging Plate and a slightly larger field was set.

(2) The Imaging Plate was exposed using 80 kVp, 20 mAs, no filtration, and SID 180 cm.

(3) The Imaging Plate was read for the regular mode.

(4) The Imaging Plate was replaced without the attenuator and center field at the same point on the Imaging Plate.

(5) The collimation was changed so the resultant field was about 10% smaller than the original field, but larger than the previously attenuated area.

(6) The Imaging was re-exposed Plate using 80 kVp, 0.5 mAs, no filtration, and SID 180 cm.

(7) The Imaging Plate was read using appropriate parameters for the system.

(8) A narrow window was set and adjusted to the appropriate level. The image was visually inspected for any evidence of the previous image; the

attenuating material and the position of the collimators were both checked. There should be no ghosting on either side of the field edges on this image. If the erasure cycle is not working properly, ghosting will be seen as a darker band outside the field and a lighter central area inside the field.

(9) ROI analysis was used to quantify the difference in pixel value between the ghost and surrounding areas and the indicated exposure was calculated for each area. The percentage of ghost to background signal was calculated using the signal transfer property to correct the pixel values.

10) Variation of Noise with Detector Air Kerma

The purpose of this experiment is to measure the noise relative to the dose.

The materials consist of the X-ray equipment as shown in Figure 3.1, the CR reader as shown in Figure 3.4, the largest Imaging Plate as shown in Figure 3.5 (a), and the copper sheet as shown in Figure 3.3.

The method is as follows:

- (1) The STP images were used for this experiment.
- (2) The variance in the image over 2 cm x 2 cm ROI in the center of the image was measured.
- (3) A quadratic curve of variance against the detector dose indicator was fitted and the noise components obtained.

11) Signal to Noise Ratio

The purpose of this experiment is to measure the relative amount of noise in an image.

The materials consist of the X-ray equipment as shown in Figure 3.1, the CR reader as shown in Figure 3.4, the largest Imaging Plate as shown in Figure 3.5 (a), and the copper sheet as shown in Figure 3.3.

The method is as follows:

- (1) A uniform image was used.
- (2) The standard deviation in the image over a 2 cm x 2 cm ROI in the center of the image was measured and this was repeated for the center of the quadrants.

12) Limiting High Contrast Spatial Resolution

The purpose of this experiment is to test the high contrast limit of the system's ability to resolve details.

The materials consist of the X-ray equipment as shown in Figure 3.1, the CR reader as shown in Figure 3.4, the Imaging Plates as shown in Figure 3.5 (a), (b), and (c), respectively, and the Hüttner test object as shown in Figure 3.7.

The method is as follows:

- (1) The Hüttner test object was placed in the center of the Imaging Plate and aligned at 45° to its edges.
- (2) The Imaging Plate was exposed using 54 kVp, 3.2 mAs, fine focus, with no added filtration.
- (3) The Imaging Plate was read by the CR reader using the appropriate parameters for that system.
- (4) The test object was placed at a slight angle to the scan and sub-scan axes and exposed same parameters.
- (5) The pixel pitch was identified for each cassette size.

(6) The images were transferred to the reporting workstation and the window level was optimized and set at a magnification of around five times. The number of resolvable groups of lines was scored and converted to the corresponding resolution.

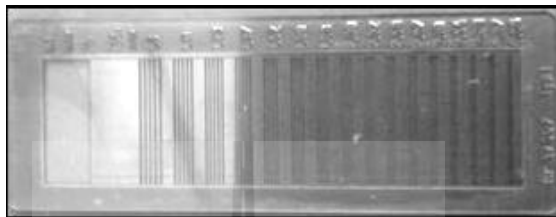


Figure 3.7 The Hüttner test object

13) Laser Beam Function

The purpose of this experiment is to assess the integrity and jitter of the laser beam scan line.

The materials consist of the X-ray equipment as shown in Figure 3.1, the CR reader as shown in Figure 3.4, the largest Imaging Plate as shown in Figure 3.5 (a), and the steel ruler as shown in Figure 3.8 (a).

The method is as follows:

- (1) The steel ruler was placed at a slight angle to the sub-scan direction on a large Imaging Plate.
- (2) The Imaging Plate was exposed at 70 kVp with no added filtration and set at 2.8 mAs to deliver an incident exposure of $\sim 20 \mu\text{Gy}$.
- (3) The Imaging Plate was read by the CR reader using the appropriate parameters for the system.

(4) The image was magnified by x10 and transferred to the reporting workstation, when necessary.

(5) A narrow window width was set so that the image was largely polarized to black or white and the edge could easily be differentiated from the background.

(6) The edge of the image was examined for evidence of laser beam jitter, as shown in Figure 3.8 (b).

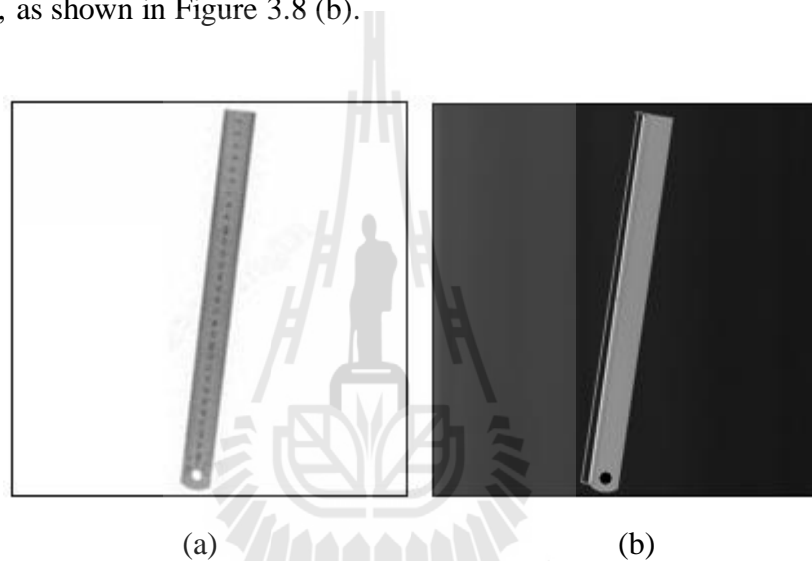


Figure 3.8 The steel ruler (a) and (b) ROI for plot profile

3.1.2 Classification of the Noise in the Computed Radiography System

1) Formation of the Original Image

The materials consist of X-ray equipment (Toshiba KXO-50R) as shown in Figure 3.1, the CR reader (FCR PROTECT) as shown in Figure 3.4, the CR detector (250.5 mm x 301.5 mm Imaging Plate) as shown in Figure 3.5, the phantom (TOR CDR) as shown in Figure 3.9, and the software for post-processing (ImageJ) as shown in Figure 3.10.



Figure 3.9 The TOR CDR phantom

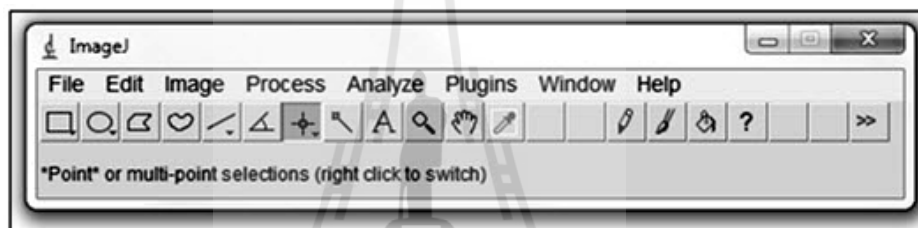


Figure 3.10 The ImageJ software

The method includes the following steps: The first step was radiography, using 54 kVp, 3.2 mAs, no filtration, and using a SID (Source to Image-receptor Distance) = 100 cm. Then a detector was used to be processed by the CR reader at this stage, with no noise reduction being processed by the vendor's software. Finally, the X-ray image was adjusted to the original image with minimal noise by retouching the software. This served as the original image, and the procedures as shown in Figure 3.11 and Figure 3.12, respectively.

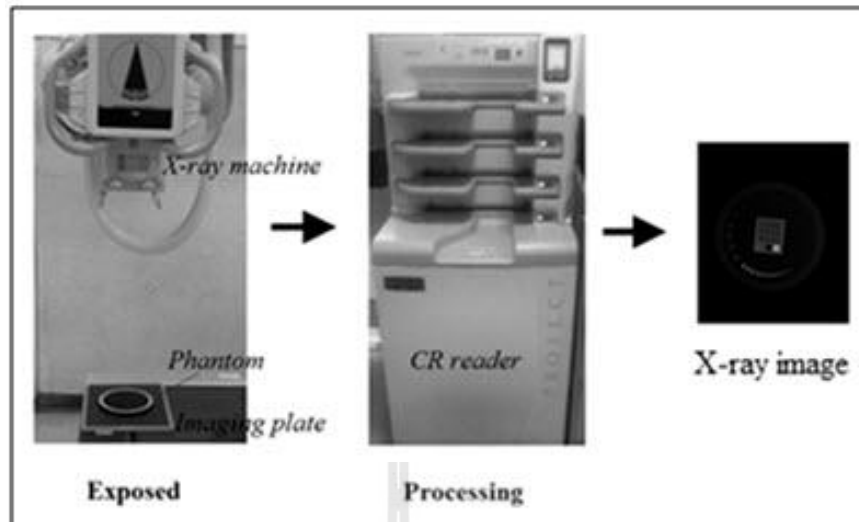


Figure 3.11 The procedure for creating the original image

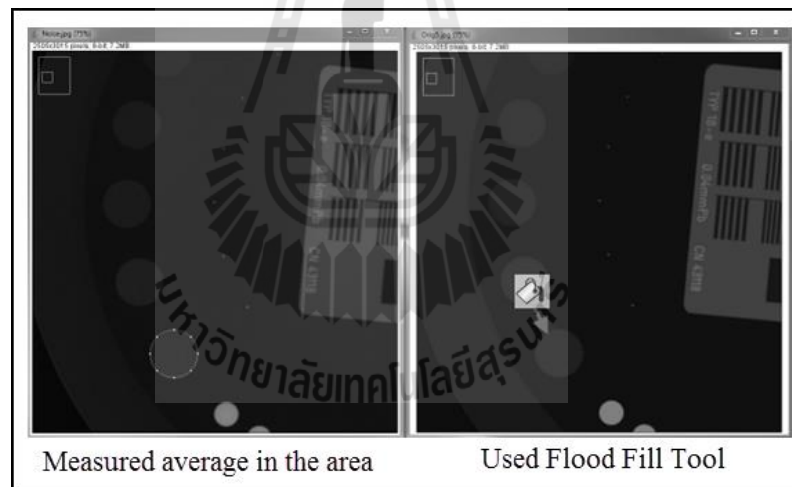


Figure 3.12 The procedure for retouching the image

2) Production of Known-Noise

Gaussian noise, Rayleigh noise, gamma noise, exponential noise, uniform noise, impulse noise, and Poisson noise were all generated for model images. They were displayed as noise images and histograms.

3) Adding the Known-Noise to the Original Image

The original image was assumed to be noiseless and the known-noise, such as Gaussian, Rayleigh, gamma, exponential, uniform, impulse, and Poisson was added. A diagram of the procedure is shown in Figure 3.13.

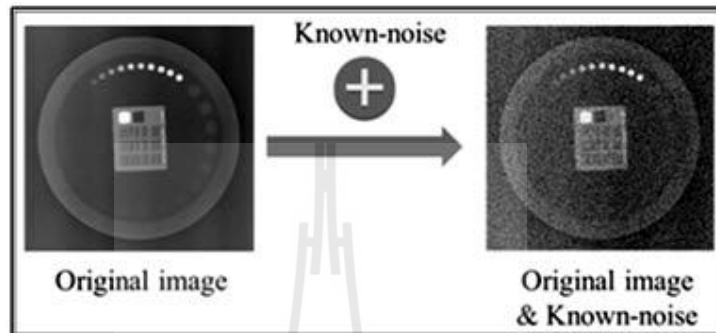


Figure 3.13 The known-noise added

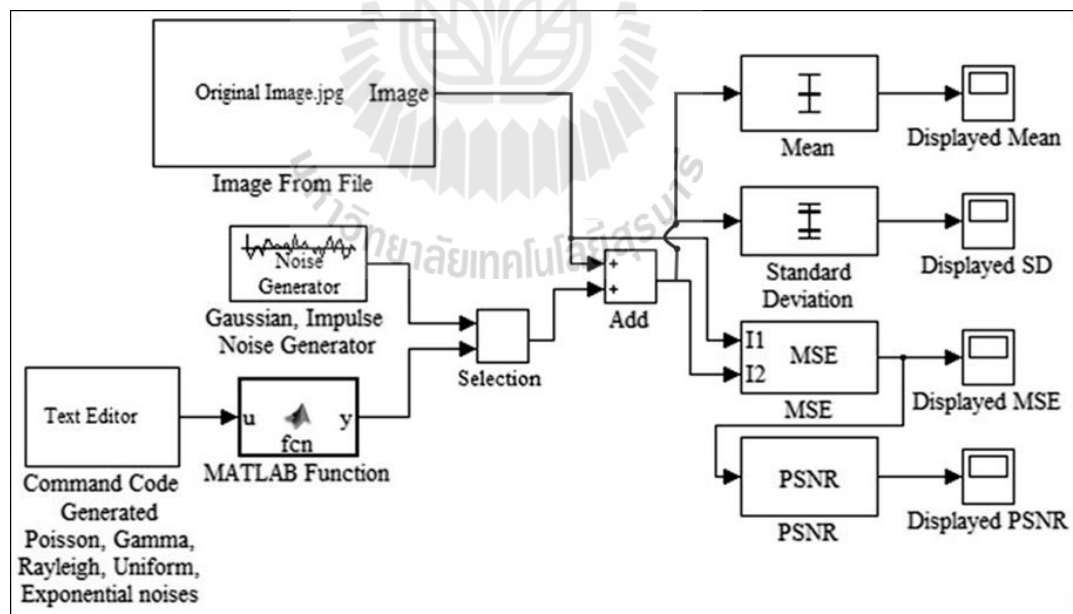


Figure 3.14 Diagram showing extraction of features

4) Feature Extraction

The known-noise, such as Gaussian, Rayleigh, gamma, exponential, uniform, impulse, and Poisson was superimposed on the original image. The Mean, MSE, PSNR, and SD were extracted from the noisy image. The diagram showing the extraction of the feature extractions is in Figure 3.14.

5) Feature Selection

The machine was trained by instances consist with 5 attributes, the Mean, SD, MSE, PSNR, and Class (Gaussian, Poisson, Impulse, Gamma, Uniform, Exponential, Rayleigh) using multilayer perceptron (MLP) algorithm, 5 hidden layers, 20,000 epochs, and a training set was used for the validation of the technique. The diagram of the algorithm for the selection of the features is shown in Figure 3.15.

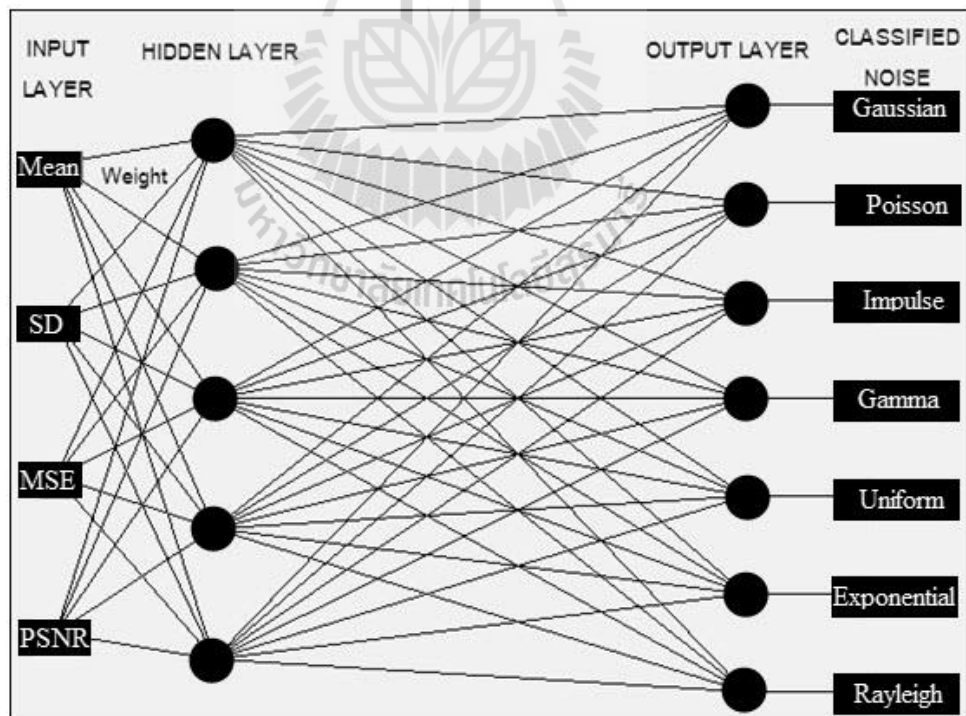


Figure 3.15 The algorithm for feature selection

The subsets of the 4 features, not including an empty set, {Mean}, {SD}, {MSE}, {PSNR}, {Mean, SD}, {Mean, MSE}, {Mean, PSNR}, {SD, MSE}, {SD, PSNR}, {MSE, PSNR}, {Mean, SD, MSE}, {Mean, SD, PSNR}, {SD, MSE, PSNR}, {Mean, MSE, PSNR}, and {Mean, SD, MSE, PSNR} were selected as being the most effective for classifying the noise. A diagram for choosing the best subset is shown in Figure 3.16.

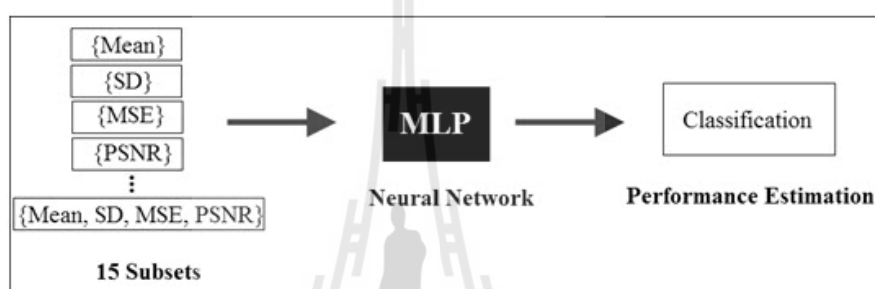


Figure 3.16 Procedure for the selection of the best subset

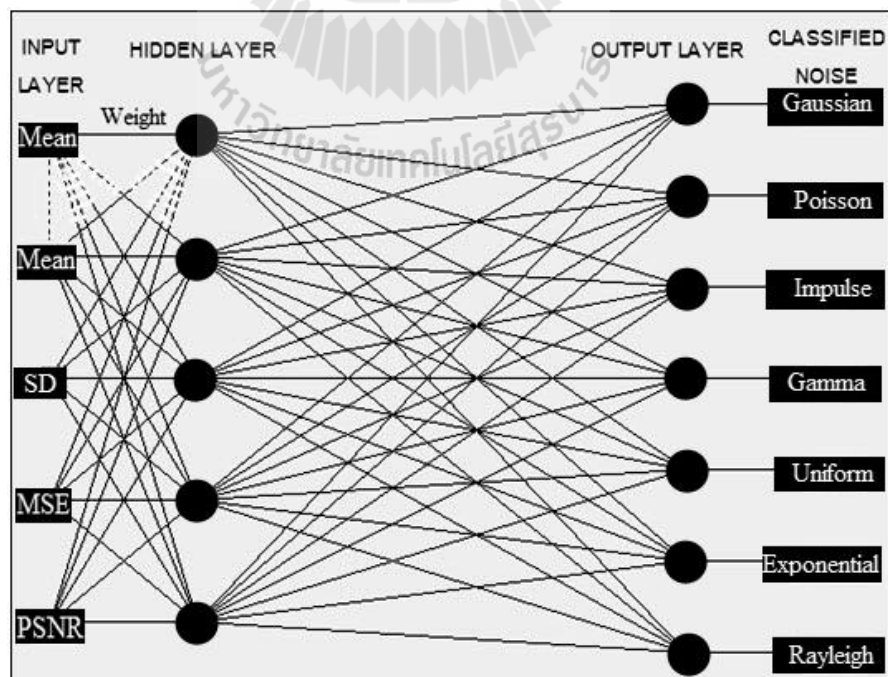


Figure 3.17 Modeling of MLP

6) Modeling

The instances were created from known-noise images. The best subset, a feature or n-features were extracted for use in the model. The models created the best model using the MLP algorithm, the training set for validation, the hidden layers were varied and the number of epochs was varied. The diagram of the MLP algorithm is shown in Figure 3.17.

7) Evaluation Model

The best model was trained and tested by the dataset, a training set was used for the validation technique using the MLP algorithm. The classification was evaluated by Precision, Recall, and F-measure. The evaluation model is shown in Table 3.1.

Table 3.1 The confusion matrix for evaluating the categorical output

	Data retrieved (+)	Data not retrieved (-)
Relevant data (+)	<i>TP</i>	<i>FP</i>
Irrelevant data (-)	<i>FN</i>	<i>TN</i>

TP = True Positive, FP = False Positive, FN = False Negative, TN = True Negative

$$\text{Precision} = \frac{TP}{(TP + FN)} \quad (3.1)$$

$$\text{Recall} = \frac{TP}{TP + FP} \quad (3.2)$$

$$\text{F - Measure} = \frac{(\beta^2 + 1)\text{Precision}}{\beta^2 \times \text{Precision} + \text{Recall}} \quad (3.3)$$

where $\beta = 1$

$$F - \text{Measure} = \frac{2\text{Precision}}{\text{Precision} + \text{Recall}} \quad (3.4)$$

8) Model Usage

The unseen data was produced by radiography. The CR image was tested by using the model for classifying noise using the rule base of MLP. The diagram of the classification is shown in Figure 3.18.

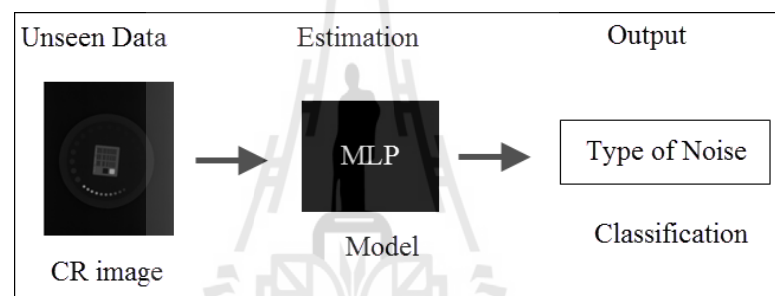


Figure 3.18 Model using for classification

The unseen data was tested by classifying the model, machine learning using MLP algorithm. The approach for testing the model, for which each node of the MLP was calculated, is shown in Figure 3.19.

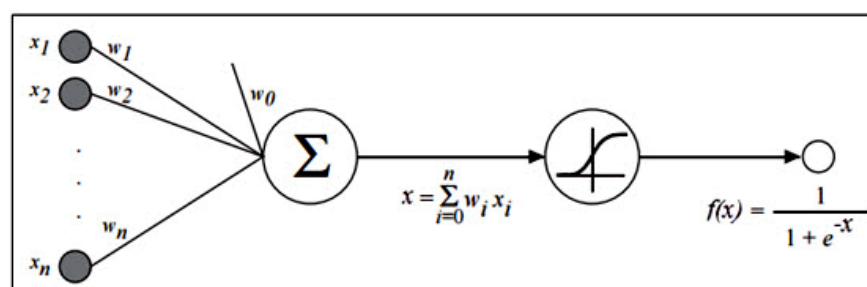


Figure 3.19 Calculation of each node

From Figure 3.19, the summation function was calculated by using the equation:

$$x = \sum_{i=0}^n x_i w_i \quad (3.5)$$

where x is the input value before the node, $x_0 = 1$, w is weight of each node. The output from the perceptron, $f(x)$ is the activation function, using the sigmoid function:

$$f(x) = \frac{1}{1 + e^{-x}}. \quad (3.6)$$

3.1.3 The Algorithm for De-noising

1) Reduced Poisson Noise

The Poisson noise was added to the original image, using the scale = 1.85×10^9 . The noisy image was converted into the de-noising image by applying different types of filters, for example, the Wiener filter (using neighborhoods of size [5 5] to estimate the local image mean and standard deviation), the Median filter, the Average filter ([3 3] kernel size), and the Gaussian filter ([5 5] kernel size, sigma = 1). The MSE, PSNR and correlation were calculated to check the performance of the filter and the de-noise images.

2) Reduced Gaussian Noise

The Gaussian noise was added to the original image, with mean = 0 and variance = 0.001. The noisy image was converted into a de-noising image by applying different types of filters, for example, the Wiener filter (using neighborhoods of size [5 5] to estimate the local image mean and standard

deviation), the Median filter, the Average filter ([3 3] kernel size), and the Gaussian filter ([5 5] kernel size, sigma = 1). The MSE, PSNR and correlation were calculated to check the performance of the filter and the de-noise images.

3) The Prototype Program

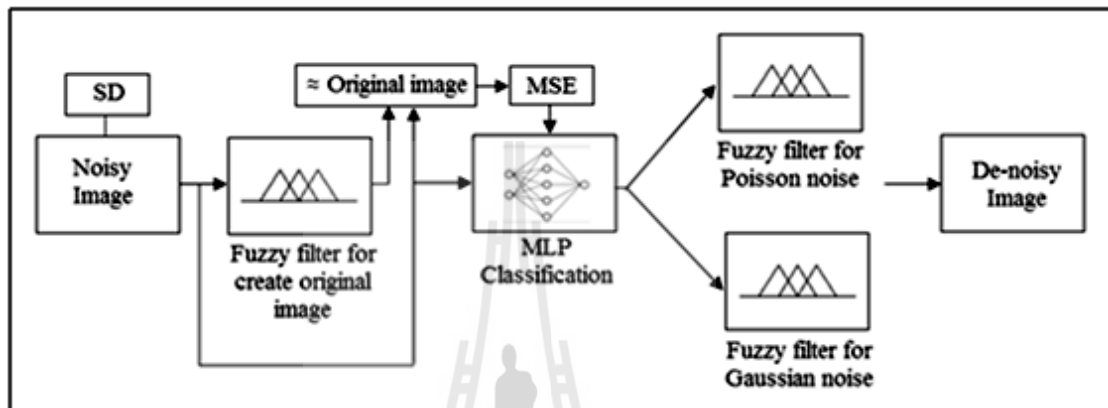


Figure 3.20 Diagram of the prototype program

Figure 3.20 shows the prototype program. Firstly, the noisy image was filtered by the fuzzy filter. Next, the noisy image was classified according to the model by using the MLP algorithm. Finally, the noisy image was de-noised by using the fuzzy filter for the Poisson or the Gaussian noise.

3.1) The Fuzzy Filter used for Creating Original Image

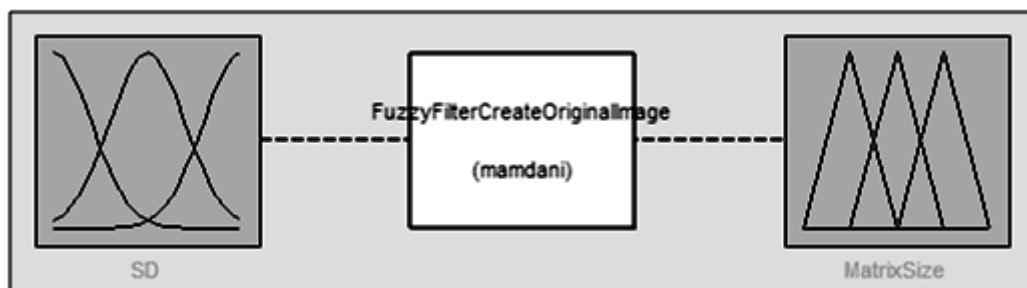


Figure 3.21 Fuzzy inference system used for creating the original image

Figure 3.21 shows the fuzzy inference system (FIS) used for creating the original image. The diagram shows the name of the input variable, SD on the left and the name of the output variable, and the matrix size on the right. The box at the center was the rule base that defines the fuzzy rules.

The steps for building a fuzzy system are as follows:

(1) The input and output linguistic variables are assigned.

- The input variable is the value of SD
- The output variable is the matrix size using the neighborhoods of the Wiener filter.

(2) The fuzzy sets are assigned.

- The value of SD is defined in linguistic terms as the input linguistic variables, which are very low, low, middle, high, and very high. The triangular function is used for the membership functions as shown in Figure 3.22.

$$\text{Very low} = \{0, 0, 12.90\}$$

$$\text{Low} = \{12.76, 12.92, 12.98\}$$

$$\text{Middle} = \{12.93, 13.01, 13.18\}$$

$$\text{High} = \{13.04, 13.28, 13.60\}$$

$$\text{Very high} = \{13.39, 26.00, 26.00\}$$

- The matrix size of using neighborhoods is defined for linguistic terms of the output linguistic variables, which are tiny, small, medium, large, and huge. The triangular function is used for the membership functions as shown in Figure 3.23.

$$\text{Tiny} = \{0, 0, 2.50\}$$

Small = {1.50, 3.00, 6.00}

Medium = {4.00, 7.00, 10.25}

Large = {8.00, 11.50, 13.50}

Huge = {11.75, 50.00, 50.00}

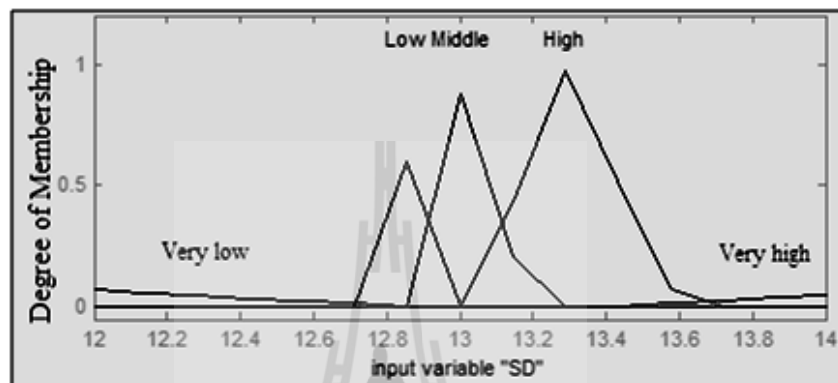


Figure 3.22 Membership functions of input variable “SD”

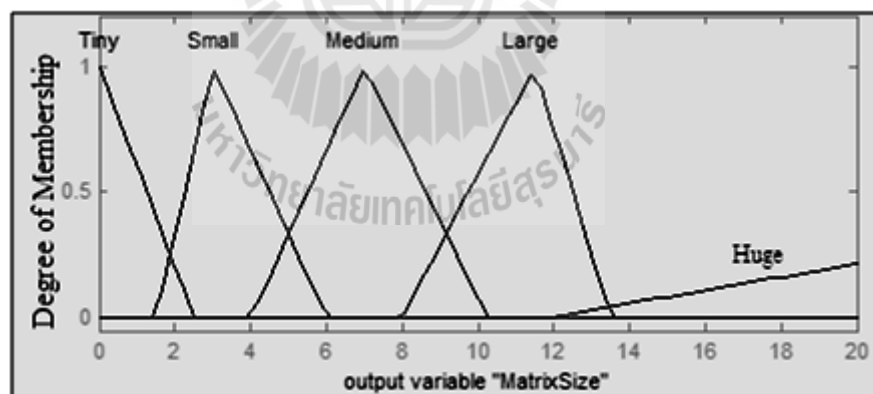


Figure 3.23 Membership functions of output variable “Matrix size”

(3) The fuzzy rules are assigned as follows:

Rule 1: “If SD is very low, then the matrix size is tiny”

Rule 2: “If SD is low, then the matrix size is small”

Rule 3: “If SD is middle, then the matrix size is medium”

Rule 4: “If SD is high, then the matrix size is large”

Rule 5: “If SD is very high, then the matrix size is huge”

(4) The rule bases are used for fuzzy inference.

(5) The crisp output is defuzzified. The technique consists of the minimum (min) which is used for implication, the maximum (max) which is used for aggregation, and the centroid of the area (COA) (Jang, Sun, and Mizutani, 1997) is used for defuzzification.

3.2) MLP Classification

The machine was trained by using instances consistent with 3 attributes, SD, MSE, and Class (Gaussian, Poisson) using the MLP algorithm, 3 hidden layers, 3,000 epochs, and the training set was used for the validation technique. The details of the instances are presented in Table 3.2.

Table 3.2 The details of instances used for modeling

Feature	Maximum	Minimum	Mean	SD
SD	13.496	12.889	13.060	0.171
MSE	8.202	0.011	2.408	2.286
Class = Gaussian (300 instances), Poisson (300 instances)				

3.3) Fuzzy Filter for Poisson Noise

The steps for building a fuzzy system are as follows:

(1) The input and output linguistic variables are assigned.

- The input variables are the values of SD and MSE.
- The output variable is the matrix size using neighborhoods for the Wiener filter.

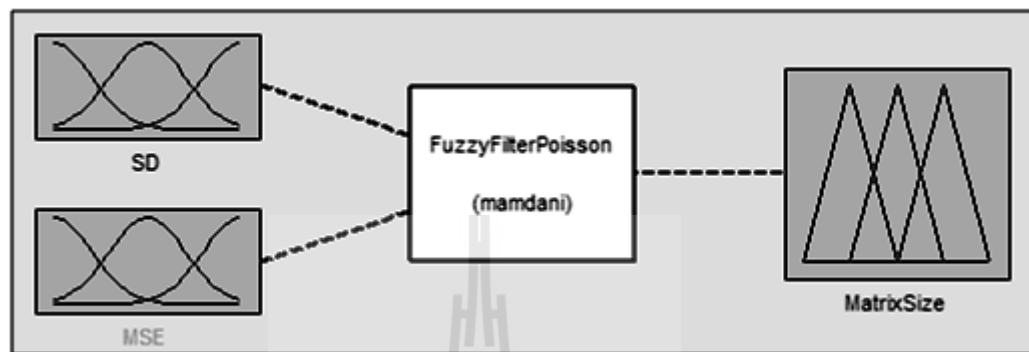


Figure 3.24 Fuzzy inference system for creating fuzzy filter of Poisson noise

Figure 3.24 shows the fuzzy inference system for creating the fuzzy filter of Poisson noise. The diagram shows the name of the input variables, SD and MSE on the left and the name of output variable, and the matrix size on the right. The box at the center is the rule base that defines the fuzzy rules.

(2) The fuzzy sets were assigned.

- The value of SD was defined in linguistic terms as the input linguistic variables: very low, low, middle, high, and very high. The triangular function was used for the membership functions as shown in Figure 3.25.

Very low = {0, 0, 12.88}

Low = {12.76, 12.90, 12.93}

Middle = {12.91, 12.94, 13.12}

High = {13.00, 13.15, 13.20}

Very high = {13.17, 26.00, 26.00}

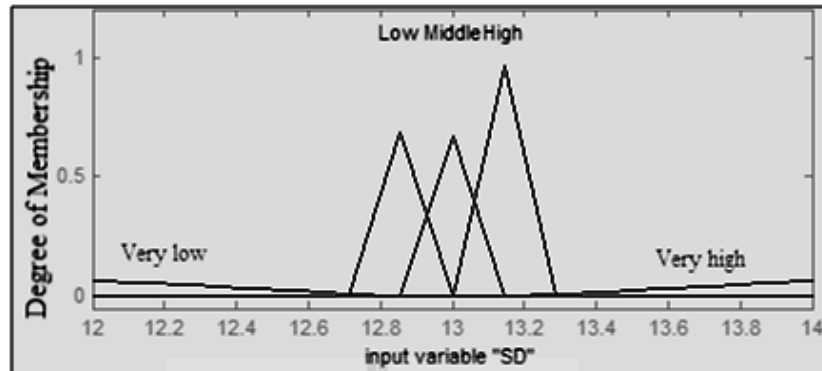


Figure 3.25 Membership functions of input variable “SD”

- The value of MSE is defined in linguistic terms as the input linguistic variables: very low, low, middle, high, and very high. The triangular function is used for the membership functions as shown in Figure 3.26.

Very low = {0, 0, 0.20}

Low = {0.11, 0.28, 0.66}

Middle = {0.37, 0.95, 1.52}

High = {1.23, 2.55, 4.60}

Very high = {3.58, 10.00, 10.00}

- The matrix size using neighborhoods is defined in linguistic terms as the output linguistic variables: tiny, small, medium, large, and huge. The triangular function is used for the membership functions as shown in Figure 3.27.

Tiny = {0, 0, 2.50}

Small = {1.50, 3.00, 6.00}

Medium = {4.00, 7.00, 10.25}

Large = {8.00, 11.50, 13.50}

Huge = {11.75, 50.00, 50.00}

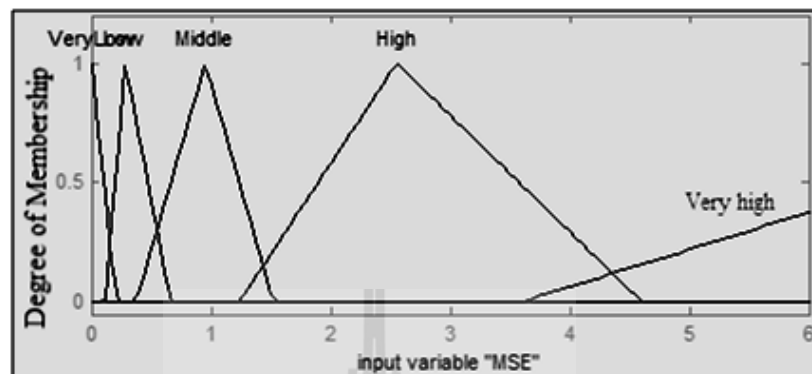


Figure 3.26 Membership functions of input variable “MSE”

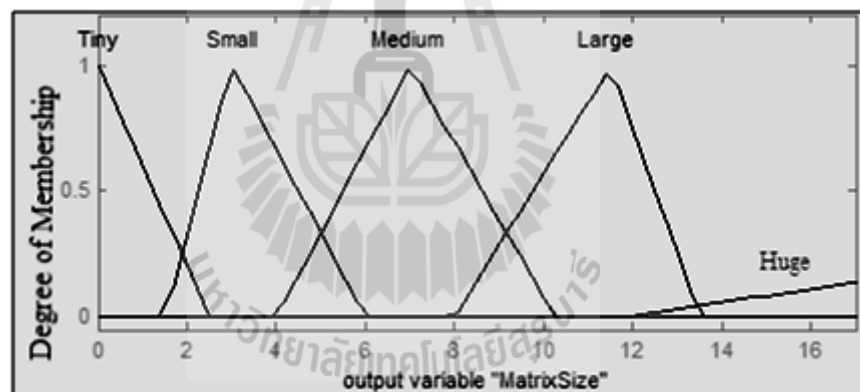


Figure 3.27 Membership functions of output variable “Matrix size”

(3) The fuzzy rules are assigned as follows:

Rule 1:

“If SD is very low or MSE is very low, then the matrix size is tiny”

Rule 2:

“If SD is low or MSE is low, then the matrix size is small”

Rule 3:

“If SD is middle or MSE is middle, then the matrix size is medium”

Rule 4:

“If SD is high or MSE is high, then the matrix size is large”

Rule 5:

“If SD is very high or MSE is very high, then the matrix size is huge”

(4) The rule bases are used for fuzzy inference.

(5) The crisp output is defuzzified. The technique consists of minimum (min) which is used for implication, the maximum (max) which is used for aggregation, and the centroid of the area which is used for defuzzification.

3.4) Fuzzy Filter for Gaussian Noise

The steps for building a fuzzy system are as follows:

(1) The input and output linguistic variables are assigned.

- The input variables are the values of SD and MSE.

- The output variable is the matrix size using the

neighborhoods for the Wiener filter.

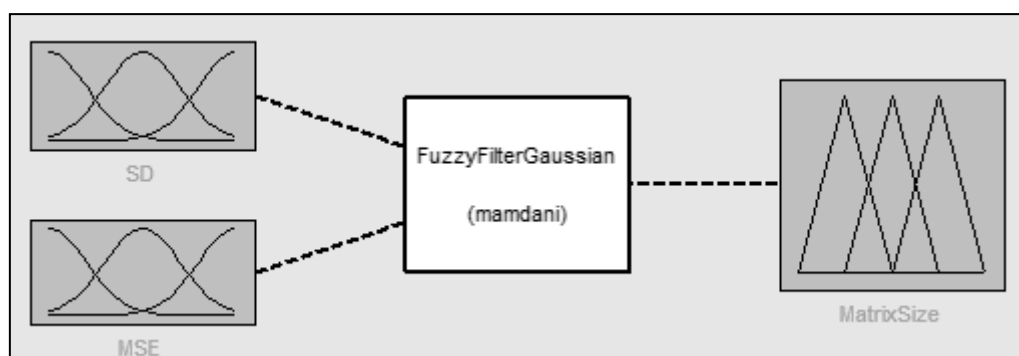


Figure 3.28 Fuzzy inference system for creating fuzzy filter of Gaussian noise

Figure 3.28 shows the fuzzy inference system for creating the fuzzy filter of Gaussian noise. The diagram shows the input variables, SD and MSE on the left and the output variable, and the matrix size on the right. The box at the center is the rule base that defines the fuzzy rules.

(2) The fuzzy sets are assigned.

- The value of SD is defined in linguistic terms of the input linguistic variables: very low, low, middle, high, and very high. The triangular function is used for the membership functions as shown in Figure 3.29.

Very low = {0, 0, 12.95}

Low = {12.92, 12.99, 13.08}

Middle = {13.02, 13.14, 13.26}

High = {13.20, 13.32, 13.44}

Very high = {13.38, 26.00, 26.00}

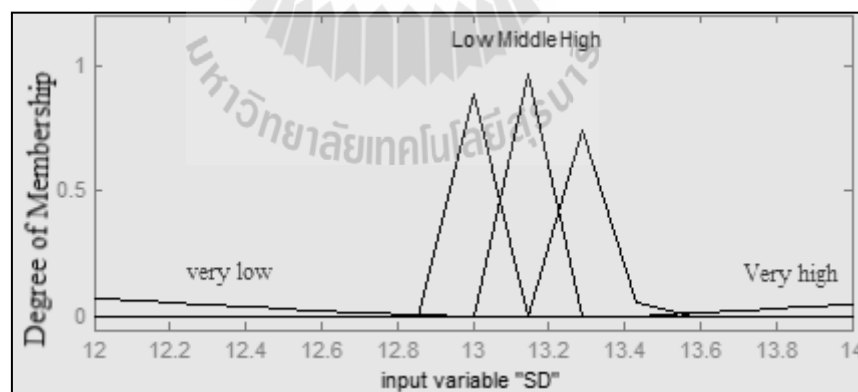


Figure 3.29 Membership functions of input variable “SD”

- The value of MSE is defined in linguistic terms of the input linguistic variables: very low, low, middle, high, and very high. The triangular function is used for the membership functions as shown in Figure 3.30.

$$\text{Very low} = \{0, 0, 0.86\}$$

$$\text{Low} = \{0.44, 1.28, 2.51\}$$

$$\text{Middle} = \{1.70, 3.32, 4.95\}$$

$$\text{High} = \{4.13, 5.76, 7.39\}$$

$$\text{Very high} = \{6.57, 10.00, 10.00\}$$

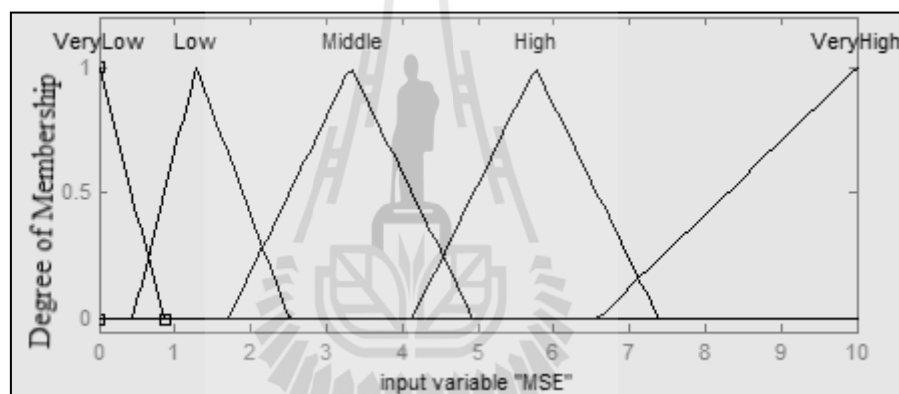


Figure 3.30 Membership functions of input variable “MSE”

- The matrix size using neighborhoods is defined in linguistic terms of the output linguistic variables: tiny, small, medium, large, and huge. The triangular function is used for the membership functions as shown in Figure 3.31.

$$\text{Tiny} = \{0, 0, 2.50\}$$

$$\text{Small} = \{1.50, 3.00, 6.00\}$$

$$\text{Medium} = \{4.00, 7.00, 10.25\}$$

Large = {8.00, 11.50, 13.50}

Huge = {11.75, 50.00, 50.00}

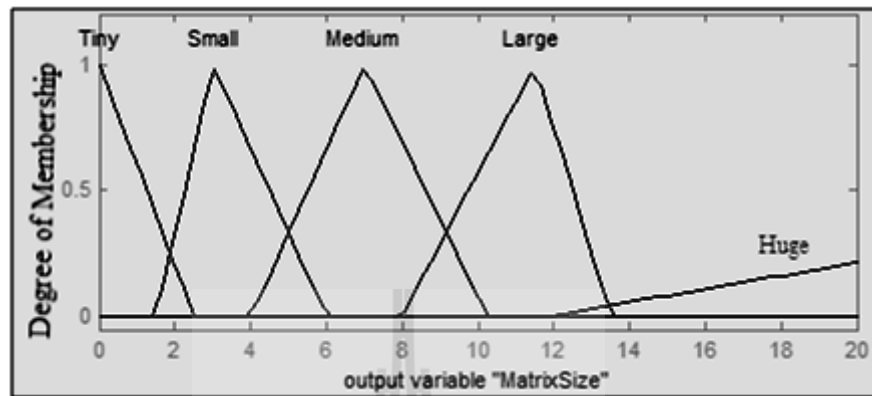


Figure 3.31 Membership functions of output variable “Matrix size”

(3) The fuzzy rules are assigned as follows:

Rule 1:

“If SD is very low or MSE is very low, then the matrix size is tiny”

Rule 2:

“If SD is low or MSE is low, then the matrix size is small”

Rule 3:

“If SD is middle or MSE is middle, then the matrix size is medium”

Rule 4:

“If SD is high or MSE is high, then the matrix size is large”

Rule 5:

“If SD is very high or MSE is very high, then the matrix size is huge”

(4) The rule bases are used for fuzzy inference.

(5) The crisp output is defuzzified. The technique consists of the minimum (min) used for implication, the maximum (max) used for aggregation, and the centroid of the area is used for defuzzification.

3.1.4 Hypothesis Testing

1) De-noising CR image Using Prototype Program

The first step is that CR image used fuzzy filter for created original image. The SD and the MSE are calculated from the CR image and the approximate original image. The second step is that the SD and MSE are used for classifying noise. The next step is that the fuzzy filter was de-noised for Poisson or Gaussian noise. Finally, the PSNR is calculated and the correlation is compared with the Vendor's software.

2) De-noised CR image Using Vendor's Software

The CR image was de-noised using the Vendor's software then the PSNR and the correlation are calculated.

3.2 Research Instruments

The research instruments or development tools are shown below.

(1) Hardware specification includes:

- Processor: Intel Core i3-550 4M 3.20 GHz
- Memory: 2048 MB
- Hard Drive: 800 GB

(2) Software specification includes:

- Operating System: Windows 7 Ultimate 32-bit
- MATLAB R2015a

- ImageJ 1.50i

- Weka 3.7.4

3.3 Data Collection

This research collects the dataset of 2,100 instances for developing a model for classifying types of noise in digital images. The instances were generated by using MATLAB commands. 300 instances of Gaussian noise were generated by varying the variances that were randomly selected from 0.0000010 to 0.0002510. 300 instances of Poisson noise were generated by varying the scales that were randomly selected from 1.00×10^7 to 2.45×10^9 . 300 instances of impulse noise were generated by varying the noise densities that were randomly selected from 0.0001 to 0.006. 300 instances of gamma noise were generated by varying the integer values for dividing the results image that were randomly selected from 60 to 1500. 300 instances of uniform noise were generated by varying the numbers in the interval (a b) that were randomly selected at intervals (0 0.054). 300 instances of exponential noise were generated by varying the numbers of parameter A that was randomly selected from 32.5 to 1000. 300 instances of Rayleigh noise were generated by varying the parameter B that was randomly selected from 0.000001 to 0.001175.

3.4 Data Analysis

The data analysis in this research comprises the correct evaluation of the performance of classification, the peak signal to noise ratio and MSE and correlation.

3.4.1 Analyzing Evaluating the Performance of Classification

Several criteria may be used to evaluate the performance of algorithms in supervised Machine Learning (ML). In general, different measures evaluate different characteristics of the classifier induced by the algorithm. Therefore, the evaluation of a classifier is a matter of on-going research (Sokolova and Lapalme, 2009), even for binary classification problems, which involve only two classes and are the most studied by the ML community.

Generally, the evaluation measures in classification problems are defined from a matrix with the numbers of examples correctly or incorrectly classified for each class, which is named the confusion matrix. The confusion matrix for a binary classification problem (which has only two classes – positive and negative) is presented in Table 3.3.

Table 3.3 Confusion matrix

	Predicted Class	
True Class	Positive	Negative
Positive	<i>TP</i>	<i>FN</i>
Negative	<i>FP</i>	<i>TN</i>

The *FP*, *FN*, *TP* and *TN* concepts may be described as:

- False positives (*FP*): examples predicted as positive, which are from the negative class.
- False negatives (*FN*): examples predicted as negative, whose true class is positive.

- True positives (*TP*): examples correctly predicted as pertaining to the positive class.

- True negatives (*TN*): examples correctly predicted as belonging to the negative class.

The evaluation measures most used in practice are as follows:

The recall measures evaluate the effectiveness of a classifier for each class in the binary problem. The recall, also known as sensitivity or true positive rate, is the proportion of examples belonging to the positive class which were correctly predicted as positive. The recall is given by the equation 3.2.

The precision is a measure which estimates the probability that a positive prediction is correct. It is given by the equation in 3.1 and may be combined with the recall originating the F-Measure. There is a constant control of the trade-off between the precision and the recall, as can be seen in equation 3.3. Generally, it is set to 1.

3.4.2 Analyzing Peak Signal to Noise Ratio and MSE

The performance parameters are the most important criteria in justifying the simulation results for noise reduction. Peak signal to noise ratio (PSNR) and mean square error (MSE) are considered to be the parameters, and the quality of the de-noised image is measured by:

$$PSNR = 10 \log_{10} \left(\frac{R^2}{MSE} \right) \quad (3.7)$$

where R is the maximum value of pixel present in an image and MSE is the mean square error between the original and the de-noised image with $M * N$ size.

$$MSE = \frac{1}{M * N} \sum_{i=1}^N [x(i, j) - y(i, j)]^2 \quad (3.8)$$

Where, $x(i, j)$ is the pixel of the original image and $y(i, j)$ is the pixel of the restored noisy image in i, j coordination. M and N are the image size.

3.4.3 Analyzing Correlation

The two-dimensional correlation criterion is used to compare the simulation results. The equation 3.9 defines the correlation (Chan and Xu, 2007).

$$Correlation = \frac{\sum_{i=1}^N \sum_{j=1}^M [x(i, j) - \bar{x}][y(i, j) - \bar{y}]}{\sqrt{\left(\sum_{i=1}^N \sum_{j=1}^M [x(i, j) - \bar{x}]^2 \right) \left(\sum_{i=1}^N \sum_{j=1}^M [y(i, j) - \bar{y}]^2 \right)}} \quad (3.9)$$

CHAPTER 4

THE RESULTS OF THE STUDY AND DISCUSSIONS

In this chapter, the results of the development of noise reduction model for computer radiography system are proposed. As previously discussed in the Chapter 3, there are commissioning and routine quality control of CR system, classification the type of noise in CR image and creating the prototype program for de-noising. Furthermore, the experimental results for checking the CR system, the most accurate classification, the appropriate algorithm for noise reduction of prototype program and all results of the study are discussed. Finally, the results of hypothesis testing are discussed.

4.1 Commissioning and Routine Quality Control of CR

4.1.1 Result of Dosimetry

Most CR testing protocols recommend using a long focus to detector distance (FDD) to minimize the anode heel effect. The same long FDD should be used throughout. The DAK should be measured reasonably scatter free conditions, correcting any dose measurements made at a shorter focus to chamber distance (FCD) using the inverse square law.

The mAs values were calculated for the air kerma of standard beam at 120 cm from the focus. The results are presented in Table 4.1.

Table 4.1 The air kerma of standard beam

Air kerma at 180 cm (μGy)	Air kerma at 120 cm (μGy)	mAs
1	2.25	1
5	11.25	4
10	22.50	8
15	33.75	10
20	45.00	14.4
40	90.00	28.4

The exposure factors needed to give known DAK (at 180 cm from focal spot) values, 1 mAs for 1 μGy , 4 mAs for 5 μGy , 8 mAs for 10 μGy , 14.4 mAs for 20 μGy , and 28.4 mAs for 40 μGy that they were used in subsequent tests.

In practice, it may be easier to work on the floor, rather than on the table, when using long FDD. If so, care should be taken to avoid back injuries when repeatedly lifting heavy Imaging Plates. Care should also be taken not to transfer any dirt from the floor to the cassette or reader. Many of these can be overcome by placing the cassette on a block of polystyrene or foam pad.

4.1.2 Result of Calibration of CR Unit DDI

The DAK_{DDI} was calculated by equation,

$$\text{DAK}_{DDI} = \left(\frac{1740}{S} \right) \quad (4.1)$$

and the percent different was calculated. The evaluations of calibration of CR unit DDI for the study are presented in Table 4.2.

Table 4.2 Calibration of CR unit DDI

IP size (cm x cm)	DAK (μGy)	S value	DAK_{DDI} (μGy)	Percent different
352.0 x 428.0	10	210	8.29	17.1
250.5 x 301.5	10	205	8.49	15.1
200.0 x 251.0	10	205	8.49	15.1

The percent different of 352.0 cm x 428.0 cm Imaging Plate is 17.1%. The percent different of 250.5 x 301.5 cm Imaging Plate is 15.1%. And the percent different of 200.0 x 251.0 cm Imaging Plate is 15.1%. The accuracy of the DDI for a particular Imaging Plate size was percent different within 20%.

During step exposure the whole Imaging Plate, mark the corners of the Imaging Plate on the table or floor with tape, so that the Imaging Plate can be easily repositioned without the use of the light beam. Marking positions for all Imaging Plate sizes at this point can save time.

The latent image signal from the Imaging Plate will drop rapidly after exposure; this is common to all CR systems. Between 1 and 10 min post-exposure, the signal typically drops by 5 to 10% (CEP, 2006a), although some systems may show less latent image decay (CEP, 2006b). Therefore, the time delay between exposures should match that specified by the manufacturer.

Cassettes usually indicate which is the tube side and which way round to insert the cassette into the reader. Care should be taken as the unloading mechanism in some readers may damage Imaging Plate by scratching them if they are inserted in the wrong orientation.

4.1.3 Result of STP and DDI with Standard Factors

The mean and SD of pixel value of image of each Imaging Plate were presented in Table 4.3.

Table 4.3 STP and DDI with standard factors

DAK (μGy)	14" x 17"		10" x 12"		8" x 10"	
	Pixel value		Pixel value		Pixel value	
	Mean	SD	Mean	SD	Mean	SD
1	256	64	256	64	256	64
5	477	7.64	480	8.34	486	7.90
10	645	2.79	652	3.14	640	2.60
15	722	2.22	731	2.76	724	2.41
20	778	1.61	789	1.84	780	1.56
40	895	0.93	896	1.04	893	1.23

The graph of STP function was plotted from mean pixel value against DAK for 14" x 17" Imaging Plate. The relation of STP function between mean pixel value and DAK is logarithm response as shown in Figure 4.1.

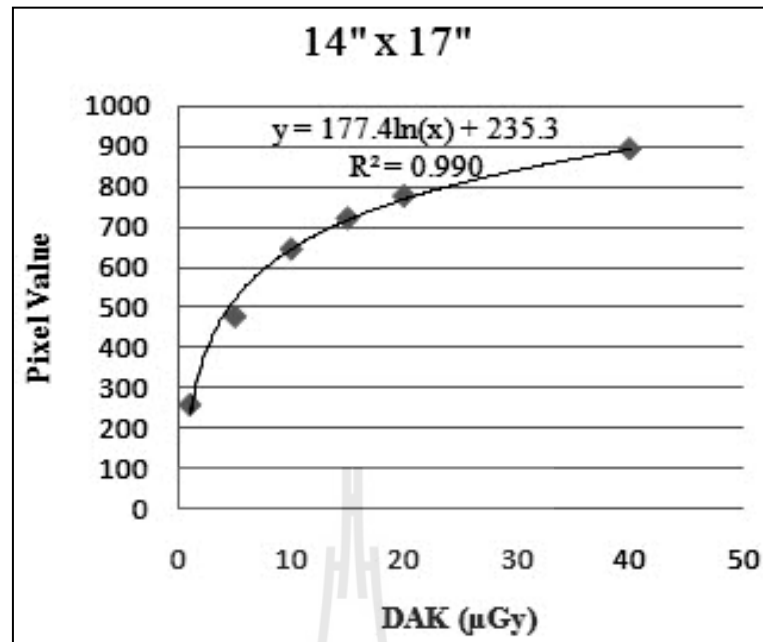


Figure 4.1 Graph of STP function of 14'' x 17''

Figure 4.1 that the STP function was applied for calculating the DAK from pixel value then it was used for the next experiment. The STP function of 14'' x 17'' Imaging Plate is

$$\text{Pixel Value} = 177.4\ln(\text{DAK}) + 235.3 \quad (4.2)$$

and the regression coefficient (R^2) = 0.990 that the trend-line is good fit to the data.

The graph of STP function was plotted from mean pixel value against DAK for 10'' x 12'' Imaging Plate. The relation of STP function between mean pixel value and DAK is logarithm response as shown in Figure 4.2.

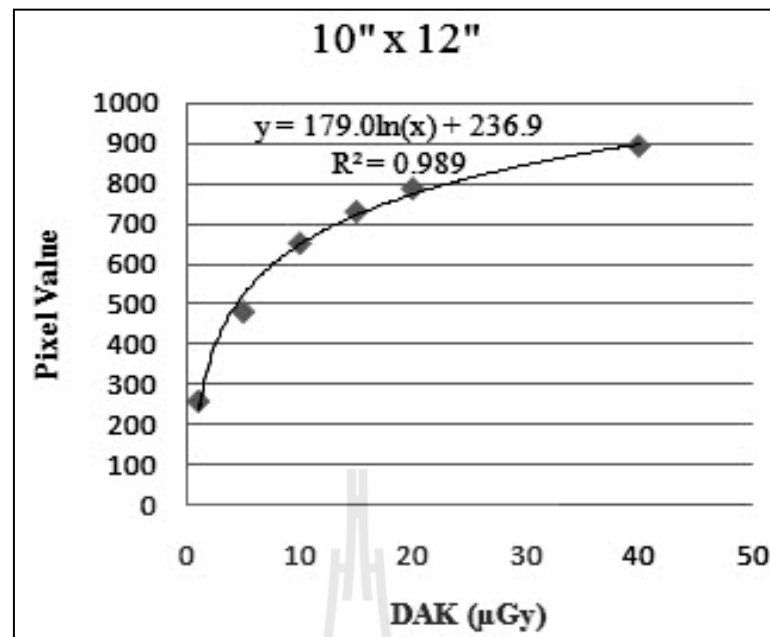


Figure 4.2 Graph of STP function of 10'' x 12''

Figure 4.2 that the STP function was applied for calculating the DAK from pixel value then it was used for the next experiment. The STP function of 10'' x 12'' Imaging Plate is

$$\text{Pixel Value} = 179 \ln(\text{DAK}) + 236.9 \quad (4.3)$$

and the regression coefficient (R^2) = 0.989 that the trend-line is not very good fit to the data.

The graph of STP function was plotted from mean pixel value against DAK for 8'' x 10'' Imaging Plate. The relation of STP function between mean pixel value and DAK is logarithm response as shown in Figure 4.3.

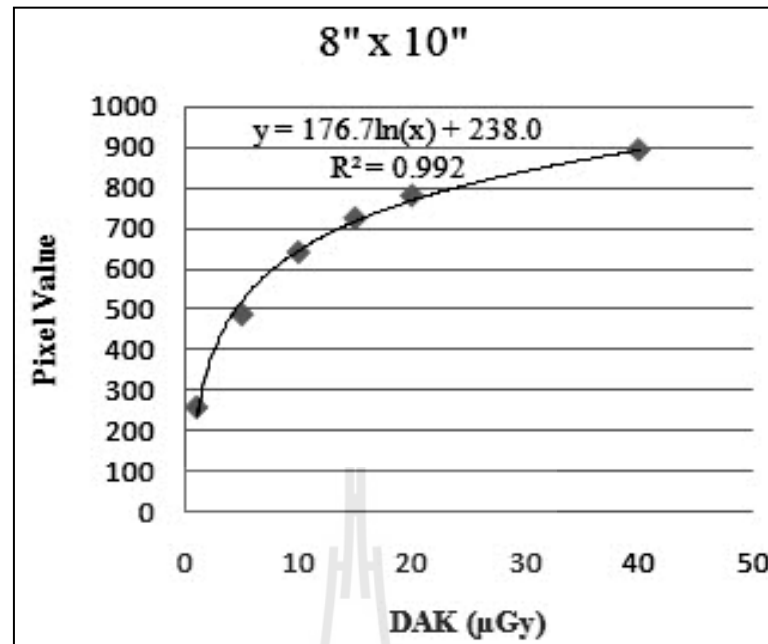


Figure 4.3 Graph of STP function of 8'' x 10''

Figure 4.3 that the STP function was applied for calculating the DAK from pixel value then it was used for the next experiment. The STP function of 8'' x 10'' Imaging Plate is

$$\text{Pixel Value} = 176.7\ln(\text{DAK}) + 238.0 \quad (4.4)$$

and the regression coefficient (R^2) = 0.992 that the trend-line is good fit to the data.

These images can also be used to determine the actual relationship between DDI and DAK where the standard conditions used differ from those recommended by the manufacturer. KCARE provide details for the standard conditions used in evaluations (CEP, 2006a): for Fuji

$$PV = 138\ln(\text{DAK}) + 152. \quad (4.5)$$

4.1.4 Result of DDI Repeatability

The pixel value of image, exposed to known DAK, was converted to DAK_{DDI} by equation 4.2. The evaluations of DDI repeatability for studied CR system are presented in Table 4.4.

Table 4.4 DDI repeatability

DAK (μGy)	Time 1		Time 2		Time 3		Time 4		CV of DAK_{DDI}
	Pixel value	DAK_{DDI}	Pixel value	DAK_{DDI}	Pixel value	DAK_{DDI}	Pixel value	DAK_{DDI}	
1	256	1.12	256	1.12	256	1.12	256	1.12	0
5	477	3.91	479	3.95	487	4.13	483	4.04	0.03
10	645	10.07	668	11.46	648	10.24	653	10.53	0.06
15	722	15.54	716	15.02	713	14.77	720	15.37	0.02
20	778	21.31	771	20.49	773	20.72	767	20.03	0.03
40	895	41.21	881	38.08	896	41.44	886	39.17	0.04

The CV values of DDI are less than 10% that they are acceptable for DDI repeatability.

Some centers set a large field size and position a reference ion chamber in one corner of the field, avoiding the Imaging Plate. This is used to check exposure consistency during this test. If the X-ray tube is fitted with a DAP meter, this can be used instead. Alternatively, if output is known to be very consistent, no monitor chamber is needed.

4.1.5 Result of Matching of CR Imaging Plates

The assessments of matching of CR Imaging Plates for studied CR system are presented in Table 4.5.

Table 4.5 Matching of CR Imaging Plates

IP size	DDI of IP 1 (μGy)	DDI of IP 2 (μGy)	DDI of IP 3 (μGy)	DDI of IP 4 (μGy)	Mean (μGy)
14" x 17"	10.07	10.11	10.08	10.03	10.07
10" x 12"	10.58	10.46	10.49	-	10.51
8" x 10"	9.89	10.12	9.91	-	9.97

The mean of DDI for 14" x 17" Imaging Plates in the batch was 10.07 μGy the IP 1 was chosen for future QC check. The mean of DDI for 10" x 12" Imaging Plates in the batch was 10.51 μGy the IP 3 was chosen for future QC perform. And the mean of DDI for 8" x 10" Imaging Plates in the batch was 9.97 μGy the IP 3 was chosen for future QC perform.

Each batch of Imaging Plates should be checked to ensure that the sensitivities of all Imaging Plates are matched. This is particularly important when Imaging Plates are added to an existing batch. Refer to manufacturer's recommendations on inter-Imaging Plate variations in sensitivity. Some CR readers correct for variations in light output between Imaging Plates. Either an Imaging Plate sensitivity value is set in the chip that identifies the Imaging Plates or this value is held in the CR reader. It is sensible to keep a departmental inventory of Imaging Plates with type, ID or serial number, age and usage. Record the Imaging Plate cassette combination if possible.

The visual inspection of the images should be undertaken using a narrow window width; possible causes of artifacts include dust, cracks and scratches on the Imaging Plates. The natural variation in sensitivity across an Imaging Plate should not be mistaken for an artifact.

4.1.6 Result of Differences between CR readers

The DAK_{DDI} was calculated by pixel value of images from three CR readers. The evaluations of differences between CR readers, FCR PROTECT, FCR XG5000 and FCR CAPSULA for studied CR system are presented in Table 4.6.

Table 4.6 Differences between CR readers

DAK (μ Gy)	FCR PROTECT		FCR XG5000		FCR CAPSULA		CV of DAK_{DDI}
	Pixel value	DAK_{DDI}	Pixel value	DAK_{DDI}	Pixel value	DAK_{DDI}	
1	256	1.12	256	1.12	256	1.12	0
5	477	3.91	482	4.02	490	4.20	0.04
10	645	10.07	657	10.77	660	10.96	0.04
15	722	15.54	729	16.17	732	16.44	0.03
20	778	21.31	788	22.55	792	23.06	0.04
40	895	41.21	901	42.63	903	43.11	0.02

The CV values of DDI, differences 3 CR readers are less than 20% that they are acceptable for DDI of differences between CR readers.

Nominally, similar readers may have different sensitivities and there may be wide tolerances on the set-up of each reader. Even where two or more readers each have a DDI calibration that is within tolerance, there may be a relatively large

variation between these readers (up to twice the tolerance on calibration). Where Imaging Plates are likely to be read in more than one reader, it is good practice to set readers up to be as similar as possible.

Compare the DAK_{DDI} for each reader with others in the department. This test is only useful where Imaging Plates are likely to be read in more than one reader.

4.1.7 Result of Dark Noise

The evaluations of dark noise for studied CR system are presented in Table 4.7.

Table 4.7 Dark noise

IP size (cm x cm)	Mean of pixel value	SD of pixel value	DAK_{DDI}
352.0 x 428.0	16	0.19	0.28
250.5 x 301.5	16	0.15	0.28
200.0 x 251.0	8	0.24	0.28

The results found dark noise values below the specified tolerance for the Fuji CR reader, the specified tolerance, pixel value < 280.

Dark noise describes the signal level of electronic noise inherent in the system. For CR, this is the level of noise seen when reading an unexposed Imaging Plate. High signal in the dark noise image may be indicative of falling laser power; increasing amplifier gain to compensate for this will result in greater amplification of dark noise.

CR readers have a manual erasure cycle for removing low levels of signal from background and scattered radiation; some readers will also have a separate erasure cycle for clearing overexposed Imaging Plates. Readers usually

revert back to normal reading mode at the end of the manual erasure cycle. Care is required with some readers because, if they have not switched back to normal reading mode before the next Imaging Plate is inserted, that Imaging Plate will also be erased leading to the potential loss of patient data.

The dark image should usually be uniform and artifact free. Some systems add a collector profile to the image to compensate for non-uniform collection efficiency across the Imaging Plate; this gives a series of bands across a dark noise image. This banding may be observed in the sub-scan direction on dark noise images but is not apparent on clinical images.

4.1.8 Result of Measured Uniformity

The assessments of measured uniformity for studied CR system are presented in Table 4.8. The DAK_{DDI} was calculated from inverse STP equation:

$$DDI = e^{\frac{PixelValue-235.3}{177.4}} \quad (4.6)$$

Table 4.8 Measured uniformity

	Mean of pixel value	SD of pixel value	Maximum difference from mean	DAK_{DDI}
Center of image	480	2.96	3	3.97
Center of quadrant I	486	3.55	3	4.11
Center of quadrant II	479	3.01	4	3.95
Center of quadrant III	478	2.97	5	3.93
Center of quadrant IV	492	3.38	9	4.25

The mean for the ROIs was 483 and the maximum difference from the mean was 9, the center of quadrant IV. The DAK_{DDI} , the mean for the ROIs was 4.042 μGy and the maximum difference from the mean was 5.15% of the center of quadrant IV. The results found measured uniformity values below the specified tolerance for the IPEM Guidance, the specified tolerance, STP corrected ROI values within mean $\pm 10\%$.

4.1.9 Result of Erasure Cycle Efficiency

The assessment of erasure cycle efficiency for studied CR system is presented in Figure 4.4, upon initially visual examination there was no evidence of any “ghosting” on the second image.

All systems have automatic erasure cycles after reading an Imaging Plate. This erasure cycle should remove any residual signal from the Imaging Plate, leaving it clear for the next exposure (Rowlands, 2002). The light source used for erasure fades over time and must eventually be replaced. This may become less of a problem in the future as longer lasting diodes replace halogen bulbs in new CR readers.

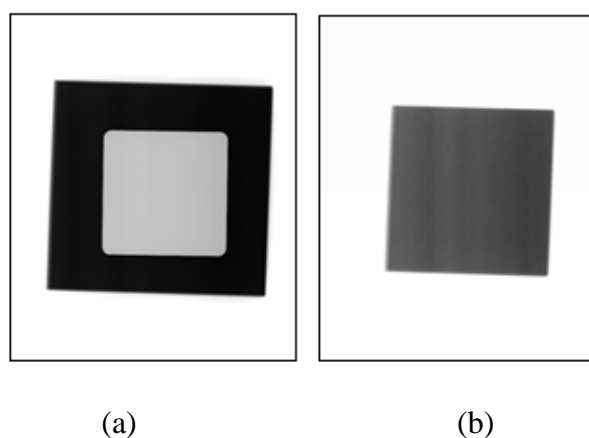


Figure 4.4 The first image, (a) and (b), the second image

4.1.10 Result of Variation of Noise with Detector Air Kerma

Table 4.9 Variation of noise with detector air kerma

DAK (μGy)	Mean of pixel value	SD of pixel value	Variance
1	256	64	4096.00
5	477	7.64	58.37
10	645	2.79	7.78
15	722	2.22	4.93
20	778	1.61	2.59
40	895	0.93	0.86

The assessments of variation of noise with DAK for studied CR system are presented in Table 4.9. The relation between variance and DAK was plotted for curve as shown in Figure 4.5.

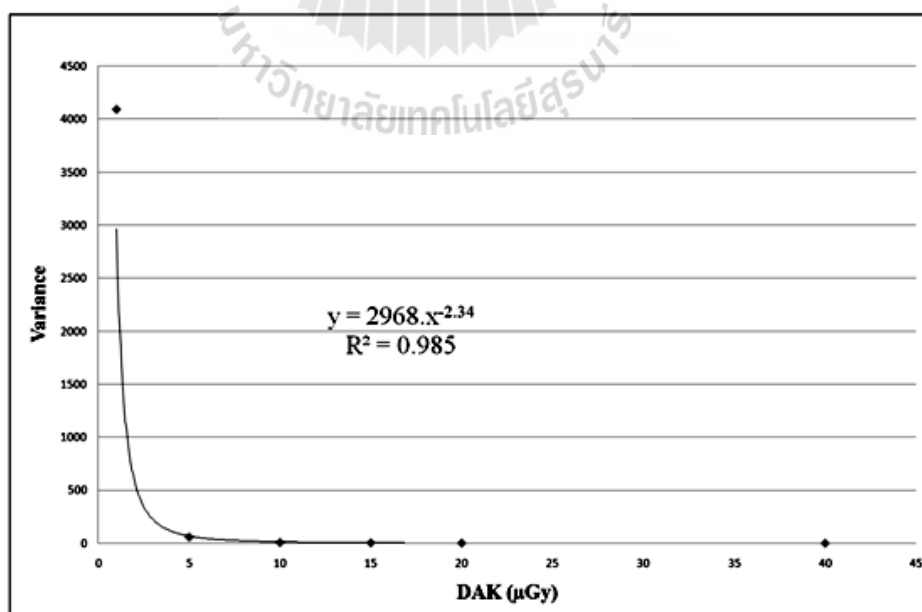


Figure 4.5 Variation of noise with detector air kerma

Figure 4.5, the function for fitting the variance to the corresponding DAK of this study is power response, equation:

$$\text{Variance} = 2968 \times \text{DAK}^{-2.34}, \quad (4.6)$$

and $R^2 = 0.985$ that the trend-line is not very good fit to the data.

The measure of variance is useful indicator of noise in image. The noise performance of detector can be checked by plotting the variance of pixel value as a function of DAK.

Most detectors have a DAK range over which image noise follows a Poisson distribution before other noise sources become important. If the detector is quantum limited, the variance should follow a Poisson distribution. This can be confirmed by fitting the variance to the corresponding DAK (equation 4.7); the b coefficient should be 1.0 for Poisson image noise.

$$v = aK^b \quad (4.7)$$

Where $K = \text{DAK}$; $v = \text{variance}$, a and b are constants.

At low DAK values (additive) electronic noise can increase the variance, while at high DAK, structure noise can be an important component of total system noise. Although these noise sources are common to most current detector (Evans, Workman and Payne, 2002; Mackenzie and Honey, 2007), the type and magnitude of noise depend on the specific detector in question. These factors influence the shape of graph (variance Vs DAK), the value of the b coefficient and the DAK range over which the detector is quantum noise limited. For this test, very low or high DAK values should not be used because at these doses, the system is unlikely to be quantum limited.

The size and position of the ROI will influence the measured variance, however using a nominal ROI placed at the image center is sufficient for a QC measurement. Flynn and Samei (1999) recommended an ROI size of 2 cm x 2 cm, as a compromise between small ROI which may be affected by local non-uniformities and large ROIs which may be affected by the anode heel effect. The ROI location should avoid artifacts in the image.

Ideally, these images should be inverted via the STP before making this measurement (Mackenzie, 2008). Linear system theory states that to make meaningful calculations, the system should follow the rules of additivity and homogeneity. A system with a STP of a logarithmic or a power law relationship will not meet these criteria. The image data can be linearised by applying the inverse of the STP to the value of each pixel. For departments without access to software to linearise an image pixel-by-pixel, then Mackenzie (2008) provides an alternative correction method for correcting noise measurement, which gives acceptable results.

This test recommended to be undertaken at commissioning; subsequently, it can be used to give more information on changes in the noise sources. It should be noted that the variance has not been normalized, therefore if there is a change in the amplification of the system then the variance should change with the amplification.

4.1.11 Result of Signal to Noise Ratio

The evaluations of signal to noise ratio for studied CR system were presented in Table 4.10.

Signal to noise ratio is a useful concept for measuring the response of a digital detector quantitatively with simple tools. It may give information on system

sensitivity and noise properties. SNR is defined as the ratio of the STP corrected signal (pixel value) to the STP corrected noise (standard deviation of pixel value).

Table 4.10 Values of mean pixel value, SD and SNR for the evaluating signal to noise ratio

	Mean pixel value	SD	SNR
Center of image	480	2.96	162.16
Center of quadrant I	486	3.55	136.90
Center of quadrant II	479	3.01	159.14
Center of quadrant III	478	2.97	160.94
Center of quadrant IV	492	3.38	145.56

Care is required in SNR measurement, as SNR is strongly affected by processing. Any changes in processing may affect the results so consistency in selection of processing parameters is important. It is possible to apply processing algorithms in such a way that the SNR changes greatly, but the visibility of low contrast details is unchanged (Burgess, 1999).

Although it is reasonable to compare SNR against a baseline for a single system, differences in processing mean that it is unwise to use SNR to compare different types of system.

4.1.12 Results of Limiting High Contrast Spatial Resolution

The assessments of limiting high contrast spatial resolution for studied CR system were presented in Table 4.11.

The limiting high contrast spatial resolution of 352.0 x 428.0 Imaging Plate was 2.87 for scan and sub-scan direction that they were not acceptable level for the IPEM Guidance, acceptable level values $\geq 0.70/2 \Delta p$ (3.5 for this study).

The limiting high contrast spatial resolution of 250.5 x 301.5 Imaging Plate was 3.54 for scan and sub-scan direction that they were acceptable level for the IPEM Guidance, acceptable level values $\geq 0.70/2 \Delta p$ (3.5 for this study).

The limiting high contrast spatial resolution of 200.0 x 251.0 Imaging Plate was 3.93 for scan and sub-scan direction that they were acceptable level for the IPEM Guidance, acceptable level values $\geq 0.70/2 \Delta p$ (3.5 for this study).

Table 4.11 Limiting high contrast spatial resolution

IP size (cm x cm)	Align	Pixel pitch (μm)	Line pair (mm^{-1})
352.0 x 428.0	45°	100	2.87
	~0°	100	2.87
	~90°	100	2.87
250.5 x 301.5	45°	100	3.54
	~0°	100	3.54
	~90°	100	3.54
200.0 x 251.0	45°	100	3.93
	~0°	100	3.39
	~90°	100	3.93

Spatial resolution in CR is determined mainly by pixel pitch, as determined by the sampling rate of the photomultiplier tube output (scan direction).

CR readers for general radiography typically use sampling frequencies of 5 to 12 pixels per mm, giving pixel pitches of 200 to 80 μm and leading to theoretical limiting resolutions of 2.5 to 6 line pairs (lp) mm^{-1} . The pixel pitch may be selectable by the user or may be linked to the Imaging Plate size. Some systems have a smaller pixel pitch of around 40 μm for use in mammography and extremity imaging. The pixel pitch can be found in the DICOM header of the image. The limiting resolution should approach the Nyquist limit. For smaller pixel pitches, the resolution is often below the Nyquist frequency indicating that other blurring processes are limiting the spatial resolution. Spatial resolution may also be limited by the display on review workstations, particularly if no or limited zoom facilities are available.

Spatial resolution also depends on the size of the laser beam used to read out the Imaging Plate and on the optical characteristics of that Imaging Plate. Optical scatter in the phosphor causes the effective size of the laser beam to increase with depth. Light emitted deeper in the phosphor will also scatter more before reaching the collection system. Therefore, a latent image stored near the surface will give better resolution on readout than one stored deeper in the phosphor (Fetterly and Hangiandreou, 2001). As lower energy photons deposit their energy closer to the surface of the Imaging Plate, limiting spatial resolution should be assessed with a low energy X-ray beam.

A lead resolution grating can be used to quickly assess high contrast spatial resolution. It should contain sufficiently fine gratings for the highest sampling rate for the Imaging Plates. A Hüttner 43 test object (or equivalent) with line spacings up to 10 lp mm^{-1} may be required.

Spatial frequencies above the Nyquist limit appear as lower frequency components of the image. This aliasing appears as light and dark bands superimposed at various angles across the different grating groups. Only unaliased groups should be counted (Albert et al., 2002).

The limiting resolution should be compared to the Nyquist limit, defined at 45° by $\sqrt{2}/2\Delta p$ where Δp is the pixel pitch. It should also be compared to that measured at commissioning and/or any results measured on a similar system known to be in good adjustment. Spatial resolution is generally poorer in the scan direction. The image should be examined carefully, normally as the bar pattern frequency approaches the Nyquist frequency then aliasing appears and makes the limiting resolution criteria more difficult. Albert et al. (2002) showed that blurring artifacts appear in bands angled to the bar pattern; below the Nyquist frequency, the blurring will be in the same direction, and when the bar frequency is greater than the Nyquist frequency, the blurring bands will flip by 90° . Honey and Mackenzie (2009) also showed a system where no aliasing appeared and the measured resolution was below the expected value; this was shown to be due to an incorrectly set low frequency filter.

4.1.13 Result of Laser Beam Function

The result of laser beam function for studied CR system, a linear fit was calculated for the series of edge position value, thus obtaining position of an ideal edge with no jitter as shown in Figure 4.6.

The readout laser beam should scan smoothly across the Imaging Plate. Any jitter in its motion will cause artifacts. Likewise, the Imaging Plate should move smoothly through the reader.

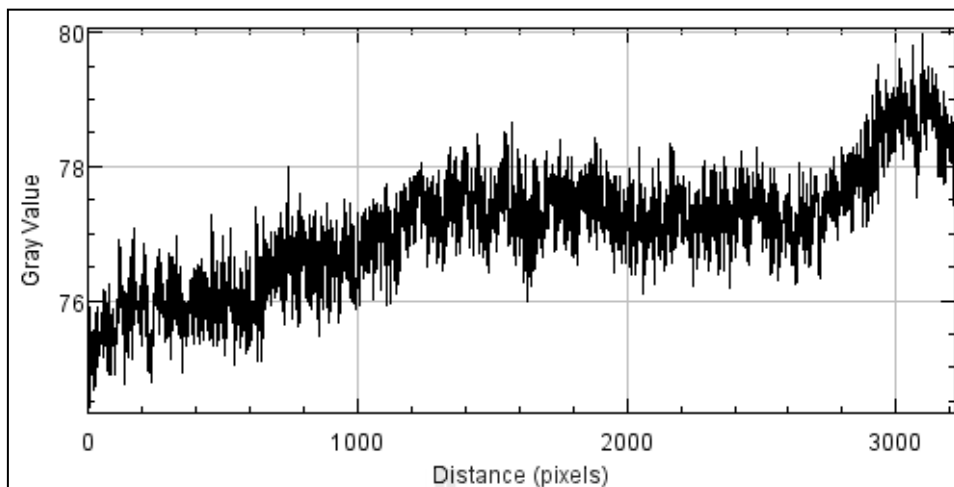
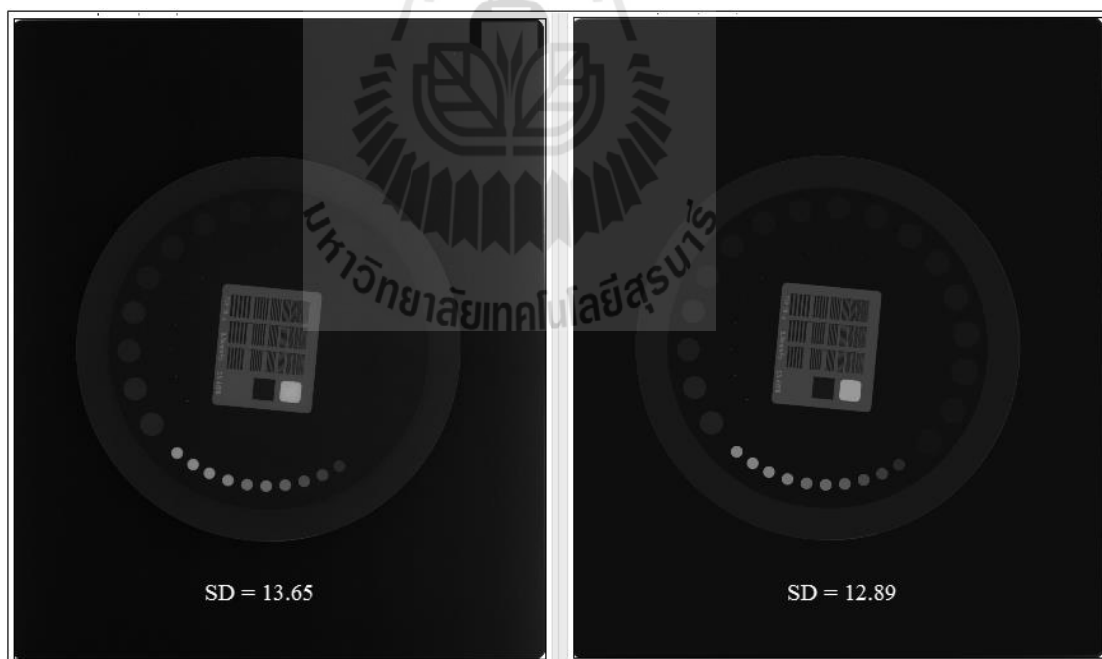


Figure 4.6 Plot of laser beam function for test jitter

4.2 Classification the Noise in Computed Radiography System



(a)

(b)

Figure 4.7 The CR image, (a) and (b), the original image

4.2.1 Result of Formation the Original Image

The original image was adjusted for the lowest noise. Its standard deviation is 12.89 as shown in Figure 4.7 (b) and it is compared with CR image, the image before adjustment as shown in Figure 4.7 (a). The CR image obtained from processing by a CR reader, 10 bit gray scale images with intensity level 0-1023, but in this study, the lookup table adjusted to the 8 bit image with intensity level 0-255.

4.2.2 Results of Production the Known-Noise

1) Gaussian Noise

Image and histogram resulting from adding Gaussian noise to the image are shown in Figure 4.8.

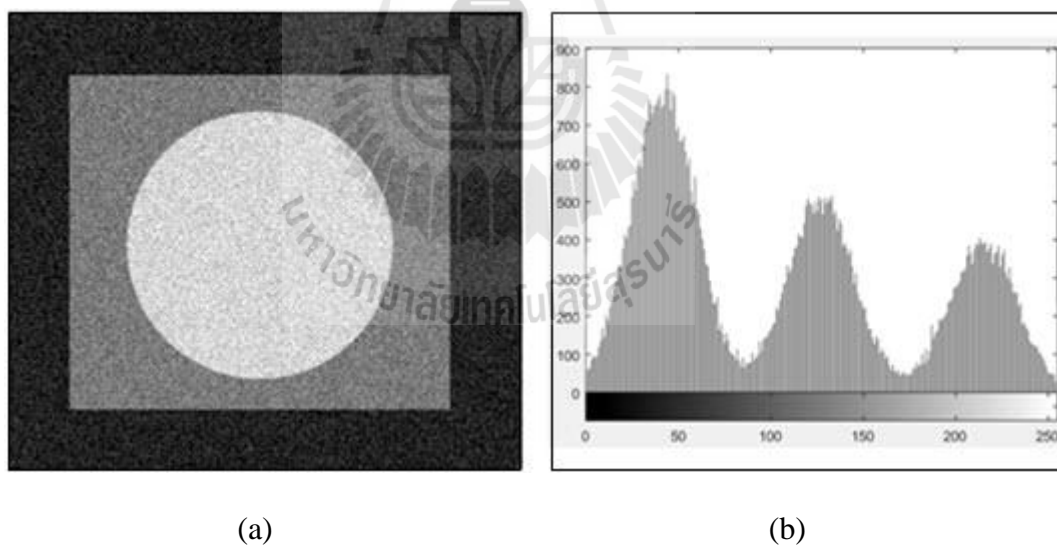


Figure 4.8 Image of added Gaussian noise to image, (a) and (b), its histogram

2) Rayleigh Noise

Image and histogram resulting from adding Rayleigh noise to the image are shown in Figure 4.9.

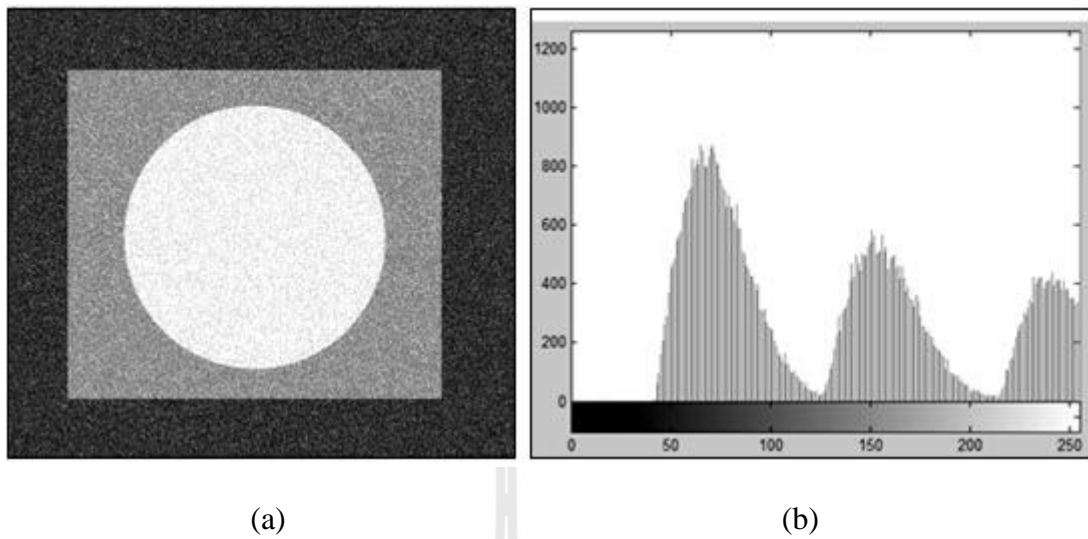


Figure 4.9 Image of added Rayleigh noise to image, (a) and (b), its histogram

3) Gamma Noise

Image and histogram resulting from adding gamma noise to the image are shown in Figure 4.10.

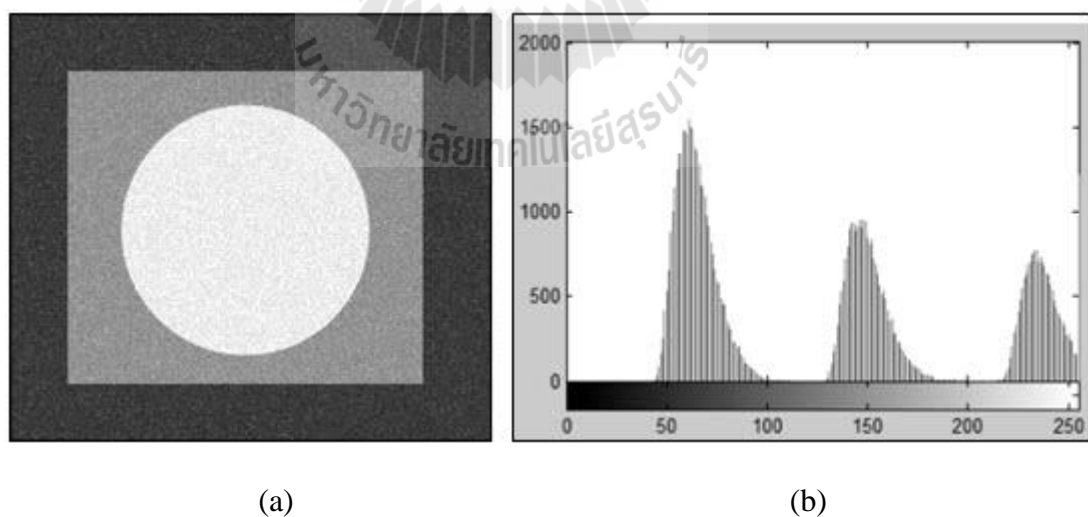


Figure 4.10 Image of added gamma noise to image, (a) and (b), its histogram

4) Exponential Noise

Image and histogram resulting from adding exponential noise to the image are shown in Figure 4.11.

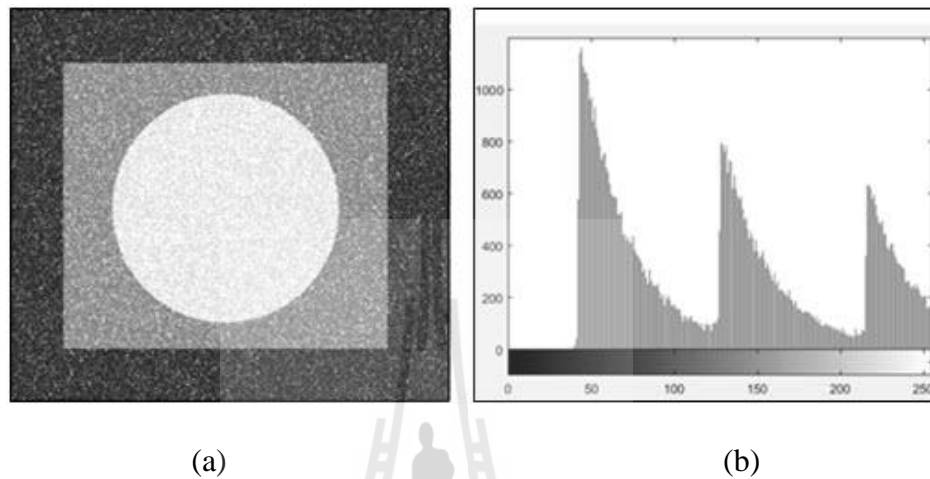


Figure 4.11 Image of added exponential noise to image, (a) and (b), its histogram

5) Uniform Noise

Image and histogram resulting from adding uniform noise to the image are shown in Figure 4.12.

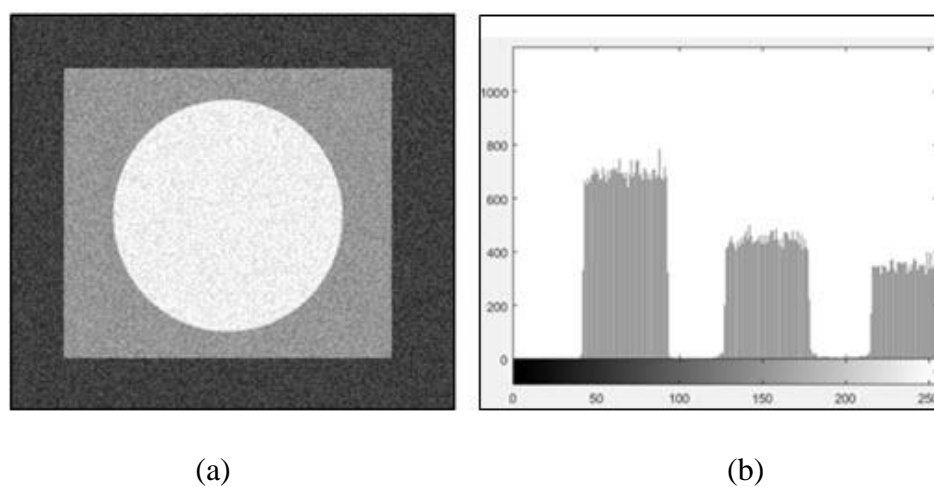


Figure 4.12 Image of added uniform noise to image, (a) and (b), its histogram

6) Impulse Noise

Image and histogram resulting from adding impulse noise to the image are shown in Figure 4.13.

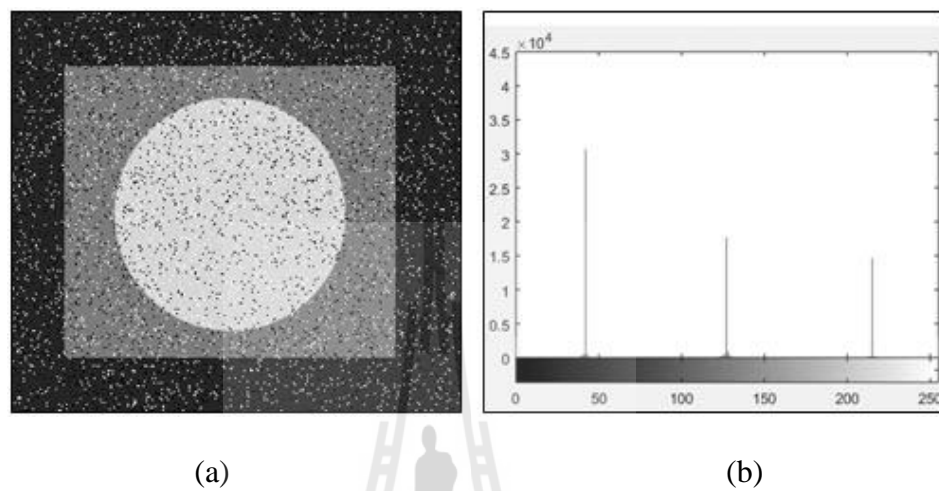


Figure 4.13 Image of added impulse noise to image, (a) and (b), its histogram

7) Poisson Noise

Image and histogram resulting from adding Poisson noise to the image are shown in Figure 4.14.

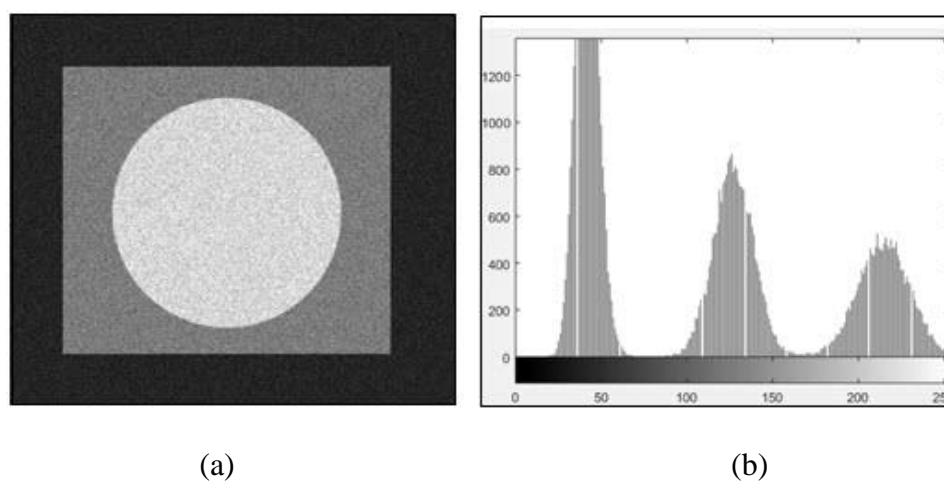


Figure 4.14 Image of added Poisson noise to image, (a) and (b), its histogram

4.2.3 Results of Adding the Known-Noise in Original Image

1) Gaussian Noise

The original image was added Gaussian noise, variable amounts to more as shown in Figure 4.15.



Figure 4.15 Images of added Gaussian noise to original image

2) Rayleigh Noise

The original image was added Rayleigh noise, variable amounts to more as shown in Figure 4.16.

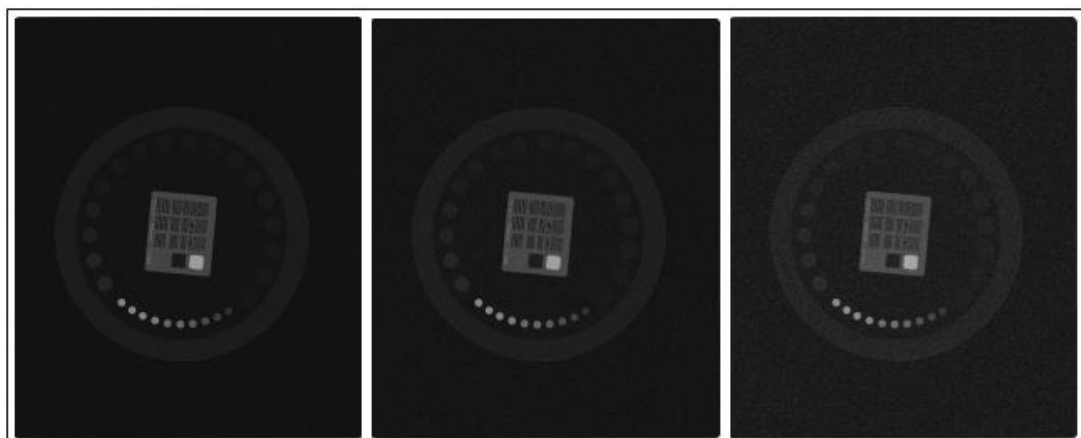


Figure 4.16 Images of added Rayleigh noise to original image

3) Gamma Noise

The original image was added gamma noise, variable amounts to more as shown in Figure 4.17.

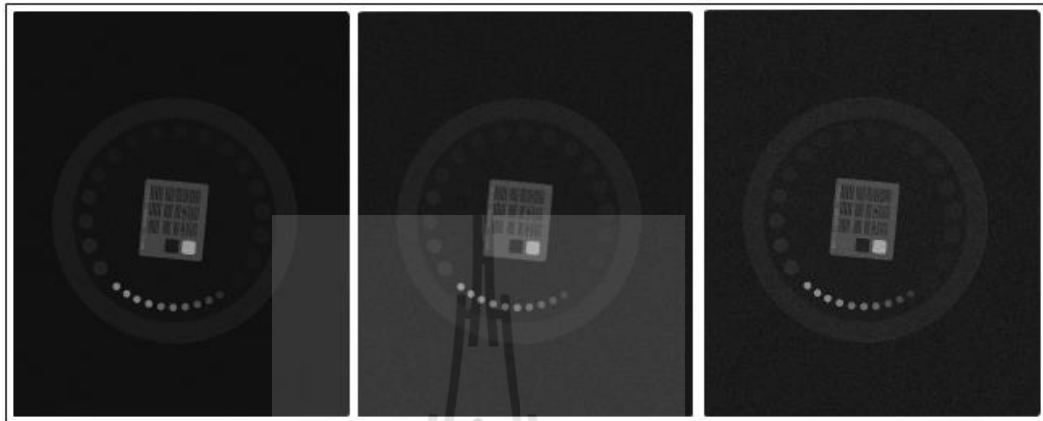


Figure 4.17 Images of added gamma noise to original image

4) Exponential Noise

The original image was added exponential noise, variable amounts to more as shown in Figure 4.18.

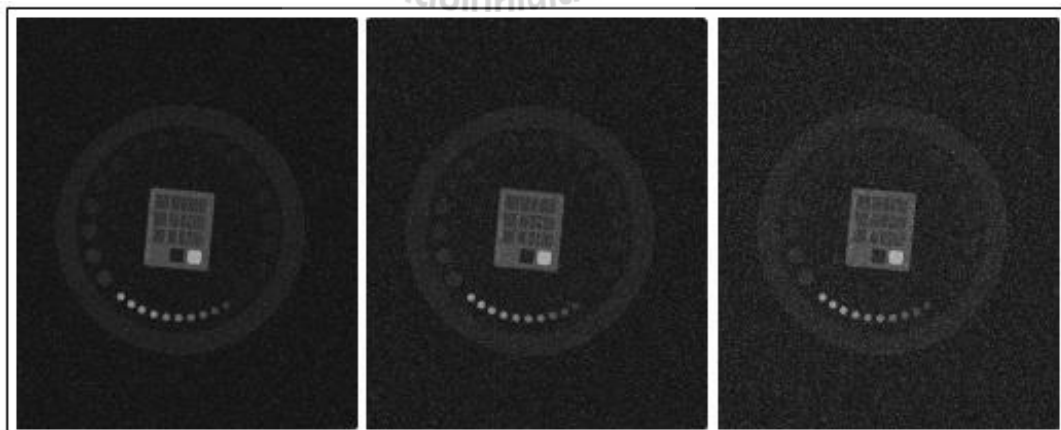


Figure 4.18 Images of added exponential noise to original image

5) Uniform Noise

The original image was added uniform noise, variable amounts to more as shown in Figure 4.19.

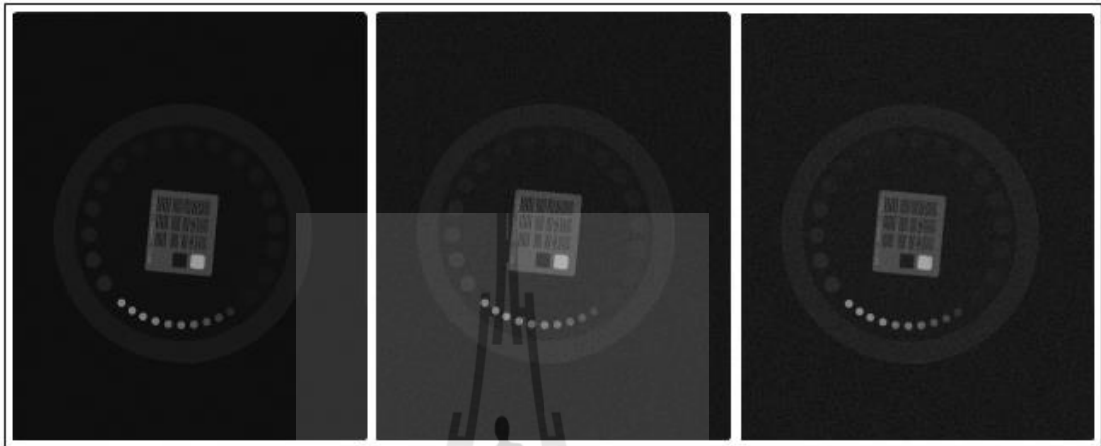


Figure 4.19 Images of added uniform noise to original image

6) Impulse Noise

The original image was added impulse noise, variable amounts to more as shown in Figure 4.20.

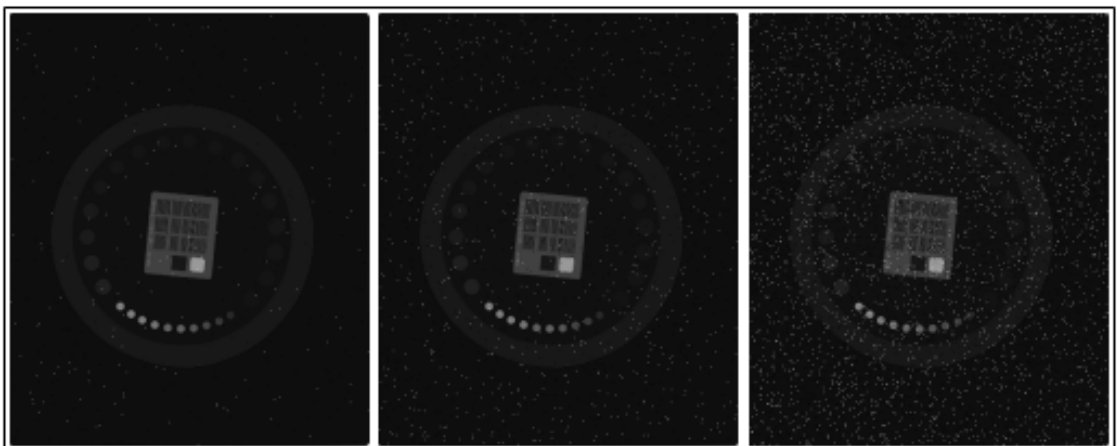


Figure 4.20 Images of added impulse noise to original image

7) Poisson Noise

The original image was added Poisson noise, variable amounts to more as shown in Figure 4.21.

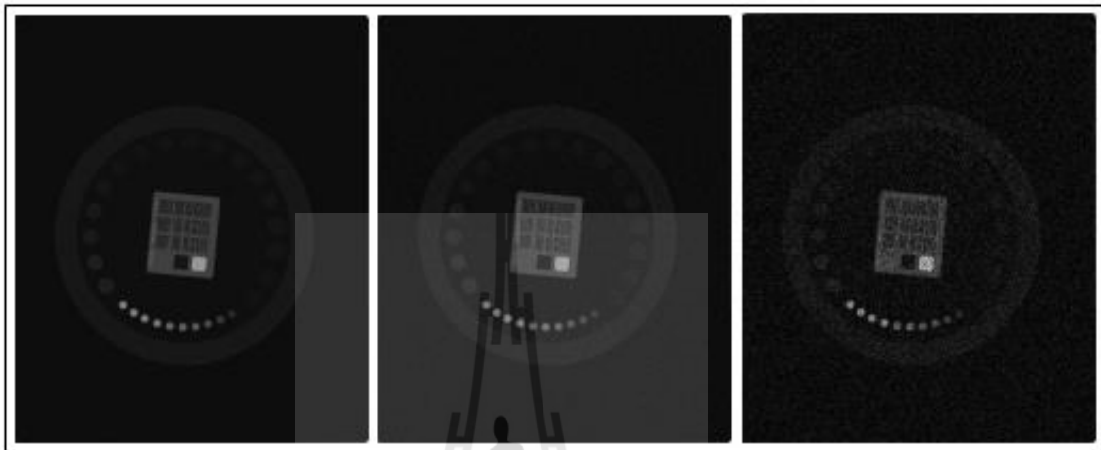


Figure 4.21 Images of added Poisson noise to original image

Image noise is random (not present in the object imaged) variation of brightness or color information in images, and is usually an aspect of electronic noise. It can be produced by the sensor and circuitry of a scanner or digital camera. Image noise can also originate in film grain and in the unavoidable shot noise of an ideal photon detector. Image noise is an undesirable by-product of image capture that adds spurious and extraneous information.

The original meaning of noise was and remains unwanted signal; unwanted electrical fluctuations in signals received by AM radios caused audible acoustic noise (static). By analogy unwanted electrical fluctuations themselves came to be known as noise (Stroebel and Zakia, 1995). Image noise is, of course, inaudible (Farooque and Rohankar, 2013).

The noisy images, added known-noise and their histogram of this study were similar to other (Gonzalez and Woods, 2002).

4.2.4 Result of Feature Extraction

The results for feature extraction were presented in Table 4.12.

Table 4.12 The values of feature extraction

Feature	Maximum	Minimum	Mean	SD
Mean	25.499	17.766	19.100	1.776
SD	18.120	12.890	13.174	0.615
MSE	72.636	0.011	7.021	13.149
PSNR	67.747	29.519	46.109	8.315
Class = Gaussian (100 instances), Poisson (100 instances), Impulse (100 instances), Uniform (100 instances), Gamma (100 instances), Exponential (100 instances), Rayleigh (100 instances)				

The noisy images were extracted for features include Mean, SD, MSE, and PSNR. The amount each instance was 100 include Gaussian noise, Poisson noise, impulse noise, uniform noise, gamma noise, exponential noise, and Rayleigh noise.

4.2.5 Result of Feature Selection

The results for feature selection were presented in Table 4.13. The best subset was {SD, MSE}, the performance estimation was 88.00% and used time for modeling was 58.11. It was selected for modeling in the next step.

Table 4.13 The values of assessment the subsets for feature selection

Subset	Performance estimation (%)	Time (s)	Rank
{Mean}	52.14	56.17	11
{SD}	35.86	56.96	15
{MSE}	44.00	56.75	14
{PSNR}	44.43	56.25	13
{Mean, SD}	79.86	58.41	5
{Mean, MSE}	72.71	59.12	9
{Mean, PSNR}	78.14	59.40	8
{SD, MSE}	88.00	58.11	1
{SD, PSNR}	79.29	58.60	7
{MSE, PSNR}	45.43	59.23	12
{Mean, SD, MSE}	87.00	61.64	2
{Mean, SD, PSNR}	85.14	61.62	3
{SD, MSE, PSNR}	71.29	61.39	10
{Mean, MSE, PSNR}	79.43	61.47	6
{Mean, SD, MSE, PSNR}	84.86	65.59	4

4.2.6 Result of Modeling

The model for classification the noise in CR image of this study is shown in Figure 4.22.

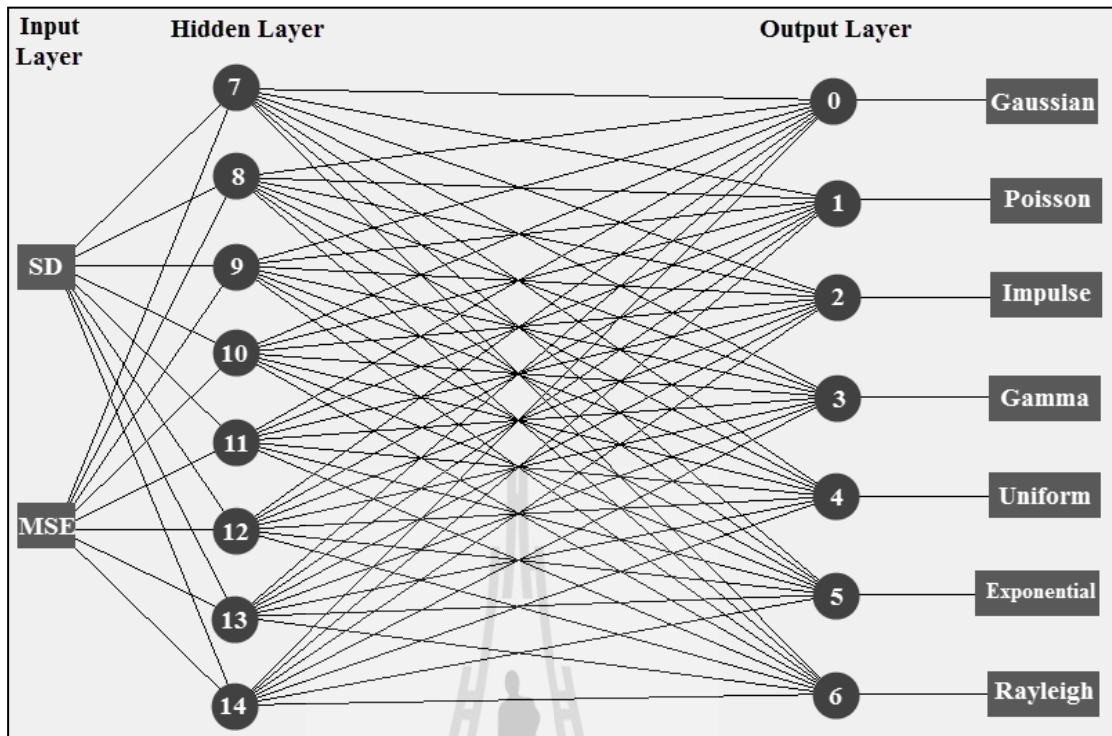


Figure 4.22 Model for classified noise

Figure 4.22, the model for classifying the type of noise using MLP algorithm, the input layer has 2 nodes, SD and MSE, the hidden layer has 8 nodes, and output layer has 7 nodes and the number of epochs for modeling was 30,000 epochs.

The classifier model of this study is presented in Table 4.14.

Table 4.14 Classifier model

Sigmoid Node	Input	Weight
Sigmoid Node 0	Threshold	-4.340293596662199
	Node 7	-32.3001983847927
	Node 8	-54.415574356793826
	Node 9	-53.64998768053294
	Node 10	-0.21753392344493436
	Node 11	-90.60613270681822
	Node 12	89.96138704616507
	Node 13	-27.467025036682383
	Node 14	-104.36743773019245
Sigmoid Node 1	Threshold	3.132948353829249
	Node 7	-2.290356052971897
	Node 8	71.14477705681175
	Node 9	-137.52537770522406
	Node 10	-0.32341139016187775
	Node 11	-134.15562653430484
	Node 12	-23.506774526451416
	Node 13	20.53757090863316
	Node 14	-53.97372123162601

Table 4.14 Classifier model (Continued)

Sigmoid Node	Input	Weight
Sigmoid Node 2	Threshold	-7.862564320960713
	Node 7	-11.332056135655781
	Node 8	-7.30433886241752
	Node 9	-3.003858945363586
	Node 10	1.4898523533574033
	Node 11	-10.773923307952298
	Node 12	4.1452669583953465
	Node 13	-1.5715334040918654
	Node 14	20.89187298311117
Sigmoid Node 3	Threshold	0.7313463812936851
	Node 7	-8.823577293262218
	Node 8	52.794224921884954
	Node 9	-24.270024386466297
	Node 10	-8.155679700658728
	Node 11	7.233495978471042
	Node 12	-82.11982739938247
	Node 13	-51.96902685168895
	Node 14	-29.602048583866623

Table 4.14 Classifier model (Continued)

Sigmoid Node	Input	Weight
Sigmoid Node 4	Threshold	2.4016547726041924
	Node 7	3.9868166426594347
	Node 8	-114.9109377681528
	Node 9	7.879416892279265
	Node 10	-25.60398219861567
	Node 11	2.1719825795285708
	Node 12	-44.50765155249919
	Node 13	8.433638253293662
	Node 14	-21.077406292798265
Sigmoid Node 5	Threshold	5.747784402371199
	Node 7	6.967472205782868
	Node 8	-158.43467927580497
	Node 9	56.55611218366482
	Node 10	-8.510803065511306
	Node 11	-63.803706033836455
	Node 12	-86.6279644098854
	Node 13	-30.15111355394148
	Node 14	-57.83075589657358

Table 4.14 Classifier model (Continued)

Sigmoid Node	Input	Weight
Sigmoid Node 6	Threshold	-3.6296772483795574
	Node 7	34.202014888602356
	Node 8	-14.794823269203217
	Node 9	7.898978846857413
	Node 10	-263.26633759843065
	Node 11	-29.204523425683874
	Node 12	18.46059278471141
	Node 13	9.214121419411706
	Node 14	9.315186775468174
Sigmoid Node 7	Threshold	135.22883664650792
	Attribute SD	-28.900734457219887
	Attribute MSE	164.18836801983977
Sigmoid Node 8	Threshold	-457.50800888175837
	Attribute SD	-616.24303234864
	Attribute MSE	57.53336793071455
Sigmoid Node 9	Threshold	-5.765321365869601
	Attribute SD	-76.72642327783892
	Attribute MSE	63.21186282835959
Sigmoid Node 10	Threshold	319.2570563688272
	Attribute SD	436.41000459355286
	Attribute MSE	-40.11613448796177

Table 4.14 Classifier model (Continued)

Sigmoid Node	Input	Weight
Sigmoid Node 11	Threshold	-292.6468676732117
	Attribute SD	-489.8711244056743
	Attribute MSE	117.09469060442025
Sigmoid Node 12	Threshold	22.521157631446876
	Attribute SD	497.63843863901405
	Attribute MSE	-387.8506480607345
Sigmoid Node 13	Threshold	79.97927419721971
	Attribute SD	96.25092801695251
	Attribute MSE	3.9898444380867897
Sigmoid Node 14	Threshold	1.2190564760491405
	Attribute SD	191.65954735383008
	Attribute MSE	-150.59469076305263

The classifier model, full training set consist of sigmoid node 0 include weight of threshold (w_0) and weight of node 7 -14, sigmoid node 1 include w_0 and weight of node 7 -14, sigmoid node 2 include w_0 and weight of node 7 -14, sigmoid node 3 include w_0 and weight of node 7 -14, sigmoid node 4 include w_0 and weight of node 7 -14, sigmoid node 5 include w_0 and weight of node 7 -14, and sigmoid node 6 include w_0 and weight of node 7 -14, sigmoid node 7 include w_0 and weight of SD and MSE, sigmoid node 8 include w_0 and weight of SD and MSE, sigmoid node 9 include w_0 and weight of SD and MSE,

sigmoid node 10 include w_0 and weight of SD and MSE, sigmoid node 11 include w_0 and weight of SD and MSE, sigmoid node 12 include w_0 and weight of SD and MSE, sigmoid node 13 include w_0 and weight of SD and MSE, and sigmoid node 14 include w_0 and weight of SD and MSE.

The evaluation of model is presented in Table 4.15. The Correctly classified instance is 93.33%. From Table 4.15, Gaussian noise, the model can be classified correctly all 300 instances with no mistakes, Poisson noise can be classified correctly 298 instances with 2 mistakes, impulse noise can be classified correctly 298 instances with 2 mistakes, gamma noise can be classified correctly 272 instances with 28 mistakes, uniform noise can be classified correctly 256 instances with 44 mistakes, exponential noise can be classified correctly 283 instances with 17 mistakes, and Rayleigh can be classified correctly 253 instances with 47 mistakes.

Table 4.15 Cross-validated confusion matrix for classifier

Classified as	Gaussian	Poisson	Impulse	Gamma	Uniform	Exponential	Rayleigh
Gaussian	300	0	0	0	0	0	0
Poisson	2	298	0	0	0	0	0
Impulse	2	0	298	0	0	0	0
Gamma	0	0	0	272	0	25	3
Uniform	0	5	0	27	256	11	1
Exponential	0	16	0	1	0	283	0
Rayleigh	0	7	0	27	3	10	253

The values of precision, recall and F-measure are presented in Table 4.16.

Table 4.16 Detailed accuracy by class

	Precision	Recall	F-measure
Gaussian	0.987	1	0.993
Poisson	0.914	0.993	0.952
Impulse	1	0.993	0.997
Gamma	0.832	0.907	0.868
Uniform	0.988	0.853	0.916
Exponential	0.860	0.943	0.900
Rayleigh	0.984	0.843	0.908
Weighted average	0.938	0.933	0.933

4.2.7 Results of Model Usage

The results for specifying the noise in CR images using model for this study are presented in Table 4.17.

The unseen data was classified by model, the procedure consist of:

Unseen image 1, SD = 13.5312, 9.8992.

Normalization used equation:

$$Normalization_attribute = \frac{attribute - base}{range} \quad (4.8)$$

$$range = \frac{\max_attribute - \min_attribute}{2} \quad (4.9)$$

$$base = \frac{\max_attribute + \min_attribute}{2} \quad (4.10)$$

Attribute SD: $range = \frac{18.356 - 12.383}{2} = 2.9865$

$$base = \frac{18.356 + 12.383}{2} = 15.3695$$

$$Normalization_SD = \frac{13.5312 - 15.3695}{2.9865} = -0.6155$$

Attribute MSE: $range = \frac{74.333 - 0.011}{2} = 37.1610$

$$base = \frac{74.333 + 0.011}{2} = 37.1720$$

$$Normalization_MSE = \frac{9.8992 - 37.1720}{37.1610} = -0.7339$$

Calculating at Node 7:

Summation function:

$$\{135.2288 + [(-0.6155) \times (-28.9007)] + [(-0.7339) \times 164.1884]\} = 32.5193$$

Activation function: using sigmoid function

$$f(x) = \frac{1}{1 + e^{-32.5293}} = 1$$

Calculating at Node 8:

Summation function:

$$\{(-457.5080) + [(-0.6155) \times (-616.2430)] + [(-0.7339) \times 57.5334]\} = -120.4340$$

Activation function: using sigmoid function

$$f(x) = \frac{1}{1 + e^{120.434}} = 0$$

Calculating at Node 9:

Summation function:

$$\{(-5.7653) + [(-0.6155) \times (-76.7264)] + [(-0.7339) \times 63.2119]\} = -4.9314$$

Activation function: using sigmoid function

$$f(x) = \frac{1}{1 + e^{4.9314}} = 0.01$$

Calculating at Node 10:

Summation function:

$$\{319.2571 + [(-0.6155) \times 436.4100] + [(-0.7339) \times (-40.1161)]\} = 80.0880$$

Activation function: using sigmoid function

$$f(x) = \frac{1}{1 + e^{-80.0880}} = 1$$

Calculating at Node 11:

Summation function:

$$\{(-292.6469) + [(-0.6155) \times (-489.8711)] + [(-0.7339) \times 117.0947]\} = -103.6772$$

Activation function: using sigmoid function

$$f(x) = \frac{1}{1 + e^{103.6772}} = 0$$

Calculating at Node 12:

Summation function:

$$\{22.5212 + [(-0.6155) \times 497.6384] + [(-0.7339) \times (-387.8506)]\} = 0.8683$$

Activation function: using sigmoid function

$$f(x) = \frac{1}{1 + e^{-0.8683}} = 0.7$$

Calculating at Node 13:

Summation function:

$$\{79.9793 + [(-0.6155) \times 96.2509] + [(-0.7339) \times 3.9898]\} = 17.8088$$

Activation function: using sigmoid function

$$f(x) = \frac{1}{1 + e^{-17.8088}} = 1$$

Calculating at Node 14:

Summation function:

$$\{1.2191 + [(-0.6155) \times 191.6595] + [(-0.7339) \times (-150.5947)]\} = -6.2259$$

Activation function: using sigmoid function

$$f(x) = \frac{1}{1 + e^{6.3359}} = 0$$

Calculating at Node 0: Gaussian noise

Summation function:

$$\{(-4.3403) + [1 \times (-32.3002)] + 0 + [0.01 \times (-53.6500)] + [1 \times (-0.2175)] + 0 + [0.7 \times 89.9614] + [1 \times (-27.4670)] + 0\} = -1.8885$$

Activation function: using sigmoid function

$$f(x) = \frac{1}{1 + e^{1.8885}} = 0.13$$

Calculating at Node 1: Poisson noise

Summation function:

$$\{3.1329 + [1 \times (-2.2904)] + 0 + [0.01 \times (-137.5254)] + [1 \times (-0.3234)] + 0 + [0.7 \times (-23.5068)] + [1 \times 20.5376] + 0\} = 3.2267$$

Activation function: using sigmoid function

$$f(x) = \frac{1}{1 + e^{-3.2267}} = 0.96$$

Calculating at Node 2: Impulse noise

Summation function:

$$\{(-7.8626) + [1 \times (-11.3321)] + 0 + [0.01 \times (-3.0039)] + [1 \times 1.4899] + 0 + [0.7 \times 4.1453] + [1 \times (-1.5715)] + 0\} = -16.4046$$

Activation function: using sigmoid function

$$f(x) = \frac{1}{1 + e^{16.4046}} = 0$$

Calculating at Node 3: Gamma noise

Summation function:

$$\{0.7313 + [1 \times (-8.8236)] + 0 + [0.01 \times (-24.2700)] + [1 \times (-8.1557)] + 0 + [0.7 \times (-82.1198)] + [1 \times (-51.9690)] + 0\} = -125.9436$$

Activation function: using sigmoid function

$$f(x) = \frac{1}{1 + e^{125.9436}} = 0$$

Calculating at Node 4: Uniform noise

Summation function:

$$\{2.4017 + [1 \times 3.9868] + 0 + [0.01 \times 7.8794] + [1 \times (-25.6040)] + 0 + [0.7 \times (-44.5077)] + [1 \times 8.4336] + 0\} = -41.8585$$

Activation function: using sigmoid function

$$f(x) = \frac{1}{1 + e^{41.8585}} = 0$$

Calculating at Node 5: Exponential noise

Summation function:

$$\{5.7478 + [1 \times 6.9675] + 0 + [0.01 \times 56.5561] + [1 \times (-8.5108)] + 0 + [0.7 \times (-86.6280)] + [1 \times (-30.1511)] + 0\} = -86.0206$$

Activation function: using sigmoid function

$$f(x) = \frac{1}{1 + e^{86.0206}} = 0$$

Calculating at Node 6: Rayleigh noise

Summation function:

$$\{(-3.6297) + [1 \times 34.2020] + 0 + [0.01 \times 7.8990] + [1 \times (-263.2663)] + 0 + [0.7 \times 18.4606] + [1 \times 9.2141] + 0\} = -210.4785$$

Activation function: using sigmoid function

$$f(x) = \frac{1}{1 + e^{210.4785}} = 0$$

The value of activation function from node 1 was highest thus the noise in unseen image 1 was Poisson.

Table 4.17 Specifying the noise in CR images

	Exposure Technique	SD	MSE	Classification
Unseen 1	(50 kVp, 3.2 mAs)	13.5312	9.8992	Poisson
Unseen 2	(50 kVp, 6.2 mAs)	13.3180	6.5987	Poisson
Unseen 3	(55 kVp, 6.2 mAs)	13.1208	3.5384	Poisson
Unseen 4	(60 kVp, 6.2 mAs)	13.0947	3.1695	Poisson
Unseen 5	(65 kVp, 6.2 mAs)	13.0375	2.2541	Poisson
Unseen 6	(70 kVp, 6.2 mAs)	13.0087	1.8457	Poisson
Unseen 7	(75 kVp, 6.2 mAs)	12.9783	1.0247	Gaussian
Unseen 8	(80 kVp, 6.2 mAs)	12.8984	0.1045	Gaussian

Table 4.17, the unseen data was classified by model include Unseen 1 is Poisson noise, Unseen 2 is Poisson noise, Unseen 3 is Poisson noise, Unseen 4 is Poisson noise, Unseen 5 is Poisson noise, Unseen 6 is Poisson noise, Unseen 7 is Gaussian noise, and Unseen 8 is Gaussian noise.

4.3 The Algorithm for De-noising

4.3.1 Results of Reduced Poisson Noise

Table 4.18 Comparison of MSE, PSNR and Correlation for Poisson noise de-noised by filters

Filters	MSE	PSNR	Correlation
Weiner filter	0.4787	51.3305	0.9970
Median filter	0.9239	48.4747	0.9860
Average filter	0.8055	49.0703	0.9919
Gaussian filter	0.6953	49.7091	0.9926

Table 4.18, the MSE, PSNR, and Correlation values resulting from different filters. The result showed that Weiner filter was more efficient for removing Poisson noise, but the performance of Gaussian filter was also good enough for Poisson noise.

Table 4.19 Comparison of MSE, PSNR and Correlation for Gaussian noise de-noised by filters

Filters	MSE	PSNR	Correlation
Weiner filter	1.9821	45.1597	0.9890
Median filter	5.6413	40.6170	0.9583
Average filter	4.0103	42.0990	0.9742
Gaussian filter	3.1082	43.2057	0.9793

4.3.2 Results of Reduced Gaussian Noise

Table 4.19, the MSE, PSNR, and Correlation values resulting from different filters. The result showed that Wiener filter was more efficient for removing Poisson noise, but the performance of Gaussian filter was also good enough for Poisson noise.

4.3.3 Results of the Prototype Program

1) Fuzzy Filter for Creating the Original Image

The fuzzy rule for creating the original image was used for calculating the matrix size of Wiener filter for de-noising. Example, the image, SD was 13 then the fuzzy rule calculated the matrix size as 7.09, as shown in Figure 4.23.

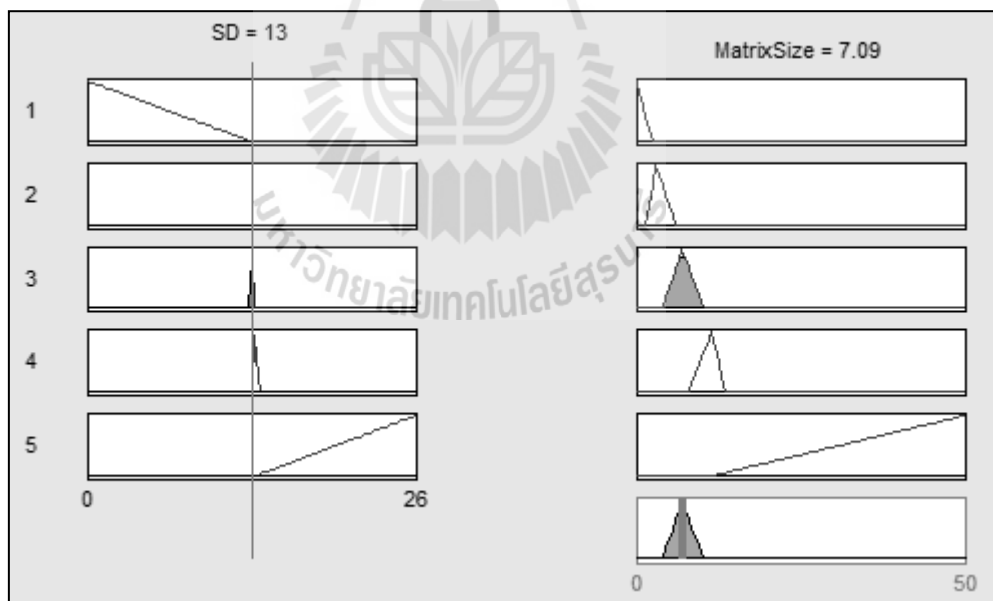


Figure 4.23 Rule viewer of creating original image

2) MLP Classification

The model for classifying noise was used for specifying the Gaussian noise or Poisson noise, as shown in Figure 4.24 and the correctly classified instances = 99.83%.

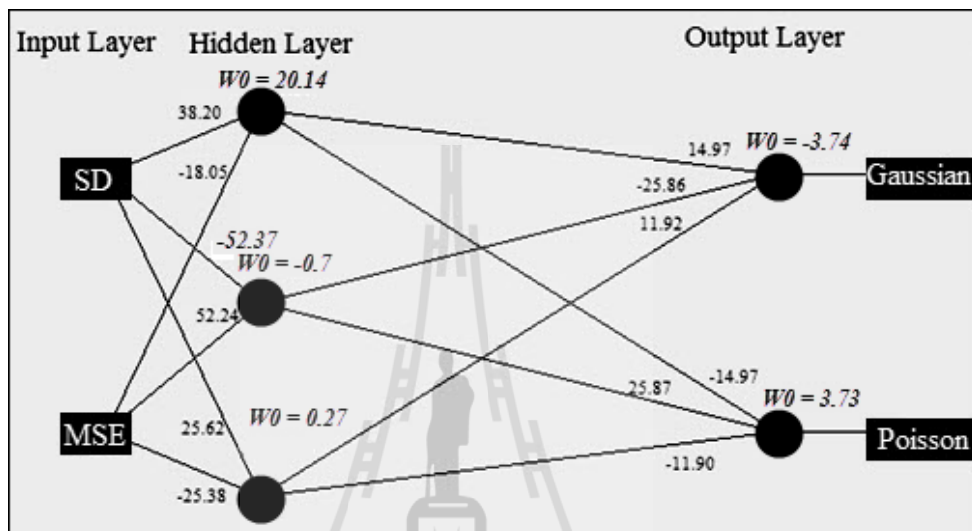


Figure 4.24 Rule viewer for classification

Table 4.20 Cross-validated confusion matrix for classifier

Actual/ Predicted	Gaussian	Poisson	Total	Recall
Gaussian	300	0	300	1
Poisson	1	299	300	0.997
Total	301	229	600	
Precision	0.997	1		

Table 4.20, the F-Measure of Gaussian was 0.998 that it was calculated by

$$F\text{-Measure} = \frac{(\beta^2 + 1)\text{Precision}}{\beta^2 \times \text{Precision} + \text{Recall}}, \text{ where } \beta = 1$$

$$F\text{-Measure} = \frac{(2) \times 0.997}{0.997 + 1} = 0.998.$$

The F-Measure of Poisson was 0.998 that it was calculated by

$$F\text{-Measure} = \frac{(\beta^2 + 1)\text{Precision}}{\beta^2 \times \text{Precision} + \text{Recall}}, \text{ where } \beta = 1$$

$$F\text{-Measure} = \frac{(2) \times 1}{1 + 0.997} = 0.998.$$

3) Fuzzy Filter for Poisson Noise

The fuzzy rule for filtering the Poisson noise was used for calculating the matrix size of Wiener filter for de-noising. Example, the image, SD was 13.5 and MSE was 0.591 then the fuzzy rule calculated the matrix size as 13.2, as shown in Figure 4.25.

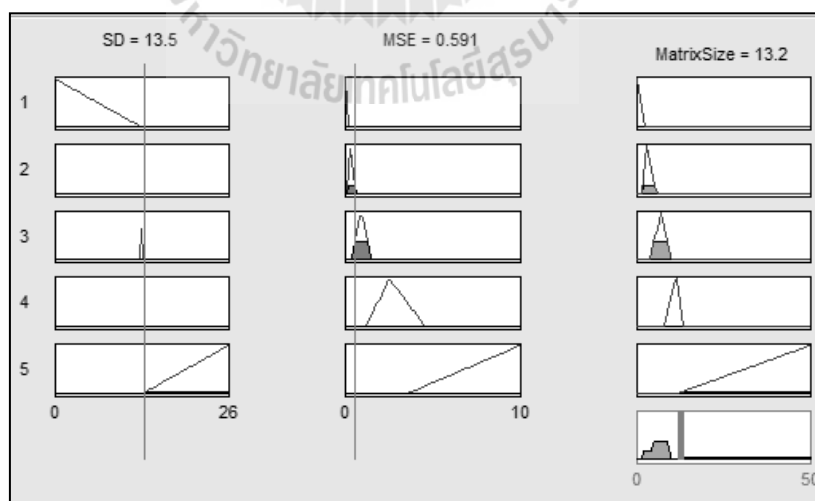


Figure 4.25 Rule viewer of filtering Poisson noise

4) Fuzzy Filter for Gaussian Noise

The fuzzy rule for filtering the Gaussian noise was used for calculating the matrix size of Wiener filter for de-noising. Example, the image, SD was 13 and MSE was 5 then the fuzzy rule calculated the matrix size as 7.17, as shown in Figure 4.26.

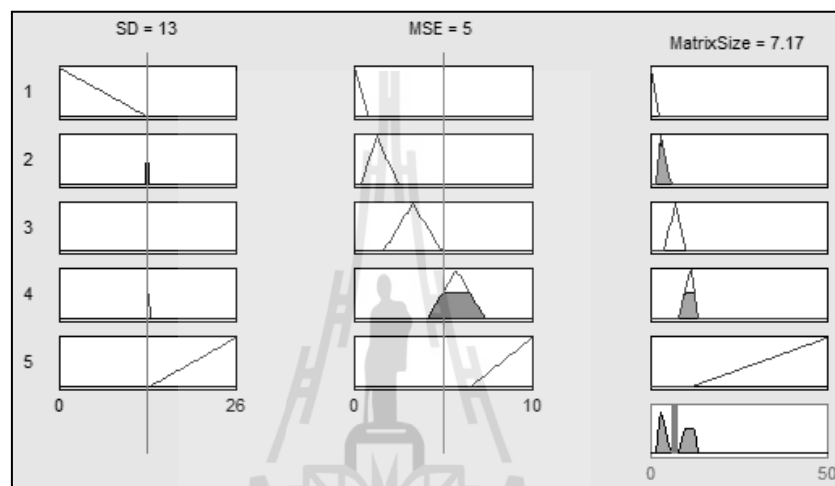


Figure 4.26 Rule viewer of filtering Gaussian noise

4.4 Hypothesis Testing

4.4.1 Result of De-noised CR image Using Prototype Program

1) Fuzzy Filter for Create Original Image

The SD of CR image was 13.6724 then the fuzzy filter was calculated the matrix size, it was 31.2, as shown in Figure 4.27. The approximate original image was produced by using Wiener filter, using neighborhoods of size 31.2 x 31.2.

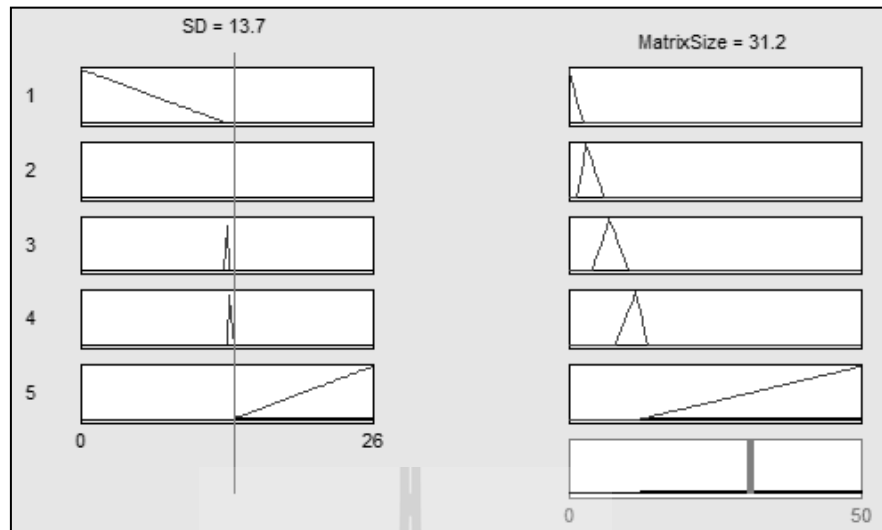


Figure 4.27 Rule viewer for calculating matrix size

2) MLP Classification

The MSE was 0.4775 and the SD was 13.6724, when they were classified by model that the result was Gaussian noise.

3) De-noising

The SD of CR image was 13.6724 and the MSE of CR image was 0.477 then the fuzzy filter was calculated the matrix size, it was 14.5, as shown in Figure 4.28. The fuzzy filter for de-noising was produced by using Wiener filter, using neighborhoods of size 14.5 x 14.5.

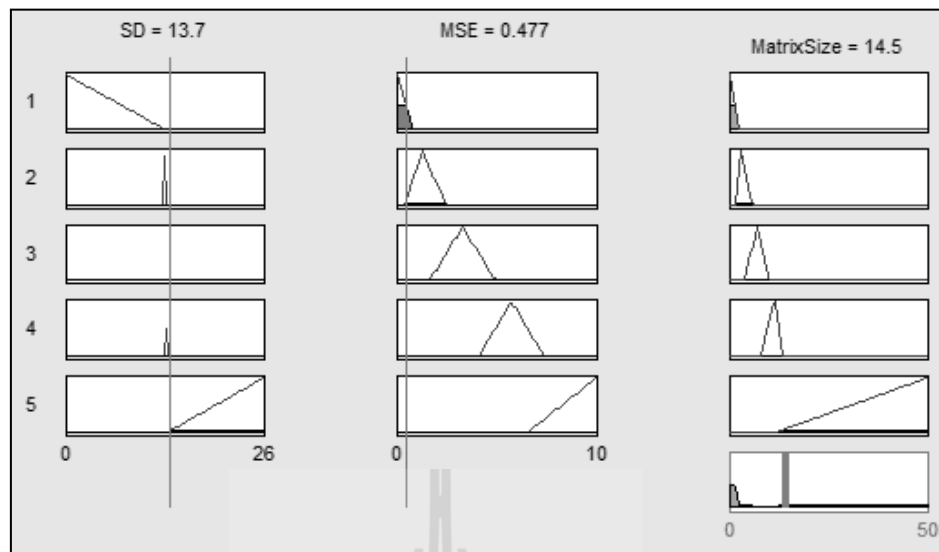


Figure 4.28 Rule viewer for de-noising

The values of de-noising image, the MSE value was 0.2822, the PSNR value was 53.6247 and the correlation value was 0.9972.

4.4.2 Result of De-noised CR image Using Vendor's Software

The CR image was de-noised by Vendor's software that the values of de-noising image, the MSE value was 0.4699, the PSNR value was 51.4110 and the correlation value was 0.9871.

In this study, the recalls for the classification of types of noise in the CR system are greater than 80% and the prototype software can be de-noised greater than the software currently available on the market when compared MSE, PSNR, and correlation.

CHAPTER 5

CONCLUSIONS AND RESEARCH RECOMMENDATIONS

The final chapter presents a summary of this study. It begins with describing the summary of the research findings. Then the limitations of the study are explained. Next, we explain the applications of the study. Finally, there are some suggestions for further studies.

5.1 Summary of the Research Findings

The objectives of this study were to develop an algorithm for the specification of the type of noise in the CR system, applying the appropriate algorithm for reducing noise in CR images, and creating a prototype software for de-noising in CR images. We propose commissioning and routine quality control of computed radiography for performing quality of CR system using guidelines provided by the Institute of Physics and Engineering in Medicine. Then, the algorithm for classification was developed for specifying the type of noise in the CR images using a neural network and a multilayer perceptron algorithm. Finally, the algorithms were applied for reducing specific noises and a prototype program was created for de-noising.

The research findings are summarized as follows:

5.1.1 Summary of Commissioning and Routine Quality Control of CR

(1) The mAs values for dosimetry were set for each air kerma that was used for performance and as a referent for the CR system.

(2) For the calibration of CR unit DDI, the percent differences for the values of 352.0 cm x 428.0 cm, 250.5 x 301.5 cm, and 200.0 x 251.0 cm Imaging Plates are acceptable (IPEM, 2010). The accuracy of the DDI for a particular Imaging Plate size was shown a difference of 20%.

(3) For the STP and DDI with standard factors, the relation of STP functions of 352.0 cm x 428.0 cm, 250.5 cm x 301.5 cm, and 200.0 cm x 251.0 cm Imaging Plates between the mean pixel value and the DAK are logarithm response that reveals they have a simple relationship (IPEM, 2010).

(4) For DDI Repeatability, the values of the Coefficient of Variation of DDI are less than 10% which is acceptable (IPEM, 2010).

(5) For the matching of CR Imaging Plates, the mean of DDI for 352.0 cm x 428.0 cm Imaging Plates in the batch was 10.07 μ Gy and the DDI of IP was nearest the mean so it was chosen for future QC performances. The mean of DDI for 250.5 cm x 301.5 cm Imaging Plates in the batch was 10.51 μ Gy and the DDI of IP was nearest the mean so it was chosen for future QC performances. The mean of DDI for 200.0 cm x 251.0 cm Imaging Plates in the batch was 10.07 μ Gy and the DDI of IP was nearest the mean so it was chosen for future QC performances. The DDI values of all Imaging Plate sizes are acceptable, the specified tolerance, DDI varies by < 20% between Imaging Plates (IPEM, 2010).

(6) Differences between CR readers, the CV values of DDI, the differences between 3 CR readers are less than 20% which are acceptable (IPEM,

2010) for DDI of differences between CR readers, FCR PROTECT, FCR XG5000 and FCR CAPSULA.

(7) Dark noise was found to have values below the specified tolerance for the Fuji CR reader, the specified tolerance, pixel value < 280 (IPEM, 2010).

(8) For measured uniformity, we found values below the specified tolerance for the IPEM Guidance, the specified tolerance, STP corrected ROI values within mean $\pm 10\%$ (IPEM, 2010).

(9) For erasure cycle efficiency, the results of the experiment show that there was no evidence of any “ghosting” on the second image for FCR PROTECT. Its light source could be used for erasing any longer.

(10) Variation of noise with detector air kerma, the relationship of variance and DAK is power response and the trend-line is not very good fit to the data. The measure of variance is useful indicator of noise in the images. The noise performance of the detector can be checked by plotting the variance of pixel values as a function of DAK.

(11) Signal to noise ratio is a useful concept for measuring the response of a digital detector quantitatively with simple tools. It may give information on system sensitivity and noise properties. In this study, the SNR values were 162.16 at the center of image, 136.90 at the center of quadrant I, 159.14 at the center of quadrant II, 160.94 at the center of quadrant III, and 145.56 at the center of quadrant IV.

(12) When limiting the high contrast spatial resolution, the results of 250.5×301.5 and 200.0×251.0 Imaging Plates were 3.54 and 3.93 for scan and sub-scan direction which is an acceptable level according to the IPEM Guideline, and

which are acceptable level values ≥ 3.5 for this study (IPEM, 2010). The results of 352.0 x 428.0 Imaging Plate were 2.87 for scan and sub-scan directions which are not an acceptable level according to the IPEM Guideline.

(13) For the laser beam function, the results from studying the CR system, a linear fit was calculated for the series of edge position values, thus obtaining the position of an ideal edge with no jitter.

5.1.2 Summary of Classification the Noise in CR System

In this study, the noises were generated in seven types which include Gaussian, Poisson, gamma, exponential, impulse, uniform, and Rayleigh. Their images and histograms were the same as those of Gonzalez and Woods (2002). The features were extracted from noisy images including the Mean, Standard Deviation (SD), Mean Square Error (MSE), and Peak Signal to Noise Ratio (PSNR), however, the features used only SD and MSE from the process of feature selection. They were used for modeling so that the seven noises in the CR images could be classified using the rule bases of multilayer perceptron (MLP) (Floreano and Mattiussi, 2008; Gonzalez and Woods, 2002). The results for specifying the noise in CR images using the model for this study revealed unseen data which were classified according to the Poisson noise type. However, the Gaussian noise type was specified when the high exposure was set at 75 kVp, 6.2 mAs and 80 kVp, 6.2 mAs, respectively.

5.1.3 Summary of Algorithm for De-noising

The CR images for added Poisson noise were de-noised by filters, Weiner, Median, Average, and Gaussian and when compared to MSE, PSNR and correlation it was found that the Weiner fitter was more efficient for removing the noise (Charhar and Thakare, 2015). The CR images for added Gaussian noise were

de-noised by filters and when compared to MSE, and PSNR, it was found that the correlation with the Wiener filter was more efficient for removing the noise (Charhar and Thakare, 2015).

The prototype program was created for de-noising CR image. Firstly, the original image was created and then the fuzzy filter was calculated for matrix size of Wiener filter. Next, the CR image was classified according to the model using the multilayer perceptron. Lastly, if the noise in the CR image is of the Poisson type, the fuzzy rule for filtering the Poisson noise will be used for calculating the matrix size of Wiener filter for de-noising. If the noise in the CR image is Gaussian, the fuzzy rule for filtering the Gaussian noise will be used for calculating the matrix size of Wiener filter for de-noising. In this study, the prototype software was able to de-noise to a greater extent than the software currently available on the market when compared to MSE, PSNR, and correlation.

5.2 The Limitation of the Study

The limitations of the development of a noise reduction model for a computed radiography system are as follows.

(1) The study for commissioning and routine quality control of CR, IPEM Guidance was performed for dosimetry, calibration of CR unit DDI, signal transfer property and DDI with standard factors, DDI repeatability, matching of CR Imaging Plates, differences between CR readers, dark noise, measured uniformity, erasure cycle efficiency, variation of noise with detector air kerma, signal to noise ratio, limiting high contrast spatial resolution, and laser beam function. Nevertheless, this study was not able to conduct some experiments, such as threshold contrast detail

detectability, blurring, scaling errors, and Moire patterns and anti-scatter grids, because of a lack of suitable equipment.

(2) This research used phantom instead of patients. The TOR CDR phantom was exposed to radiography for this study. The original image was processed from retouching software and it assumed a noiseless image. The noises, Gaussian noise, Rayleigh noise, gamma noise, exponential noise, uniform noise, impulse noise, and Poisson noise were generated from MATLAB commands that were used instead of the noise in the CR images.

(3) The prototype program created an approximate image instead of using the original image. This research used the spatial domain for creating the fuzzy filters for de-noising and it also studied gray scale images.

5.3 The Application of the Study

This research demonstrates the following benefits:

It can be used for commissioning and routine quality control of CR and as a referent for quality control of CR systems in the future and for comparison with other CR systems. These experiments can be studied by technical experts or physicists.

The noise in the CR images was specified as Poisson and Gaussian noises then they were de-noised by using the appropriate software. The algorithms could be used for de-noising so that the CR images enhanced accuracy for diagnoses. This will provide great benefits to patients.

The algorithms for modeling of part classification could be applied for resolve problems concerning the diagnoses of patients in hospital.

The prototype software for de-noising CR images could be applied for de-noising other types of noise, such as in Digital Radiography (DR) images, Computed Tomography (CT) images, Magnetic Resonance Imaging (MRI), Nuclear Medicine images, and digital images.

5.4 Recommendations for Further Study

There are some possible improvements that we would like to recommend for the near future as described below:

(1) The commissioning and routine quality control of CR uses the guidance of the American Association of Physicists in Medicine (AAPM) for comparison with the Institute of Physics and Engineering in Medicine (IPEM) guidance. The DR system and others should be used for quality control.

(2) The algorithms for classification the noise in the CR images can be applied, such as changing the type of noise for modeling, the amount of known-noise types could be increased or decreased to appropriate amounts, the model of multilayer perceptron could be applied for use with other problems, such as a model to diagnose the X-ray image instead of a physician, and the model could also be used for the selection of X-ray images which could lead to the rejection of a diagnosis.

(3) The prototype software could be applied, such as the software de-noised in the color images, the software de-noised in the ultrasound images, the algorithms used other techniques, for example, Naïve Bayes, Neuro fuzzy for classification, de-noising in frequency domain or wavelet transforms.

REFERENCES

- AAPM (American Association of Physicists in Medicine). (2006). **Acceptance Testing and Quality Control of Photostimulable Storage Phosphor Imaging Systems**. AAPM Report 93 by Task Group 10. Maryland: College Park.
- Albert, M., Beideck, D. J., Bakic, P. R., and Maidment, A. D. A. (2002). Aliasing Effects in Digital Images of Line-pair Phantoms. **Medical Physics**. 29: 1716-1718.
- Altas, I., Louis, J., and Belward, J. (1995). A Variational Approach to the Radiometric Enhancement of Digital Imagery. **IEEE Transactions on Medical Imaging**. 4(6): 845-849.
- Barboriak, D., Padua, A., York, G., and Macfall, J. (2005). Creation of DICOM-Aware Applications Using ImageJ. **J Digit Imaging**. 18(2): 91-99.
- Boyat, A. K., and Joshi, B. K. (2015). A Review Paper: Noise Models in Digital Image Processing. **Signal & Image Processing: An International Journal**. 6(2): 63-75.
- Burgess, A. E. (1999). The Rose Model, Revisited. **Journal of the Optical Society of America**. 16: 633-646.
- Bushberg, J. T., Seibert, J. A., Leidholdt, E. M., and Boone, J. M. (2002). **The Essential Physics of Medical Imaging**. 2nd ed. Baltimore: Lippincott Williams & Wilkins.

- Carter, C. E., and Veale, B. L. (2010). **Digital Radiography and PACS**. St. Louis, Missouri: Mosby.
- CEP (Centre for Evidence-based Purchasing) (2006a). **Computed Radiography (CR) Systems for General Radiography**. A Comparative Report, 2nd ed. London: CEP.
- CEP (Centre for Evidence-based Purchasing) (2006b). **Computed Radiography (CR) Systems for General Radiography**. Agfa Healthcare DX-S. London: CEP.
- Chan, Y.D., and Xu, R. H. S. (2007). A Detection Statistic for Random-Valued Impulse Noise. **IEEE Transactions on Image Processing**. 16 (4): 1112-1120.
- Charhar, P. S., and Thakare, V. V. (2015). Performance Comparison of Various Filters for Removing Gaussian and Poisson Noises. **International Research Journal of Engineering and Technology**. 2(5): 1101-1105.
- Collins, T. J. (2007). ImageJ for Microscopy. **BioTechniques**. 43(1 Suppl): 25-30.
- Cormen, T. H., Leiserson, C. E., Rivest, R. L., and Stein, C. (2009). **Introduction to Algorithms**. 3rd ed. Cambridge, Massachusetts: Massachusetts Institute of Technology.
- Eliceiri, K., and Rueden, C. (2005). Tools for visualizing Multidimensional Images from Living Specimens. **Photochem Photobiol**. 81(5): 1116-1122.
- Evans, D. S., Workman, A., and Payne, M. (2002). A Comparison of the Imaging Properties of CCD-based Devices Used for Small Field Digital Mammography. **Physics in Medicine and Biology**. 47: 117-135.

- Farooque, M. A., and Rohankar, J. S. (2013). Survey on Various Noised and Techniques for De-noising the Color Image. **International Journal of Application or Innovation in Engineering & Management**. 2(11): 217-221.
- Fetterly, K. A., and Hangiandreou, N. J. (2001). Effects of X-ray Spectra on the DQE of a Computed Radiography System. **Medical Physics**. 28: 241-249.
- Floreano, D., and Mattiussi, C. (2008). **Bio-Inspired Artificial Intelligence—Theories, Methods, and Technologies**. Massachusetts: MIT.
- Flynn, M. J., and Samei, E. (1999). Experimental Comparison of Noise and Resolution for 2k and 4k Storage Phosphor Radiography Systems. **Medical Physics**. 26: 1612-1623.
- Gering, E., and Atkinson, C. (2004). A Rapid Method for Counting Nucleated Erythrocytes on Stained Blood Smears by Digital Image Analysis. **J Parasitol**. 90(4): 879-881.
- Girish, V., and Vijayalakshmi, A. (2004). Affordable Image Analysis Using NIH Image/ ImageJ. **Indian J Cancer**. 41(1): 47.
- Gonzalez, R. C., and Woods, R. E. (2002). **Digital Image Processing**. 2nd ed. New Jersey: Prentice-Hall.
- Gravel, P., Beaudoin, G., and De Guise, J. A. (2004). A Method for Modeling Noise in Medical Images. **IEEE Transactions on Medical Imaging**. 23(10): 1221-1232.
- Grossberg, S. (1987). Competitive Learning: From Interactive Activation to Adaptive Resonance. **Cognitive Science**. 11: 121-134.

- Haight, F. A. (1967). **Handbook of the Poisson Distribution**. New York: John Wiley & Sons.
- Holmblad, L. P., and Ostergaard, J. J. (1982). **Control of Cement Kiln by Fuzzy Logic**. North Holland.
- Honey, I. D., and Mackenzie, A. (2009). Artifacts Found During Quality Assurance Testing of Computed Radiography and Digital Radiography Detectors. **Journal of Digital Imaging**. 22: 383-392.
- IEC (International Electrotechnical Commission). (2005). **Medical Diagnostic X-ray Equipment - Radiation Conditions for Use in the Determination of Characteristics**. IEC 61267. Geneva: IEC.
- IEC (International Electrotechnical Commission). (2008). **Medical Electrical Equipment - Exposure Index of Digital X-ray Imaging Systems - Part I: Definitions and Requirements for General Radiography**. IEC 62494-1. Geneva: IEC.
- IPEM (Institute of Physics and Engineering in Medicine). (2005). **Recommended Standards for the Routine Performance Testing of Diagnostic X-ray Imaging Systems. IPEM Report 91**. IPEM, York.
- IPEM (Institute of Physics and Engineering in Medicine). (2010). **Measurement of the Performance Characteristics of Diagnostic X-ray Systems: Digital Imaging Systems**. IPEM Report 32 Part VII. IPEM, York.
- Jang, J-S. R., Sun, C-T., and Mizutani, E. (1997). **Neuro-Fuzzy and Soft Computing: A Computational Approach to Learning and Machine Intelligence**. NJ: Prentice-Hall.

- KCARE. (2005). **Protocol for the QC of Computed Radiography Systems Commissioning and Annual QA Tests.** KCARE.
- Koli, M., and Balaji, S. (2013). Literature Survey on Impulse Noise Reduction. **Signal & Image Processing: An International Journal.** 4(5): 75-95.
- Lal, S., Chandra, M., and Upadhyay, G. K. (2009). Noise Removal Algorithm for Images Corrupted by Additive Gaussian Noise. **International Journal of Recent Trends in Engineering.** 2(1): 199-206.
- Le, T., Chatrand, R. and Asaki, T. J. (2007). A Variational Approach to Reconstructing Images Corrupted by Poisson Noise. **Journal of Mathematical Imaging and Vision.** 27(3): 257-263.
- Leblans, P., Vandebroucke, D., and Willems, P. (2011). Storage Phosphors for Medical Imaging. **Materials.** 4: 1034-1086.
- Mackenzie, A. (2008). Validation of Correction Methods for the Non-linear Response of Digital Radiography Systems. **British Journal of Radiology.** 81: 341.
- Mackenzie, A., and Honey, I. D. (2007). Characterization of Noise Sources for Two Generations of Computed Radiography Systems Using Powder and Crystal Line Photostimulable Phosphors. **Medical Physics.** 38(4): 3345-3357.
- Mamdani, E. H., and Assilion, S. (1999). An Experiment in Linguistic Synthesis With a Fuzzy Logic Controller. **International Journal of Human-Computer Studies.** 51(2): 135-147.

- Masood, S., Hussain, A., and Jaffar, M. A. (2012). Studied Intelligent Noise Detection and Filtering Using Neuro-Fuzzy System. **Multimed Tools Appl.** 63: 93-105.
- McCulloch, W., and Pitts, W. (1943). A Logical Calculus of the Ideas Immanent in Nervous Activity. **Bulletin of Mathematical Biophysics.** 5: 115-133.
- MHRA (Medicines and Healthcare Products Regulatory Agency). (2006). **Radiation Dose Issues with Digital Radiography Systems.** MHRA notice.
- Moler, C. (2004). **The Origins of MATLAB.** MathWorks.
- Palakkal, S., and Prabhu, K. M. M. (2012). Poisson Image Denoising Using Fast Discrete Curvelet Transform and Wave Atom. **Signal Processing.** 92: 2002-2017.
- Quinlan, I. R. (1993). **C4.5: Programs for Machine Learning.** San Francisco: Morgan Kaufmann Publishers.
- Quinn, B., and Carroll, M. (2011). **Radiography in the Digital Age.** Illinois: Springfield.
- Rajwa, B., McNally, H., Varadharajan, P., Sturgis, J., and Robinson, J. (2004). AFM/ CLSM Data Visualization and Comparison Using an Open-source Toolkit. **Microsc Res Tech.** 64(2): 176-184.
- Rampado, O., Isoardi, P., and Ropolo, R. (2006). Quantitative Assessment of Computed Radiography Quality Control Parameters. **Phys Med Biol.** 51(2006): 1-17.
- Rowlands, J. A. (2002). The Physics of Computed Radiography. **Physics in Medicine and Biology.** 47: R123-R166.

- Rudin, L. I., Osher, S., and Fatemi, E. (1992). Nonlinear Total Variation Based Noise Removal Algorithms. **Physica D: Nonlinear Phenomena**. 60(1-4): 259-268.
- Rueden, C. T., and Eliceiri, K. W. (2007). Visualization Approaches for Multidimensional Biological Image Data. **Bio Techniques**. 43(1 Suppl): 31, 33-36.
- Samei, E., Seibert, J. A., Willis, C. E., Flynn, M. J., Mah, E., and Junck, K. L. (2001). Performance Evaluation of Computed Radiography Systems. **Med Phys**. 28(3): 361-371.
- Santhanam, T., and Radhika, S. (2005). Probabilistic Neural Network a Better Solution for Noise Classification. **Journal of Theoretical and Applied Information Technology**. 27(1): 39-42.
- Schneider, C. A., Rasband, W. S., and Eliceiri, K. W. (2012). NIH Image to ImageJ: 25 Years of Image Analysis. **Nat Methods**. 9(7): 671-675.
- Sherer, M. A. S., Visconti, P. J., Ritenour, E. R., and Haynes, K. W. (2014). **Radiation Protection in Medical Radiography**. 7th ed. Maryland Heights: Elsevier Mosby.
- Sokolava, M., and Lapalme, G. (2009). A Systematic Analysis of Performance Measures for Classification Tasks. **Information Processing and Management**. 45(4): 427-437.
- Solomon, C., and Breckon, T. (2011). **Fundamentals of Digital Image Processing: A Practice Approach with Examples in MATLAB**. West Sussex: Wiley-Blackwell.

- Stroebel, L. D., and Zakia, R. D. (1995). **The Focal Encyclopedia of Photography**. Focal.
- Sun, Z., Chen, S., and Qiao, L. (2014). A General Non-local Denoising Model Using Multi-Kernel-Induced Measures. **Pattern Recognition**. 47(2014): 1751-1763.
- Tiwari, S., Singh, A. K., and Shukla, V. P. (2011). Studied Statistical Moments Based Noise Classification Using Feed Forward Back Propagation Neural Network. **International Journal of Computer Applications**. 18(2): 36-40.
- Tucker, D. M., and Rezendes, P. S. (1997). The Relationship between Pixel Value and Beam Quality in Photostimulable Phosphor Imaging. **Medical Physics**. 24: 887-893.
- Wang, Y., Fan, Y., Bhatt, P., and Davatzikos, C. (2010). High-dimensional Pattern Regression Using Machine Learning: From Medical Images to Continuous Clinical Variables. **Neuro Image**. 50(2010): 1519-1535.
- Zadeh, L. A. (1965). Fuzzy Sets. **Intl J. Information Control**. 8(3): 338-353.
- Zhang, W. X., Cao, Y. Z., Zhang, R. X., and Wang, Y. Q. (2014). Image Denoising Using Total Variation Model Guided by Steerable Filter. **Mathematical Problems in Engineering**. 1-11.

CURRICULUM VITAE

Mr. Boonserm Nerysungnoen was born on November 19, 1972 in Nakhon Ratchasima Province, Thailand. He received Bachelor of Science (Radiological Technology) from Khon Kaen University in 2005, Master of Science (Medical Imaging) from Chulalongkorn University in 2008, and Master of Science (Mathematics and Technology for Teaching) from Nakhon Ratchasima Rajabhat University in 2013. In 2013, he has got a scholarship from Institute of Social Technology, School of Information Technology, Suranaree University of Technology to pursue his doctoral degree in Information Technology Program at Suranaree University of Technology. His major research interests are digital image processing, noise in digital images, and neural network.

